Università degli Studi di Cagliari

PhD COURSE IN

ELECTRONIC AND COMPUTER ENGINEERING

XXVIII CYCLE

MANAGEMENT AND MODELLING OF BATTERY STORAGE SYSTEMS IN MICROGRIDS AND VIRTUAL POWER PLANTS

ING-IND/32 Convertitori, Macchine e Azionamenti elettrici

Author	MAURA MUSIO
PhD Course Coordinator	Prof. Fabio Roli
Advisor	Prof. Alfonso Damiano

2014 – 2015

Ph.D. in Electronic and Computer Engineering
Dept. of Electrical and Electronic Engineering
University of Cagliari

Management and Modelling of Battery Storage Systems in MicroGrids and Virtual Power Plants

Maura Musio

Advisor: prof. Alfonso Damiano
Curriculum: ING-IND/32 Convertitori, macchine e azionamenti elettrici

XXVIII Cycle
March 2016

Abstract

In the novel smart grid configuration of power networks, Energy Storage Systems (ESSs) are emerging as one of the most effective and practical solutions to improve the stability, reliability and security of electricity power grids, especially in presence of high penetration of intermittent Renewable Energy Sources (RESs).

This PhD dissertation proposes a number of approaches in order to deal with some typical issues of future active power systems, including optimal ESS sizing and modelling problems, power flows management strategies and minimisation of investment and operating costs. In particular, in the first part of the Thesis several algorithms and methodologies for the management of microgrids and Virtual Power Plants, integrating RES generators and battery ESSs, are proposed and analysed for four cases of study, aimed at highlighting the potentialities of integrating ESSs in different smart grid architectures. The management strategies here presented are specifically based on rule-based and optimal management approaches. The promising results obtained in the energy management of power systems have highlighted the importance of reliable component models in the implementation of the control strategies. In fact, the performance of the energy management approach is only as accurate as the data provided by models, batteries being the most challenging element in the presented cases of study. Therefore, in the second part of this Thesis, the issues in modelling battery technologies are addressed, particularly referring to Lithium-Iron Phosphate (LFP) and Sodium-Nickel Chloride (SNB) systems. In the first case, a simplified and unified model of lithium batteries is proposed for the accurate prediction of charging processes evolution in EV applications, based on the experimental tests on a 2.3 Ah LFP battery. Finally, a dynamic electrical modelling is presented for a high temperature Sodium-Nickel Chloride battery. The proposed modelling is developed from an extensive experimental testing and characterisation of a commercial 23.5 kWh SNB, and is validated using a measured current-voltage profile, triggering the whole battery operative range.

Table of Contents

To the people who care about me, and look after me.
To the people who loved me, and now look at me from the sky.
To my family.

Introduction

The awareness of climate changes caused by energy production and consumption systems has driven the worldwide policies to promote a sustainable energy transition. In order to combine the needs of an energy growing demand with a sustainable development, the distributed generation (DG) based on Renewable Energy Sources (RESs) was significantly supported in the last years. However, the natural variability of some renewable sources, such as wind and solar, has introduced a series of challenges in order to preserve the quality, reliability and controllability of the electricity grid. As result, the classic hierarchical and strictly regulated management model of the present power systems is no more suitable for handling a progressive increment of energy supply from intermittent RES. In fact, the integration of these technologies at a significant scale requires a much more flexible grid that can cope with the variability and uncertainty of supply introduced by RES systems.

One of the most approved solutions is the use of a distributed electricity management approach based on the local clustering of demand and generation and on the adoption of a suitable network supervisory control. The aim is reducing the impact of the intermittent RES generation and improving the dispatching efficiency both technically and economically, resorting to the use of Energy Management Systems (EMSs). In this novel energy configuration, Energy Storage Systems (ESSs) are emerging as one of the most effective and practical solutions to improve the stability, reliability and security of the novel smart grid architectures. In fact, they represent the compensation devices that allow the time shifting of electricity generation and load demand as well as the balance of the unavoidable mismatching related to forecasting errors of local demand and production, or system modelling. Particularly, battery technologies can be effectively exploited for these purposes: they are efficient and versatile storage technologies, some commercial chemistries being already mature for integrating RESs and providing smart grid services. Alongside stationary and centralised storage systems, distributed battery configurations have gained momentum. In particular, as electric vehicles (EVs) become more popular, the possibility of using on-board batteries as load-side distributed ESSs has been widely discussed in the technical literature. The related technology is called Vehicle-to-grid (V2G) and enable EVs to provide a variety of services to grid operators and customers. In this framework, the correct choice of storage technology, its optimal sizing in terms of capacity and rating power, and the development of adequate management strategies are presently considered some of the most important and challenging aspects to be investigated in order to facilitate the reliable integration of the smart grid architectures into the present distribution network.

This PhD dissertation proposes a number of approaches in order to deal with such typical issues of future active power systems, including optimal ESS sizing and modelling problems, power flows management strategies and minimisation of investment and operating costs. Chapter 1 introduces and describes main components of smart grids, particularly focusing on Concentrating PhotoVoltaic (CPV) technology and Battery Storage Systems (BESS). Such energy resources are deeply analysed in order to highlight advantages, issues as well as challenges for their effective implementation. Finally, some energy management strategies are presented, defining their field of application for the deployment of reliable smart grid control systems. In Chapter 2, several algorithms and methodologies for the management of smart networks, integrating RES generators and battery ESSs, are proposed and analysed. In particular, the management strategies here presented are based on rule-based (RBS) and optimal management (OMS) approaches. These are implemented in four cases of study, aimed at highlighting the potentialities of integrating ESSs and V2G technologies in different smart grid architectures. Although RBSs have demonstrated feasibility and effectiveness in the proposed scenarios, the best solutions, design or operating conditions can be ensured only by the optimal control approach. In this context, the optimal input profiles are obtained using suitable models that predict the system behaviour. Because of the presence of uncertainty, optimisation requires accurate modelling in order to actually reach optimality. In fact, a simple model could lead to significant system-model mismatching, being often insufficient to optimise the objective function in the real application. In the analysed cases of study, one of the most critical components is the BESS, which could need different degrees of modelling accuracy, depending on the particular application. Specifically, in dynamic optimisation problems a more complex mathematical formulation is often required in order to deal with dynamic and non-linear behaviours of battery-based storage systems. Additionally, since electrochemical ESSs group a number of technologies, an "all-purpose" model can hardly represent the peculiarities of each battery system. Therefore, based on prior knowledge and measurements from real BESS, *ad-hoc* battery models need to be developed and validated to ensure that their complexity and accuracy will be adequate for their final implementation. Therefore, in Chapter 3, the issues in modelling battery technologies are addressed, particularly referring to Lithium-Iron Phosphate and Sodium-Nickel Chloride systems. In the first case, a simplified and unified model of lithium batteries is proposed for the accurate prediction of charging processes evolution in EV applications. The proposed estimation algorithm aims at determining the duration of charge processes and battery voltage profiles at different charging rates, providing the sole information on the battery capacity, terminal voltage and SOC. In particular, the adopted electrical modelling has been experimentally validated on a Lithium-Iron Phosphate battery. The model is developed in order to be simple and accurate enough to allow its implementation in off-board chargers, enabling the on-line forecast of EV charging profiles, and the subsequent smart energy management of plugged EV fleets. Finally, in order to test different battery technologies and with the aim of verifying the actual performance of new storage candidates for smart grid applications, a dynamic electrical modelling is presented for a high temperature Sodium-Nickel Chloride battery (SNB). The proposed modelling is developed from an extensive experimental testing and characterisation of a commercial 23.5 kWh SNB, and is validated using a measured current-voltage profile, triggering the whole battery operative range. The aim is the development of an accurate model easily implementable in smart grids EMS and, hence, suitable for their on-line management and control.

Chapter 1

Smart Grids, Distributed Generation and Energy Storage Systems

1.1 Smart Grids and Active Networks

In the last years, the traditional and hierarchical organization of electrical power systems is worldwide facing a number of challenges posed by the increasing deployment of distributed generation (DG). Distributed energy resources (DER) usually supply local loads at distribution level by using non-conventional and/or renewable energy sources (RES) like wind power, solar photovoltaic systems, fuel cells, biogas and combined heat and power (CHP) plants. The current policies of connecting these generators are generally based on a *fit-and-forget* philosophy, in which DG is regarded as a mere passive element of the system. This approach can be ascribed to the traditional design and operation of passive distribution networks, characterised by unidirectional flows of energy. Although this philosophy has been demonstrated to be effective for relatively moderate penetration of this type of distributed generators, a massive integration of DER will significantly affect the planning and operation of the electrical power system. Such technical impacts are mostly related to power quality issues, voltage rise effect, branch overload problems as well as protection and stability concerns [1]. Therefore, in order to avoid restriction in the DG penetration level and preserve the integrity and security of the power system, the operational paradigm of distribution networks needs to change, evolving from an outdated passive management strategy toward a future grid active approach.

Active distribution networks are consequently considered the fundamental step to achieve an effective integration of DG in the distribution grid, making DER and, particularly, RES fully controllable and capable of providing system regulation and security services. Besides including flexible and intelligent control, active distribution networks should also employ modern information and communication technologies leading to the development of the Smart Grid (SG) paradigm [1–3].

In [4], the Smart Grid is defined as follows : "*A Smart Grid is an electricity network that can intelligently integrate the actions of all users connected to it –generators, consumers and those that do both–in order to efficiently deliver sustainable, economic and secure electricity supplies. A Smart Grid employs innovative products and services together with intelligent monitoring, control, communication and self-healing technologies to:*

- *better facilitate the connection and operation of generators of all sizes and technologies;*
- *allow electricity consumers to play a part in optimising the operation of the system;*
- *provide consumers with greater information and choice of supply;*
- *significantly reduce the environmental impact of the total electricity supply system;*
- *deliver enhanced levels of reliability and security of supply.*"

SGs are therefore characterised by advanced control and communication systems devoted to the synergistic management and coordination of generators, end-users as well as electricity market and systems operators. The aim is the maximisation of the overall efficiency and cost minimisation, maintaining at the same time the reliability, durability and stability of the system. To this end, smart grids rely on a number of devices, including smart metering, wide area active control, network management systems and advanced sensors. Moreover, demand side management (DSM) could play a crucial role in increasing the flexibility and controllability of the future smart systems [2]. In fact, demand response (DR) programs can be exploited to reduce the peak loads and enhance the local use of electric generation from RES. Energy Storage Systems (ESSs) are also widely required in order to allow a stable and reliable operation of SGs. ESSs can in fact improve the operating capabilities of the grid and address issues related to the variability of RES production. Another possibility is the use of plug-in electric vehicles (PEVs) to provide a variety of grid services. By properly coordinating their charging/discharging processes when connected to the grid,

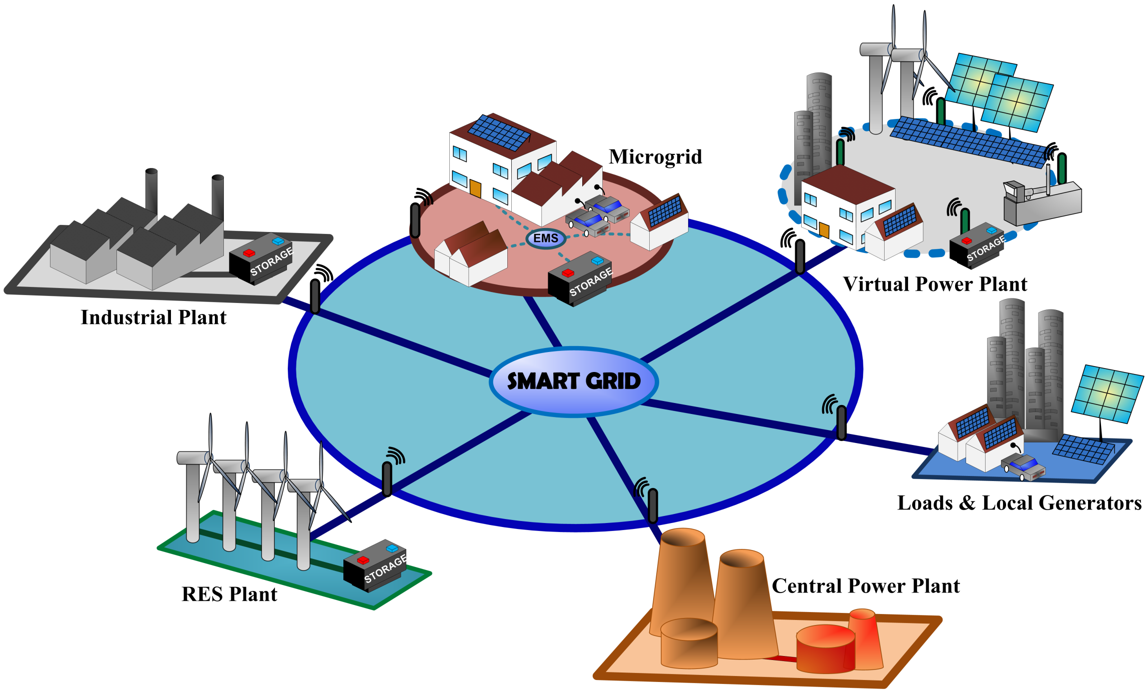

Figure 1.1: *Smart Grid architecture.*

they could de facto represent low-cost, highly controllable, and rapidly responding storage devices located near load centres. As can be observed in Fig. 1.1, the smart grid architecture is composed of several building blocks, essentially based on Microgrids (MGs) and Virtual Power Plants (VPPs) network structures. MGs and VPPs are two grid concepts that can be effectively applied in active network management of a smart grid, allowing the efficient integration of RES, end-users and storages in power systems. In particular, a MG is designed in order to supply both thermal and electricity local needs by aggregating and properly managing distributed generators, controllable loads and ESSs. The MG units are then controlled as a single power system in order to fulfil different goals, ranging from economic benefits for consumers, power quality, efficiency and reliability improvements for utilities, to the reduction of carbon dioxide emissions [1, 5–9]. These goals are achieved by adopting a smart and appropriate high-level coordination and control system, namely the Energy Management System (EMS), which receives in real-time the information about the status of each MG element as well as weather forecasts and market electricity prices, and synthesizes the most suitable set-point signals for each unit controller. Moreover, a MG is capable of working both in grid-connected mode and in island, separating and isolating itself from the utility's distribution during brownouts or blackouts. This ability makes hence the MG structure suitable to guarantee secure and optimal energy supply to continuous processes or in remote places, also in presence of power system failure. Practically, feasible islanding operation requires well-sized MG generation power systems and fast responding generating capacity, which can be achieved by suitable energy storage systems.

A VPP is an alternative active network management approach based on the clustering of demand and generation and on the adoption of a suitable network supervisory control. VPPs aim at aggregating DG, ESSs and customers in order to replace conventional power plant with more efficient and flexible systems. All resources are coordinated over a wide geographical area without need of physical connection. In fact, VPPs represent the "*Intenert of Energy*" concept which exploits software and Web-connected systems to remotely and automatically dispatch aggregated production and consequently enable the participation to the traditional trading market [8, 9]. To this end, a VPP can sell its electricity to the energy market or stipulate bilateral contracts with the customers (industrial or residential). It can take part in the Day-ahead, Intraday Market as well as in the auxiliary service market. As auxiliary service a VPP can not only offer active reserve for frequency control or reactive power reserve for local voltage control, but also power quality, communication or energy business services. Depending on roles and responsibility, VPPs are divided in two different types: Commercial (CVPP) and Technical Virtual Power Plant (TVPP). A CVPP aims at optimising the VPP from an economical point of view by offering competitive energy blocks and services without respect to network limitations. On the other hand, a TVPP aims at ensuring that the VPP is operated in an optimised and secure way [10, 11].

Although MGs and VPPs have a number of distinct differences, they are characterised by the same fundamental components, as schematically depicted by Fig. 1.1. These could be generally ascribed to the following categories: distributed generators, energy storage devices, controllable loads, energy management and control systems. In the rest of this Chapter, each MGs and VPPs element will be introduced and described, particularly focusing on Concentrating PhotoVoltaic (CPV) technology and Battery Storage Systems (BESS). Such energy resources will be then analysed in order to highlight advantages, issues as well as challenges for their effective implementation in the future smart active network configurations. Finally, some energy management strategies are presented, defining their field of application for the deployment of reliable MG and VPP control systems.

1.2 Distributed Generation

Distributed generation principally refers to small size generators connected to the distribution grid, characterised by rated powers ranging from few kW to tens of MW. A number of DG technologies are presently widely developed, examples of which include traditional generators in the form of small combined heat and power (CHP) plants and well-established renewable energy systems, such as wind turbines and photovoltaic (PV) panels.

A CHP plant is an integrated system that efficiently generates electricity and uses the heat from that process to produce steam, hot water, and/or hot air for other purposes. Usually, it is located at or near a building or facility with the main aim of satisfying at least a portion of the facility's electrical demand and utilising the heat generated by the electric power section in order to provide heating to the industrial/domestic thermal loads. A CHP system can typically operates in two different ways: electric-driven or heat-driven mode. In the former case, CHP units are controlled to supply electrical loads, while in the latter CHP plants are dispatched to meet the heat demand. This approach can lead to generation of electricity in excess compared to the facility requirements, which can be exploited to power the rest of MGs or VPPs loads.

Renewable generators are also important components of smart grids. Their installation in fact allows the reduction of green-house gas emissions from electrical power sector, while ensuring a less-dependence from fossil-fuel and introducing more variety in the electricity generation mix. Although established DG technologies include also geothermal generation and energy from biogas and biomass fuels, the most widespread RES systems in the DG field are presently based on wind and solar energy. In fact, wind plants and PV systems are more distributed in nature than other energy resources, their production being dependent only on weather and climatic conditions. Whereas wind turbines are commonly developed in the 1-5 MW power range, PV panels can be combined in a variety of sizes, obtaining systems from below 1 kW to hundreds of MW. For this reason, PV systems come with a greater flexibility than wind plants, making them suitable for a wider range of applications at the distribution voltage level. Particularly, PV modules can be installed to supply houses and residential buildings or to support energy-consuming production activities and industrial processes. As a consequence, PV generation is preferred and deployed worldwide as DER for local and isolated power systems electricity supply.

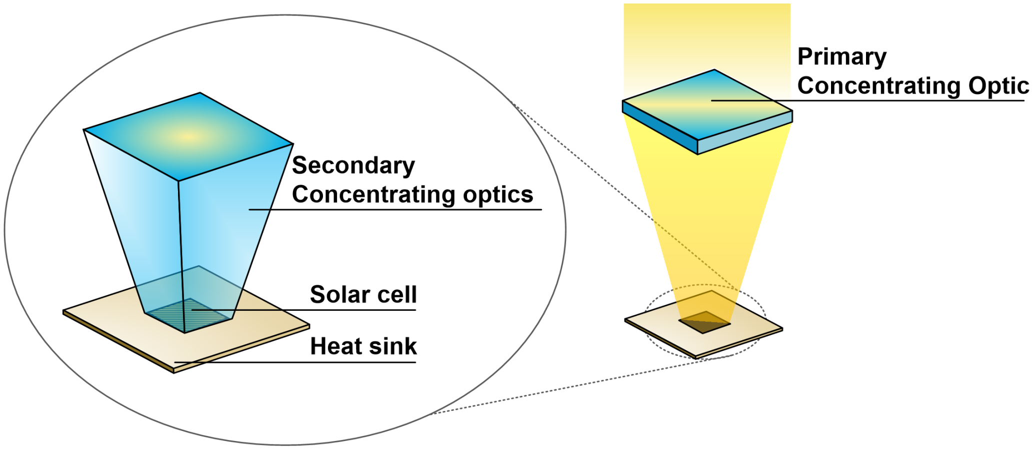

Figure 1.2: *CPV receiver and its main components.*

Solar PV cells convert global (direct and diffuse) sun radiation into electricity by exploiting the photo-electric effect. Commonly, PV modules are constituted of several silicon cells connected in series and/or parallel; additionally, they are mounted on fixed structure with a tilt angle dependent on the site and type of installation (e.g. roof mounting or ground-mounted). Silicon-based systems allow conversion efficiencies up to 25% and 22% for the single cell and panel, respectively [12]. These efficiency levels are relatively low compared to other renewable energy systems, such as wind or hydro technologies. Moreover, PV installations are characterised by a higher land-use, both on a capacity and electricity-generation basis. In order to address such issues, new PV concepts were recently developed. In particular, the Concentrating PV technology represents the most advanced PV system, which has already demonstrated its reliability and efficiency [13–17].

1.2.1 The Concentrating Photovoltaic Technology

The CPV basic element is the receiver, which is composed of the fundamental elements reported in Fig. 1.2. The main advantage in the use of this technology is represented by its potential to increase the efficiency, reducing at the same time the active material used for the energy conversion process. In fact, CPV receivers are characterised by optical systems that concentrate the solar direct radiation and, consequently, significantly increase the incident radiative power on the photovoltaic cells surface. As a consequence, the usage of expensive semiconductor material is reduced, proportionally to the concentration factor. CPV systems typically use III-V multi-junction (MJ) solar cells, which allow the extension of the physical energy conversion limit of a single photovoltaic material. In fact, MJ devices are characterised by a wider working irradiative bandwidth than traditional silicon cells [18], reaching efficiencies of 43% under concentrated light [12, 13]. It is worth noting that the approach followed to obtain such results requires the development of an integrated and complex system. As a consequence, some strict technical constraints need to be satisfied due to the necessity of concentrating and continuously focusing the Direct Normal Irradiation (DNI) on MJ cells with an even spatial distribution. Particularly, this requires a high precision dual-axis solar tracker which allows the sun radiation to focus continuously on the photovoltaic cells. In addition, a correct integration among the concentrator optics, solar cells and sun tracker is mandatory in order to obtain an efficient and reliable system. The complexity connected to the design, joint to the management and the maintenance of such a technology, is presently considered the main drawback for the CPV diffusion in the smart grid framework. Furthermore, as the electrical generation from CPV strictly depends on the daily trend of DNI, more variability is introduced, especially on short-term basis. In fact, CPV power production is subject to rapid variations and fluctuations since the direct component of solar radiation can drop to zero in few seconds in presence of clouds. This implies a short-term intermittency of CPV generation, showing dynamics much faster than those of traditional PV systems. Such a behaviour can be better understood by looking at Fig. 1.3, where the profiles of CPV power output and DNI are reported for a partially cloudy day. The higher degree of uncertainty and variability of supply, combined with the dependence from the tracking error occurrences, makes the forecasting and dispatch of CPV production a complex task, adding challenging operating conditions for the energy management of electricity grids. The necessity of having a reliable control for the deployment of active networks implies the knowledge of actual performance of each resource. In the case of CPV plants, extensive characterisation and modelling studies are hence required in order to facilitate their integration as distributed generators. In the following, some characterisation studies and performance analyses carried out on different CPV technologies are presented, aiming at highlighting the main features and issues of these renewable systems.

1.2.1.1 Characterisation studies

At the present time, several photovoltaic companies and research groups have worldwide developed a number of CPV solutions with the aim of increasing the system effi-

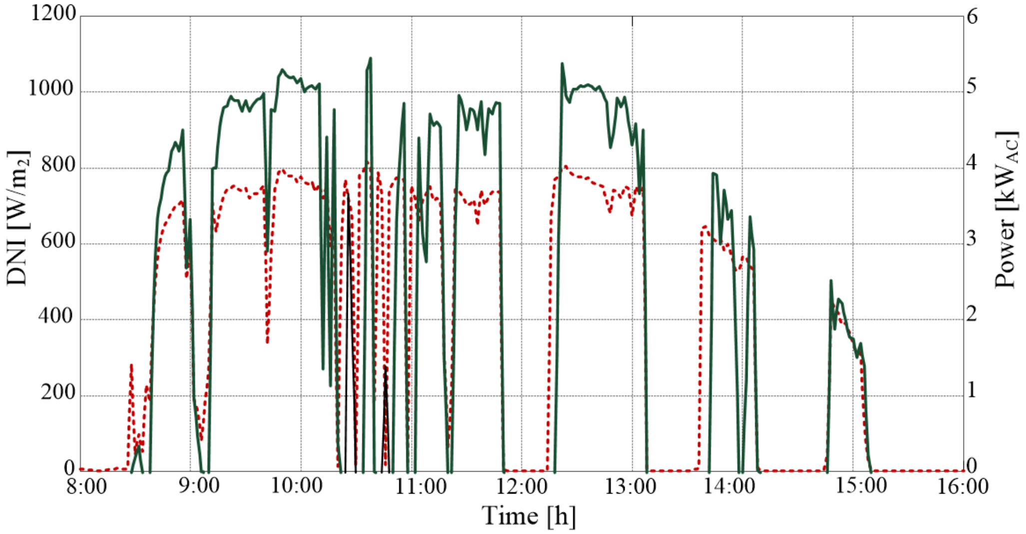

Figure 1.3: *Measured daily profiles of a CPV plant power production (green) and DNI daily evolution (dashed red) during a partially cloudy day.*

ciency and reducing costs, obtaining a more competitive product on the photovoltaic market. In particular, based on the geometry of the optical configuration, CPV technologies can be divided in refractive and reflective optics-based systems [19]. Examples of CPV modules implementing these two optical solutions are reported in Fig. 1.4 for the sake of clarity.

So far, most commercial CPV modules employ refractive optics (mainly Fresnel lenses) because of their relatively low cost and reduced system complexity. In fact, Fresnel lenses are usually made with low cost PMMA material characterised by a typical thickness of 4-5 mm. However, this optical configuration introduces chromatic aberration phenomena which contribute to the degradation of the overall system performance [20]. Moreover, the spatial distribution of concentrated radiation is a critical issue and can cause an incorrect heating, leading to hot spot effects that increase the series resistance and the solar cells degradation. To overcome this problem, a secondary optical element, namely the homogeniser, is commonly installed. The implementation of this solution allows to increase the acceptance angle of CPV receivers and reduce the effect of optical misalignment and tracking accuracy losses [18].

In the reflective optics-based systems, a Cassegrain configuration is typically adopted despite the fact that parabolic mirrors can be used as well. Cassegrain-type concentrators are characterised by higher complexity than Fresnel lenses since they

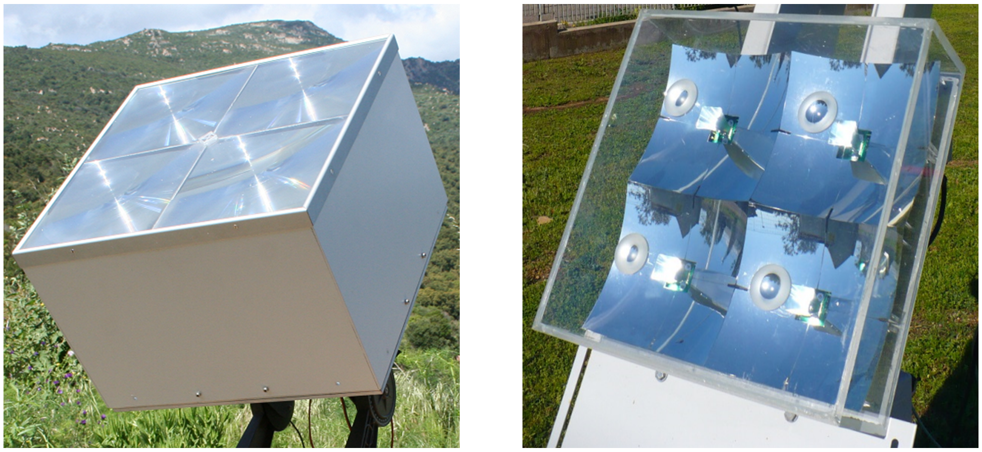

(a) (b)

Figure 1.4: *Examples of CPV modules. (a) Refractive and (b) Reflective configurations.*

are based on a double reflection system, composed of a main collector and a secondary reflector. In order to make uniform the concentrated radiation pattern and increase the acceptance angle, an optical homogeniser is also implemented. In this case, the optics design inputs are less challenging, permitting the implementation of simplified non-imaging optics. In fact, these systems are not affected by chromatic aberrations and hence a correct optical alignment is required only in the design phase.

A critical issue common to both CPV configurations is related to the design of the heat sink, which can strongly influence the system conversion efficiency. In fact, the cell temperature can rise considerably under concentrated light, causing a significant drop in the open circuit voltage and negatively affecting the maximum delivered DC power and, consequently, the overall system performance and reliability [21].

Considering the quite new concept of CPV applied to DG, extensive characterisation studies are hence necessary in order to evaluate the feasibility of this RES technology in smart grid applications. To this end, several tests have been carried out on the two receiver prototypes shown in Fig. 1.4. Such experimental analyses have included electrical and optical characterisation studies, thermal investigations as well as light soaking tests.

Experimental set-up. The CPV receivers have been electrically and thermally tested by means of the outdoor experimental set-up depicted in Fig. 1.5a, whereas the optical characterisation has been performed using the indoor test system illustrated in Fig. 1.5b.

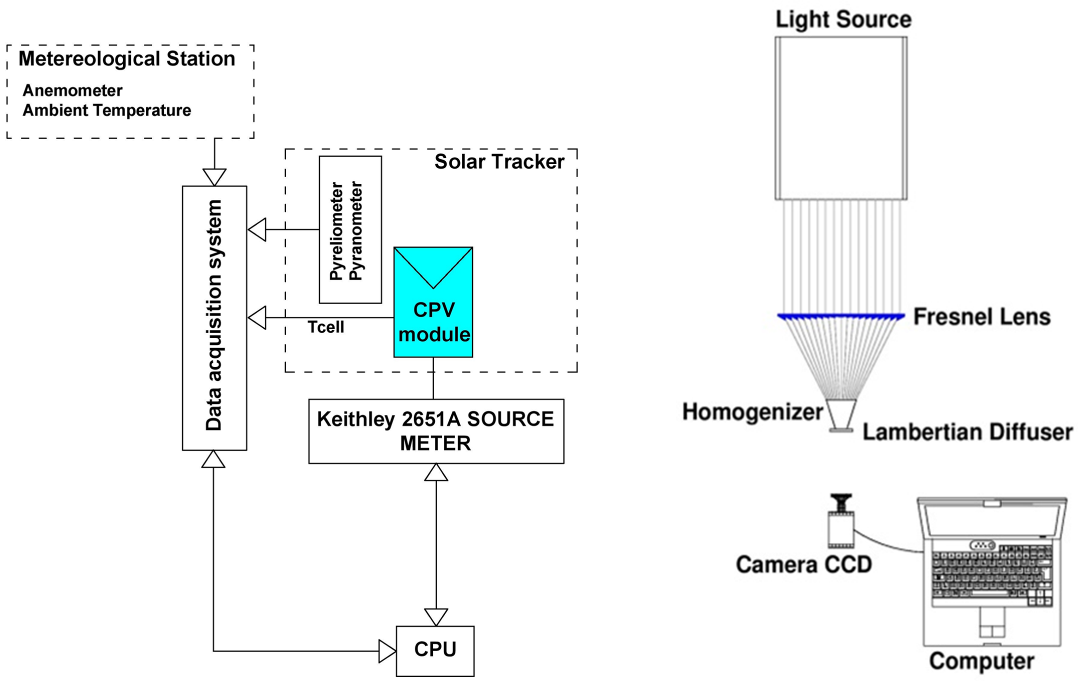

(a) (b)

Figure 1.5: *Experimental set-up for CPV characterisation. (a) Outdoor test system for electrical and thermal analyses (b) Indoor test system for optical analyses.*

The adopted outdoor experimental set-up consists mainly of a Keithley 2651A high power source-meter, used both as I-V curve tracer and as MPPT unit. The device is controlled by a laptop PC (CPU), running Virtual Instruments (VIs) specifically developed in the NI-Labview environment. All measurements can be monitored on-line from the host computer through the VIs Graphical User Interface (GUI), as shown in Fig. 1.6a. In order to acquire a complete I-V curve, the source-meter is programmed to automatically generate variable voltage steps and acquire current and voltage operating points, depending on the user settings. In the GUI, the module performance and operating parameters, obtained processing the measured data, are then numerically displayed, while resulting I-V and P-V curves are plotted in a X-Y graph. Additionally, the outdoor facility of Fig. 1.5a includes a meteorological station, exploited to acquire ambient parameters, such as DNI, Global Normal Irradiance (GNI), external temperature, wind speed and direction as well as relative humidity. The CPV cell temperatures are measured by means of either NTC thermistors or PT100 probes, which can be placed both in the direct proximity of the

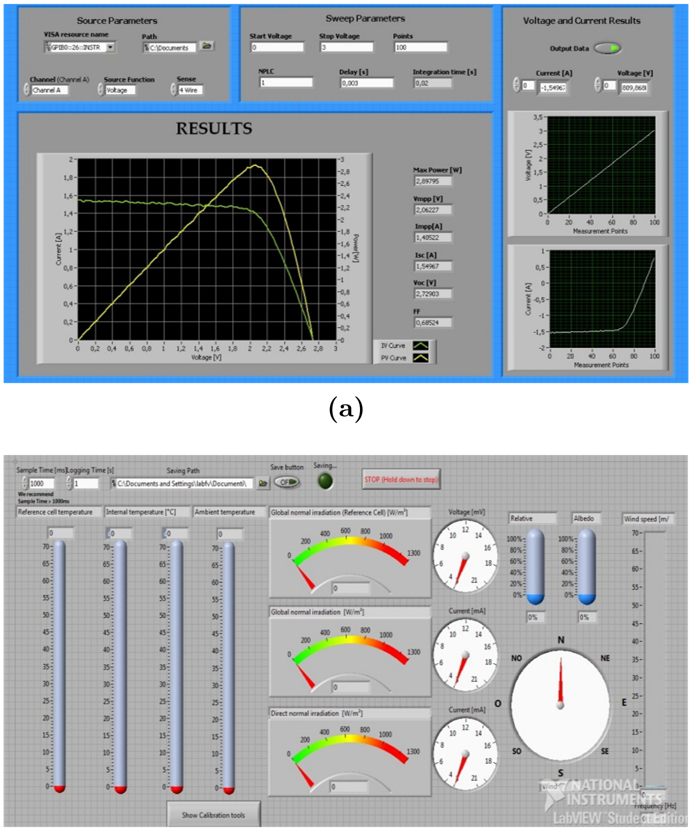

Source Parameters
VISA resource name: GPIB0::26::INSTR
Path: C:\Documents
Channel (Channel A): Channel A
Source Function: Voltage
Sense: 4 Wire

Sweep Parameters
Start Voltage: 0
Stop Voltage: 3
Points: 100
NPLC: 1
Delay [s]: 0,003
Integration time [s]: 0,02

Voltage and Current Results
Current [A]: 0 -1,54967
Voltage [V]: 0 809,8681

RESULTS
Max Power [W]: 2,89795
Vmpp [V]: 2,06227
Impp[A]: 1,40522
Isc [A]: 1,54967
Voc [V]: 2,72903
FF: 0,68524

(a)

Sample Time [ms]: 1000
Logging Time [s]: 1
We recommend Sample Time > 1000ms
Saving Path: C:\Documents and Settings\labfv\Documenti\
Reference cell temperature: 0
Internal temperature [°C]: 0
Ambient temperature: 0
Global normal irradiation (Reference Cell) [W/m²]: 0
Global normal irradiation [W/m²]: 0
Direct normal irradiation [W/m²]: 0
Relative: 0%
Albedo: 0%
Frequency [Hz]: 0

(b)

Figure 1.6: *Experimental set-up for CPV characterisation. (a) Outdoor test system for electrical and thermal analyses (b) Indoor test system for optical analyses.*

photoactive area and on the back of the module. All sensor signals are acquired by a NI-SCXI data acquisition platform, controlled by a proper VI that automatically acquires, elaborates and stores the environmental and module temperature data. The resulting measurements and acquisition settings are monitored in the related GUI, shown in 1.6b. The described testing equipment enables the simultaneous acquisition of atmospheric variables, CPV electrical and thermal parameters, which are also sampled at the same time intervals. Therefore, the performance of the CPV module can be studied and analysed under real operating conditions, evaluating the weather patterns on the system power and efficiency. The experimental set-up implemented for the optical characterisation and shown in Fig. 1.5b is used to evaluate the uniformity of the irradiance distribution on the cell plane, produced by the CPV receiver optics. The solar simulator Sun 2000 11048 by Abet Technologies is exploited as light source. In order to understand how the optical elements spatially modify the

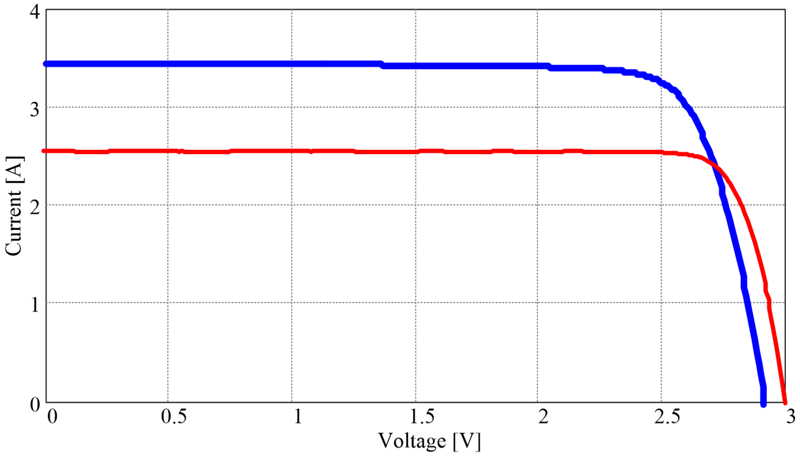

Figure 1.7: *I-V curves for the reflective (blue) and refractive (red) CPV receivers.*

light distribution, the irradiance profile is captured by a CCD camera. The method uses a Lambertian diffuser placed at the focus of the primary collector, e.g. a Fresnel lens. The diffuser receives the concentrated light over the front side and transmits it on the back side, producing an image of the irradiance distribution of the incident light [22]. The spot image is then captured by the CCD camera located behind it and finally processed using the Matlab software.

Performance Analyses. Several tests are carried out on the reflective and refractive prototypes of Fig. 1.4 in order to deeply understand the main factors influencing their performance. Firstly, the two CPV systems have been electrically characterised, extracting I-V curves and main electrical parameters, such as the open-circuit voltage (V_{OC}), the short-circuit current (I_{SC}), the maximum DC power (P_{max}) and efficiency (η). Referring to tests performed at 900 W/m^2 DNI, obtained results are well-summarised in Fig. 1.7 and in Table 1.1. Although the two modules are based on different technologies and show slight differences in the MJ cell characteristics, both have demonstrated to have reliable performance when optimal operating conditions are considered, which means central hours of sunny days characterised by the

Table 1.1: *Refractive and reflective CPV prototypes: comparison of receivers performance*

	$\mathbf{V}_{OC}$ [V]	$\mathbf{I}_{SC}$ [A]	$\mathbf{P}_{max}$ [W]	η [%]
Refractive Receiver	2.92	3.45	8.13	22.4
Reflective Receiver	2.97	2.60	6.70	21.6

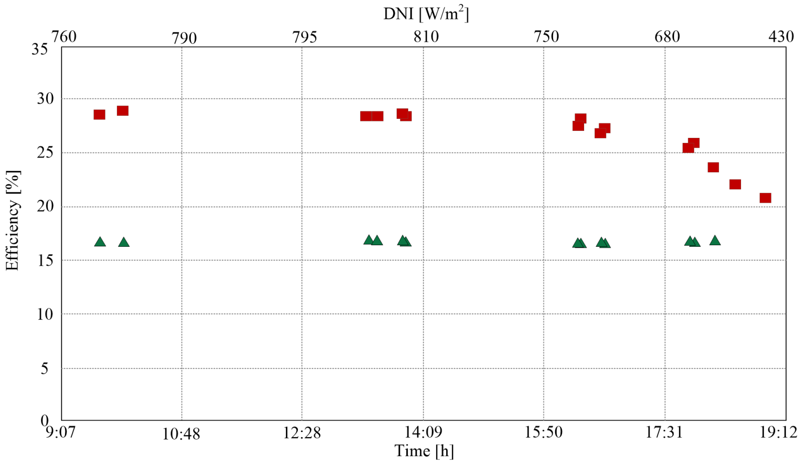

Figure 1.8: *Comparison between the efficiency of the CPV module based on MJ solar cell (red square) and a reference silicon solar cell (green triangle).*

highest values of direct radiation. However, as the atmospheric conditions change during the day, in terms of humidity and air mass, the spectrum of the solar radiation at the ground undergoes to daily variation. In particular, the blue portion of the solar spectrum is progressively absorbed or scattered as the air mass increases. In MJ devices, the junctions are connected in series and the current flowing in the device is determined by the junction that generates the lowest photo-current, which is usually the top one, more sensitive to the blue radiation. In late afternoon, as the blue portion of the solar spectrum is progressively absorbed or scattered, the top junction generates a lower current and thus chokes the current flowing in the whole device. As can be seen from Fig. 1.8, the efficiency of the CPV receiver based on MJ solar cell decreases progressively during the day. As a reference, in Fig.1.8 the efficiency measurements of a standard silicon cell are reported, as well. The efficiency trend of the reference silicon cell is basically constant, which reveals that the spectral mismatch for single-junction solar cells is negligible and the temperature variations are not large enough to justify the performance drop registered in MJ solar cells.

Regardless of such tests, MJ solar cells are expected to undergo high temperature at operative conditions because of the great power density levels impinging on the receivers. In fact, the electrical conversion efficiency of a solar cell greatly depends on its operating temperature, decreasing as the temperature rises. These effects are considerably enhanced under light concentration, suggesting the need of a complete monitoring of thermal performance. Different tests have been carried out on the CPV prototypes in order to determine the temperature profiles in real op-

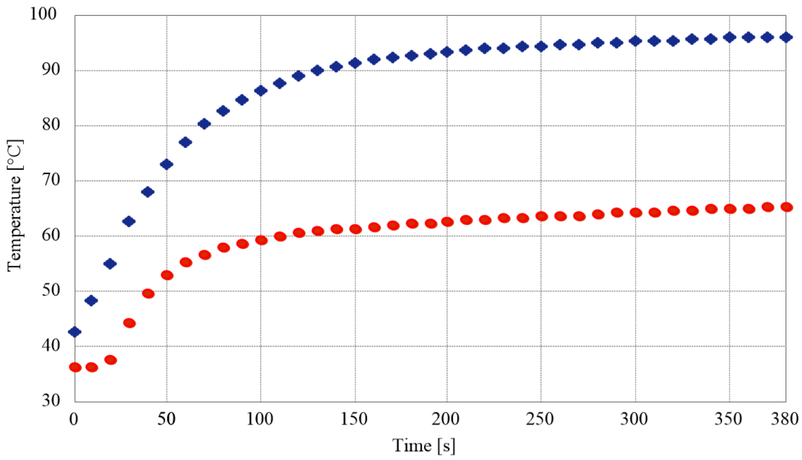

Figure 1.9: *Temperature evolution for a CPV receiver considering two heat sink configurations: simple metal plate (blue) and improved system with high thermal conductivity compound (red).*

erating conditions and investigate to what extend their thermal dynamics influence the module performances. The results here reported refer to measurements carried out on a three hours time-window at a mean DNI value of 900 W/m^2 and ambient temperature of 30-35°C. The experimental data reported in Fig. 1.9 show as an non-optimised thermal management can result in an extremely fast rise in photovoltaic cells temperature, hitting the value of 100°C in less than 10 minutes. Such a temporal evolution of the temperature has entailed a drastic drop in the module performance. For instance, at the end of the test, the efficiency had decreased by 10.4% respect to the initial value. These outcomes clearly point out the importance of correctly managing the operating temperature of a CPV module. In order to match the temperature constraints of the CPV devices, the CPV receivers have been subsequently equipped with heat sinks engineered to be thermally coupled with the back-panel of the module. The contact thermal resistance between solar cell and heat sink has been reduced using high thermal conductivity compound. As can be observed in Fig. 1.9, the better heat dissipation obtained with this second configuration lowers the final temperature to 30°C respect to the first solution, leading to stable thermal operations and reliable performance.

Another important concern in the operations of CPV systems is related to the non-uniformity of the irradiance distribution on the cell plane, introduced by the optics. In particular, the non-uniformity of the concentrated solar light causes high illuminated areas and hot spot phenomena which result in an increase in the effective

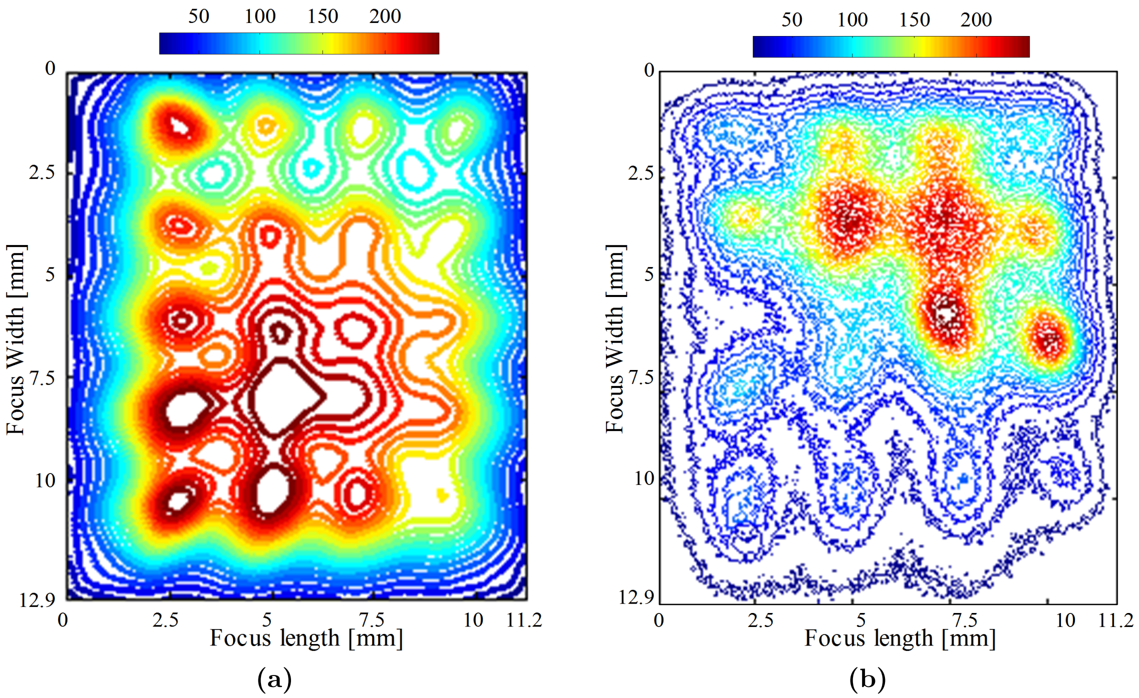

Figure 1.10: *Light distribution on the cell plane. (a) Fresnel lens. (b) Reflective homogeniser*

series resistance. This in turn translates into a drop in the efficiency, affecting the overall solar cell performance. Following these considerations, the irradiance spatial distribution of CPV devices should be carefully analysed. In the scientific literature, the effects of inhomogeneous illumination on the CPV solar cell plane have been commonly evaluated by simulations based on distributed circuit models [23]. However, simulations provide reliable results only if accurate data for the solar cell distributed model are available and the irradiance profiles over the cell are known. Illumination patterns are usually simulated starting from optical system models which can hardly reproduce the actual profiles produced by manufactured optics accurately [24]. Therefore, the indoor test system illustrated in Fig. 1.5b has been used, obtaining the irradiance profiles at the exit of the CPV optical system reported in Fig. 1.10. In particular, Fig. 1.10a shows the irradiation distribution on the primary collector focal plane. As can be observed, this flux distribution determines areas illuminated at an irradiance level 250 times higher than the less irradiated ones, leading to an increase in the effective series resistance and, therefore, to a drop in the fill factor. At the same time, non-illuminated areas work as dark diodes, contributing only with recombination current but not with photo-generation. The introduction of a secondary optical element, i.e. the reflective homogeniser, has the purpose to improve the uniformity of the irradiance distribution over the triple-junction solar cell. As can be noticed from Fig. 1.10b, the geometrical characterisation and the flux mapping demonstrate a poor spatial irradiation uniformity, with several hot spots concentrated on the top-right region of the cell area. The presence of localised high intensity peaks is one of the main reasons of the module degradation. This suggests the importance of considering the effect of inhomogeneous illumination on the CPV system power output in order to obtain a more accurate estimation of its effective operating performance.

Final Remarks. The characterisation studies and analyses presented in the foregoing paragraphs highlight the complexity of the CPV technology, its power production and efficiency depending on a number of factors. These include not only the direct irradiation but also MJ cell operative temperature, air mass and solar spectrum as well as pointing accuracy of the dual-axis solar tracker and hot spot phenomena due to optical misalignment. As a consequence, the estimation of CPV production results in a multifactorial task, which adds more issues for the accurate forecasting of CPV generation. Moreover, the high variability and short-term dynamics introduced by these systems pose challenging operating conditions, forcing the installation of storage systems in order to make the CPV production dispatchable and programmable, enabling its effective integration in active networks.

1.3 Electrical Storage Technologies

Electrical Energy Storage (EES) refers to a system able to convert electrical energy into a form that can be stored and then converted back to electricity when needed. The concept behind EESs is clearly not new, since large-scale Pumped Hydroelectric Storage (PHES) is historically recognised and deployed as a fundamental component of the high voltage power grid. However, several drivers are currently emerging to support the installation of alternative EES technologies, especially at the distribution grid level. These factors include: the rise in stochastic generation from RES, an increasingly congested infrastructure, the development of smart grids as building blocks of the new distribution grid architectures as well as the increased need for flexibility, reliability and security in electricity supply. In order to deal with the above

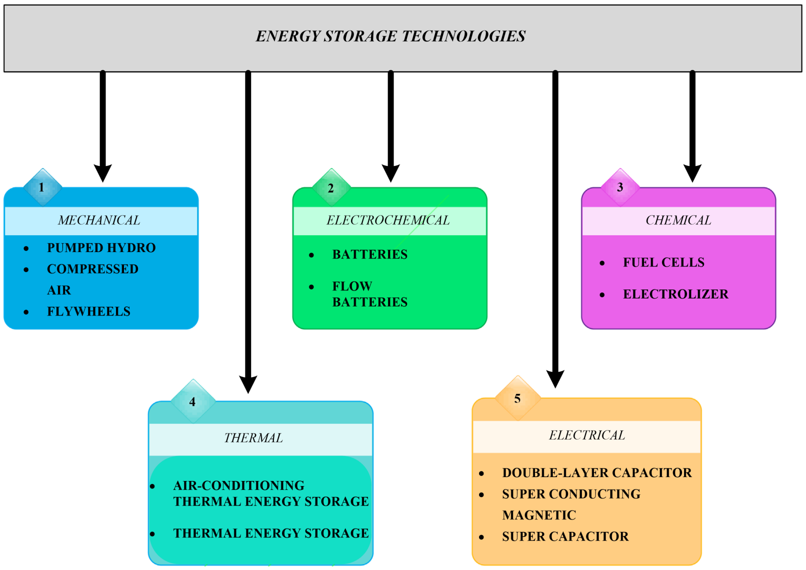

Figure 1.11: *Classification of electrical energy storage.*

issues and challenges, a number of EES systems have been extensively investigated, some of them having already demonstrated their feasibility in several stationary applications [25].

Electricity storage technologies can be categorised based on two different criteria: physical operating principle and function [26]. The first approach is widely adopted for classifying EESs, and takes into account the form of energy used to store electricity. A complete classification of EES types is accordingly presented in Fig. 1.11, based on [10]. In terms of the function, EES systems can be divided in two main classes: the first includes the technologies intended firstly for high power ratings, while the second comprises the EESs designed principally for energy management purposes. The area of application for specific electricity storage technologies is restricted by physical, technical and economic limitations. For example, PHES plants have been conventionally considered for bulk energy storage because of their high-energy density characteristics, but their development implies the availability of adequate sites for two reservoirs, long lead time for the construction, as well as environmental considerations [27]. On the other hand, Flywheels (FES) and Super Capacitors (SCES) are mainly intended for high power/short duration applications [26, 27]. However, they are high costly technologies, being suitable for a limited range of applications, e.g in the electric vehicles propulsion systems or hybrid EESs, generally in combination with batteries.

Among these various EES technologies, batteries storage systems (BESS) are the most suitable for MGs and VPPs. In fact, electrochemical batteries are more efficient and flexible EES than PHES, FES or SCES: they can be installed regardless of geographical and land occupation constraints, which make them suitable for domestic and residential installations, as well. Additionally, batteries size can be designed ranging from a few kWh to several MWh and some electrochemical technologies can be applied to both power and energy management applications. For these reasons, they are likely to be widely adopted in the novel smart grid configuration [10]. A battery works by converting chemical energy into electrical energy by means of various chemical reactions. In the past and recent years, a wide range of different combinations of anode, cathode, and electrolyte materials have been investigated in order to develop the best trade-off between cost and performance. These efforts have been resulted in a number of BESS technologies, characterised by different degrees of commercial maturity and availability. The following sections provide an overview of the main types of batteries that can be successfully applied in the active network and smart grid context.

1.3.1 Batteries Storage Systems

1.3.1.1 Lead-acid batteries

Lead acid (LA) battery represents the oldest and more widespread BESS technology, being adapted during years for use in various applications. It is mainly used as automotive starting, lightning, ignition (SLI) and main storage system in light-duty electric vehicles (e.g. golf kart and lift trucks) as well as for stationary storage applications, such as uninterruptible power supply (UPS) and emergency ESS in power stations [27, 28]. The worldwide diffusion of this battery is primarily related to its easy manufacture in a wide range of capacity sizes and to its relatively low cost. However, the high specific weight, moderate cycle-life and reduced discharging capabilities have limited their range of applications, LA batteries being unsuitable for renewable integration and smart grid projects.

1.3.1.2 Lithium-ion batteries

The Lithium-Ion (Li-Ion) battery technology has recently emerged as the most promising BESS on the market, specifically because of several characteristics that make this battery type more suitable than other technologies in a variety of applications. In fact, Li-Ion batteries show the highest energy density, conversion efficiency and cycle-life as well as the lowest weight among all rechargeable BESS [27]. Therefore, besides being already widely employed for consumer and portable electronics, Li-Ion batteries are now becoming the leading storage technology for plug-in hybrid electric vehicles (PHEVs) and all-electric vehicles (EVs), as well. However, there are still some challenges for developing large-scale Li-ion batteries. In particular, cost and safety issues are the two main factors that obstacle the deployment of lithium-ion for widespread use in power systems. Cell degradation and thermal runaway due to overcharge and underdischarge phenomena require special packaging and internal protection circuits, increasing complexity and costs. In order to overcome such criticalities and meet the cost and safety requirements for ESS applications, Li-ion batteries have been designed in a range of different chemistries, each with unique cost and performance characteristics. Considering cathode materials, lithium iron phosphate ($LiFePO_4$) based batteries are emerging as promising candidate for both EES stationary and vehicular applications, due to its low cost and reduced environmental impact as well as high stability [11, 29, 30]. The latter is in fact essential in order to avoid safety issues due to thermal runaway at high temperatures. Thanks to the improvements in Li-Ion technologies, stationary systems have been recently deployed, demonstrating the feasibility of this battery type for frequency regulation and spinning reserve services, RES integration and distribution grid support [31].

1.3.1.3 Molten salt batteries

Sodium-sulphur (NaS) and Sodium-nickel chloride ($NaNiCl_2$) batteries are based on a liquid sodium negative electrode and operate both at high temperatures, above 250°C. The development of these electrochemical cells have been driven by the need of identifying combinations of materials characterised by both low cost and high specific energy. Moreover, because of their high internal temperature, operations of molten salt batteries are independent from the ambient thermal conditions making them suitable for applications in extreme climates, where other BESS typologies can be not effectively employed.

NaS batteries are a relatively commercial mature and attractive candidate for large-scale EES systems, finding applications in wind power integration and high-value grid services, such as load-leveling or peak shaving [31]. In fact, they are generally used for energy-density applications, being able to sustain discharge processes for long time-periods . This system is composed of a liquid sodium anode separated from the sulphur cathode by a ceramic electrolyte (β''-alumina), which allows the migration of sodium-ions while acting as a good electric insulator. The cell needs to be operated at high temperatures, between 300°C and 350°C, which are required to maintain the electrodes in molten states and ensure efficient ion transportation through the ceramic solid electrolyte. Although NaS features very interesting properties for stationary ESS, such as very high specific energy and cycling flexibility, it is still facing some challenges especially related to safety problems and incident risk [32]. In fact, the direct contact of electrodes can results in fires and explosion, mining the feasible and secure deployment of this technology in large-scale storage systems.

In Sodium-nickel chloride batteries, the positive electrode is in solid state and based on nickel element. This configuration requires the presence of a second electrolyte in liquid state (sodium chloroaluminate, $NaAlCl_4$) in order to improve the ion conductivity of the electrode. In case of damage or solid electrolyte structure failure, the sodium chloroaluminate reduces the effects of the exothermic reaction, leading to continuous and safe operations of the ESS plant, without risk of fire or explosion. The intrinsic safety and the wide variety of applications, ranging from residential to grid support services, are encouraging the installation of such a technology in several projects, including RES integration and frequency/voltage regulation [31, 33], However, further improvements are needed in order to increase energy density and power capability, and to lower specific costs.

1.3.1.4 Flow batteries

Redox flow battery (RFB) represents one of the most recent and advanced BESS technology, being based on a novel electrochemical structure, which make them more similar to fuel cell storage systems than traditional batteries. In fact, RFBs is constituted of two external electrolyte tanks storing the solvable redox couples, and of reaction stacks where the liquid electrolytes are pumped in, converting chemical energy in electricity. This peculiar electrochemical structure results in one of the more interesting features of such a technology: the capability of coming with independent size of power and energy. Particularly, power is a function of the number of cells that are stacked, whilst energy depends on the electrolyte volume, which is circulated by pumps. Moreover, RFBs are characterised by high flexibility, high depth-of-discharge, long durability and fast responsiveness [34]. Such features allow for a variety of power and energy applications, ranging from power quality to energy management services. Among various RFB technologies, the leading chemistries at the present is the Vanadium Redox battery (VRB), which is in fact the sole that has reached effective commercial maturity. Although VRB systems are already been successfully demonstrated in test and commercial plants, capital and cycle life cost reductions as well as improvements in power and energy densities and further development in electrochemical materials are still required in order to obtain a commercial product widely deployed for smart-grid-oriented applications [27, 34].

1.3.2 EES stationary applications for smart grids

EESs can be effectively deployed in order to support reliable operations of MG and VPP systems as well as transmission power networks. However, these applications still require to EESs different functions and energy/power capabilities. For instance, at the utility grid level, storage systems need to carry out a number of short-duration high-power functions, such as frequency regulation or RES fluctuations compensation. However, at the same time, they are demanded to support power system planning and operation activities (i.e. transmission and distribution upgrade deferral, load following and electric energy time shift), requiring long-duration energy management capabilities. Therefore, for grid-scale applications, the deployment of large energy capacity and power density energy storage systems is a mandatory necessity, which still requests further improvement in technologies and reduction of specific costs. On the other hand, energy storage is a fundamental component of active smart networks since the development of MGs and VPPs can not overlook the primary role of EES in a number of system services, including maintaining energy balance and power flexibility, facilitating the integration of RES and improving power quality [35]. In this case, the smaller capacity and lower initial costs facilitate the diffusion of several EES technologies in the SG context. Moreover, these storage installations could represents a test environment for EES systems, allowing the development of models and performance studies which could be further applied to utility grids, as well.

1.3.2.1 Energy balance and power flexibility

Balancing and flexibility are two main functionalities offered by storage systems. Within SGs, the reliability of power supply is a fundamental requirement which implies the management of all energy resources in order to maintain a balanced and efficient power system. In the MGs framework, the need for grid stability and flexibility is particularly related to the presence of a large number of variable-generation resources, such as wind and solar. Moreover, the ability of a MG to be disconnected from the utility grid and to operate at islanded mode, requires suitable compensation device driving the transition from the grid-connected mode. Power and energy capabilities of most EESs as well as their high dynamic responses can be effectively exploited for these types of applications, operating as both short-term electricity suppliers and power compensation devices. In addition, EES may act as emergency power buffer for critical customers during fault situations.

1.3.2.2 Renewable energy resources integration

Although RES power plants are the main energy resources of active networks, their reliable integration poses a number of challenges, especially due to the intermittent and variable nature of their productions. In fact, the increasing connection of RES generators add volatility to the grid supply and load balance. Because of the critical need to instantaneously balance supply and demand, SGs and, particularly, MGs need flexible and dispatchable energy storage resources, which can buffer the renewable power output by storing surplus energy and re-delivering it in periods of low generation. Besides being used as energy buffers, EESs are also needed as power compensation devices in order to counterbalance the rapid and unpredictable fluctuations of RES generation. Storages can in fact used to smooth the production of variable RES plants, making their power output more reliable and dispatchable. Therefore, both the buffering and power flexibility offered by EESs enable active networks to integrate increasing capacity of intermittent RES systems [7], optimising their operations and the exchange of power with the main grid.

1.3.2.3 Arbitrage

Price arbitrage implies the use of EES systems for retail electric energy time-shift in order to reduce the overall cost of electricity. In this application, the spread between peak and off-peak prices can be economically exploited by EESs. In fact, storage devices can purchase and store energy from the grid when electricity prices are low, and then sell and discharge during on-peak time periods. By implementing high-energy density EES technologies, a MG or VPP can thus effectively enable arbitrage functions.

1.3.2.4 Power quality service

The electric power quality service involves using storage to protect SG resources against short-duration events that affect the quality of power. Thanks to the combination with power electronics-based interfaces, EES systems can regulated their output in terms of both active and reactive power, improving and regulating power quality of MG and VPP customers. Suitable EES technologies can be further exploited to smooth out transient disturbances, such as voltage sags and short-term spikes, harmonics and instant power shortage. Typically, these applications require discharge duration ranges from a few seconds to a few minutes; particularly fast-response and fast-ramping EESs are necessary in order to tackle with sudden voltage variations.

1.3.3 Vehicle-to-grid Technology

As smart grid and active network configurations become more widespread, the need for distributed battery systems are increasing, as well. Furthermore, the simultaneous transformation in the automotive sector is leading to the diffusion of new electrified mobility forms, such as battery electric vehicles (BEVs). In these systems, a battery storage is used to power the vehicle, representing the key component for enhancing the electric mobility and for the integration between the vehicular field and the power grid. Consequently, as plug-in electric vehicles (PEVs) become more popular, the possibility of using on-board batteries as load-side distributed EES systems has been widely discussed in the technical literature [36–48]. In particular, the future impact of PEVs on performance and economics of electricity networks is one of the main concerns related to the diffusion of electric vehicles. In this context, the Grid-to-Vehicle (G2V) and Vehicle-to-Grid (V2G) technologies are typically considered as possible solutions. These enable the interaction between the smart electrical network and PEVs in two different ways:

- Under the traditional G2V paradigm, PEVs behave exclusively as electricity loads, demanding energy when they are connected to the grid in order to charge their storage systems.

- Under the V2G paradigm, PEVs could behave both as electricity consumers and electricity suppliers.

A variety of grid services could be provided to grid operators and customers by appropriately managing BEVs when connected to the grid, even applying the sole G2V approach. In this case, PEVs can be considered as controllable loads, managing their charging processes by exploiting DSM and DR strategies. Although G2V is presently more easily implementable, the most promising technology for BEVs integration into the SGs is certainly the V2G, which enables their management as distributed ESSs. This consideration is based on results of several analyses that take into account the actual number of cars per capita, average utilisation factors as well as time and space correlation between electric energy and car use [37–39]. In fact, the vehicles are usually parked for 90% of the time, constituting idle electrochemical resources which might be used for several network services, provided that a connection to the grid is in place. In particular, the wide-scale diffusion of V2G could enable PEVs to provide extra power supply, peak load shaving, load shifting and support to renewable energy resources exploitation. To this end, an aggregative structure is necessary since competitive energy blocks and auxiliary services in energy markets can not be offered by a single BEV's owner, but can be provided by their aggregation [36]. Essentially, the aggregator acts as an intermediary between each BEV's user and the SG central control, managing BEV batteries with the aim of primarily ensuring the mobility customer requirements, but offering, at the same time, network balancing services. This requires the adoption of proper management strategies, which should consider driver mobility needs, V2G economy as well as demanded regulation performance.

1.4 Energy Management Strategies

In a smart grid configuration, the coordination of the energy and power flows is performed by the Energy Management System (EMS). The EMS represents the MG (VPP) central controller and its main objective is to define and synthesises the most suitable power set-points signals for DGs, ESSs and controllable loads, based on real-time operating conditions of components and system status as well as weather forecasts and market electricity prices. Therefore, the EMS serves as a gateway between the distribution network operator (DNO) or market operator (MO) and the local controllers (LCs), associated at each DG, ESS and load unit [49]. On the basis of system set-points or price inputs sent from DNO and MO, the EMS determines the optimal operating condition of local units according to a certain objective function (e.g. minimisation of energy costs and fuel consumption or maximisation of system energy autonomy). Finally, the power scheduling set-points are transferred to LCs, which accordingly regulate the corresponding power output, depending on physical constraints of DG and ESS unit. EMS central controllers rely on suitable algorithms, which can be based on a number of management strategies. Generally, these are formulated as optimal control problem since the EMS purpose is the minimisation of a performance index defined over an extended period of time (e.g., one day) by using a sequence of instantaneous control actions. Several methods can be used for its solution, being mainly subdivided in four categories: numerical optimisation, analytical optimal control theory, instantaneous optimisation, and heuristic control techniques. In the first two cases, the problem is considered in its entirety, i.e. taking into account at each instant information related to past, present, and future time; in the latter two, the solution at each time is calculated based only on present information.

1.4.1 Numerical global optimization

Numerical methods for global optimization require the knowledge of the entire control horizon and find the global optimal control numerically. This means that the production from RES, load demands and electricity prices should be well defined and known in advance. Due to the necessity of knowing a priori the system evolution and to the required computational complexity, these methods are not easily implementable for real-time applications. Linear programming, dynamic programming and genetic algorithms belong to this category. In particular, the method most widely used is dynamic programming [50–52], which solves the optimal control backwards in time, i.e. starting from the final instant of the control horizon and proceeding backwards, ending at the initial time.

Dynamic programming (DP) was originally used in 1940 by Richard Bellman and allows the simplification of complicated control problems by means of their recursive segmentation in simpler sub-problems. The DP approach has several advantages, being able to find the global solution of both linear and non-linear problems, also in presence of control and state constraints. However, it suffers from the so-called *curse of dimensionality*, which entails the computational load exponential rise with the increase of state variables dimension. This drawback amplifies the computational complexity and limit the DP range of applications.

1.4.2 Analytical optimal control techniques

Analytical methods consider the entire control horizon as well, but use an analytical problem formulation to find the solution in closed and analytical form, consequently lowering the resolution time. However, in order to obtain a suitable description which can be completely solved by using these techniques, a significant simplification and abstraction of the problem is often required. Among these methods, the most used is the Pontryagin's minimum principle [53].

Pontryagin's minimum principle (PMP) was formulated in 1956 by the Russian mathematician Lev Semyonovich Pontryagin as a special case of Euler-Lagrange equation of calculus of variations. Being based on non-linear second-order differential equations, the dimension of the problem increases only linearly with the number of variables, which entails a low computational complexity. However, PMP provides only necessary conditions for the optimal solution, potentially leading to local optimal rather than to a global solution. Another limit of this technique is that, it generally requires a-priori knowledge of the entire optimisation horizon, which considerably limits its real-time implementation, unless combined with adaptive approaches.

1.4.3 Instantaneous optimisation

Instantaneous optimisation methods modify global optimal control problems into a sequence of local (instantaneous) problems, calculating the solution as a sequence of local minima. In this case, the cost function depends only on the present state of system variables, enabling their real-time implementation. These family of control strategies include: model predictive control (MPC), neural networks and particle swarm optimisation approaches. Additionally, a further development of PMP can be effectively used for on-line applications, by reducing the global optimisation problem into local and solving the control problem in the continuous time domain, without use of information regarding the future [53, 54].

1.4.4 Heuristic control methods

Heuristic control techniques are not based on explicit optimisation, since the energy management applies a pre-defined set of rules. Rules are typically derived by heuristic or mathematical models on the basis of engineering knowledge of the system and practical experience. These strategies are robust and computationally efficient, and hence easily implementable in real-time EMS. However, the main drawback is that the results may not be optimal, due to the lack of a formal optimisation. Rule-based control strategies and fuzzy logic methods are the most significant approaches of these control techniques.

The rule-based control strategies (RBS) are static controllers, based on rule tables of flowcharts used to define the operating point of system components. As a consequence, the EMS takes decision based only on current information and instantaneous conditions, which facilitates the respect of local constraints. In fact, the rules can be theoretically developed in order to deal with any violation of system boundaries. On the other hand, the rules are defined without referring to any standard methodology and need to be again synthesised for every new system configuration.

Chapter 2

Management Strategies for Microgrids and Virtual Power Plants

2.1 Introduction

The awareness of climate changes caused by energy production and consumption systems has driven the worldwide policies to promote a sustainable energy transition. In order to combine the needs of an energy growing demand with a sustainable development, the distributed generation (DG) based on Renewable Energy Sources (RES) was significantly supported in the last years. This, jointly with the subsides to RES provided by many countries worldwide, has caused a fast-growing demand and increasing deployment of RES conversion systems, creating the economic conditions for a de facto energy source transition. However, the natural variability of some renewable sources, such as wind and solar, has introduced a series of challenges in order to preserve the quality, reliability and controllability of the electricity grid. As result, the classic hierarchical and strictly regulated management model of the present power systems is no more suitable for handling a progressive increment of energy supply from intermittent RES. In fact, the integration of these technologies at a significant scale requires a much more flexible grid that can cope with the variability and uncertainty of supply introduced by RES systems. New operational paradigms are consequently emerging, forcing toward the adoption of active smart network architectures [7].

Microgrids (MGs) and Virtual Power Plants (VPPs) are two grid concepts that can be effectively applied in active network management of a smart grid, allowing the efficient integration of RES into the power system [10]. Both approaches are based on the clustering of demand and generation and on the adoption of a suitable network supervisory control. The aim is reducing the impact of the intermittent RES generation and improving the dispatching efficiency both technically and economically, resorting to the use of Energy Management Systems (EMSs). These avoid the infrastructure strengthening of distribution and transmission networks, consequently determining a neutral economic impact of RES exploitation on the power system. However, due to the intermittency and poor predictability of RES generation coupled with the uncertainty of load demands, new challenges arise for the design of reliable and stable MGs and VPPs [55]. For example, depending on the short-term variability of weather conditions, solar PV and wind energy generations are subject to rapid fluctuations, which result in instability of active and reactive power profiles. Additionally, the mismatch between RES production and load demand may lead to unbalance conditions and consequently impair the stability and security of the system. In order to address these problems, various strategies, including using conventional generators [56], applying demand-side management (DSM) programs [57], and enabling energy cooperation in networks of MGs and VPPs [58], have been proposed. Among these technical options, Energy Storage Systems (ESSs) are emerging as one of the most effective and practical solutions to improve the stability, reliability and security of the novel smart grid architectures. In fact, ESSs may provide the best compensation resources for a number of grid services, such as the time shifting of electricity generation and load demand, the balance of the unavoidable forecasting errors occurring in the prediction of local demand and production, and the stabilisation of the voltage and frequency for both short- and long-term applications.

Batteries can play a crucial role in this framework: they are efficient and versatile ESS technologies, some commercial chemistries being already mature for integrating RESs and providing smart grid services [59]. Alongside stationary and centralised storage systems, distributed battery configurations have gained momentum. In particular, as electric vehicles (EVs) become more popular, the possibility of using on-board batteries as load-side distributed ESS has been widely discussed in the technical literature. The related technologies are called Vehicle-to-grid (V2G) or Vehicle-to-home (V2H) and enable EVs to provide a variety of services to grid operators and customers.

The presence of ESSs both in centralised and distributed configuration can make the management of power balance and the definition of the supervisory strategy a challenging task, as they depend on a number of variables. In fact, storage devices introduce additional degrees of freedom in the control of the system that thus needs to be carefully defined. Defining the best management and operating mode for ESSs can have a significant impact on the power systems operation since storage power outputs can be controlled in order to reach several objectives (e.g. reducing the system energy cost, minimising power losses, shifting peak load, compensating RES power fluctuations and forecasting errors, and reducing the dependence from the main utility grid [59]). Moreover, the off-line development and implementation of a management strategy is fundamental in order to identify the proper rating of ESS and avoid oversizing, to verify the effectiveness and reliability of control algorithms, and enable the efficient and optimal use of all energy resources by technical and/or economic point of view.

In this Chapter, several algorithms and methodologies for the management of MGs and VPPs, integrating RES generators and battery ESSs, are proposed and analysed. In particular, the management strategies here presented are based on two different approaches that can be categorised as follows:

- rule-based strategies (RBS),
- optimal management strategy (OMS),

The proposed management strategies are implemented in four cases of study, aimed at highlighting the potentialities of integrating ESSs in different smart grid architectures. The importance of defining a proper management algorithm in order to obtain reliable and stable systems operation is underlined, as well.

2.2 V2G and ESS Integration in a VPP

The adoption of a VPP configuration is a quite new concept of managing active power networks being recently analysed in a number of studies [60–63], and additionally investigated in several European projects [64]. Originally, a VPP was defined as an aggregation of distributed generators capable to operate as a unique power plant, when properly coordinated. More recently, such an initial concept has been extended to all forms of distributed energy resources, including controllable loads and energy storage systems. Basically, a VPP gives the possibility to aggregate small grid customers (loads, generators or both) who are able to offer competitive energy blocks and auxiliary services in energy markets and to compensate for unexpected power fluctuations of wind and solar energy farms.

ESSs permit both the shifting in time of RES electricity generation and the compensation for instantaneous energy unbalance and are thus considered basic elements of VPPs. Nevertheless, the high cost of energy storage technologies represents so far the main drawback for their diffusion at the distribution grid level, requiring a careful evaluation and a correct sizing, calibrated on the real application needs. A feasible solution may be the joint management of stationary ESSs and distributed storage systems located near load centres, such as batteries of plug-in electric vehicles (PEVs). In this context, V2G technology [36, 39] could be usefully exploited in order to reduce investment cost of centralised storages. In fact, if the charging process of PEVs is appropriately managed, for instance by an aggregator [40], EV batteries can be considered either as controllable loads or distributed ESSs, helping with the regulation of the grid. Essentially, the aggregator acts as an intermediary between each EV's user and the VPP's EMS, managing EV batteries with the aim of primarily ensuring the mobility customer requirements, but offering, at the same time, network balancing services. This requires the adoption of a proper management strategy , which needs to consider driver mobility needs, V2G economy as well as regulation performance.

In this Section, a rule-based management strategy for VPPs integrating EV storage systems and stationary batteries is proposed. It aims at satisfying the VPP load demand as much as possible by relying on the sole VPP generation resources. Mathematical models of V2G and centralised ESS are firstly introduced and implemented in the VPP management algorithm. Then, an optimisation procedure, aimed at optimally designing the VPP by considering the effects of adopted management strategies and storage systems, is applied. The optimal VPP design is achieved by solving an optimisation problem, with the objective of minimising the total annual cost of the system. The proposed management approach is finally validated by means of a wide simulation study referred to an autonomous VPP characterised by a high penetration of intermittent RES. The simulation results highlight the effectiveness of the proposed strategy and the technical and economic benefits of mobile and stationary electrical storages in the energy management of a VPP. In a nutshell, the main contribution of the proposed approach is that typical issues of future active power systems, such as the optimal system planning and design, the definition of a proper management strategy and the minimisation of investment and operating costs, are analysed and addressed in a synergistic way in order to obtain a reliable, efficient and economic autonomous VPP.

2.2.1 Mathematical Modelling

The effectiveness of the proposed management algorithm considerably depends on reliable modelling of all VPP components. The mathematical models specifically developed for the battery and V2G systems as well as for the VPP generation units (GUs) are described in the following sub-sections. In particular, specific aspects related to the impact of the hardware constraints on the EMS are highlighted and modelled.

2.2.1.1 Battery Model

In recent years, the technological progress in the field of electrochemical storage is especially focused on lithium based batteries, which are considered the best candidate for automotive and mobile applications thanks to their low weight, high energy density, efficiency and cycle life. These features make Li-Ion batteries attractive also for stationary installation, especially in areas characterized by space constraints. In particular, the Lithium Iron Phosphate (LFP) is currently considered one of the most versatile and adaptable battery technologies, especially in the vehicular field [29,65]. For these reasons, LFP-based batteries have been assumed as basic technology of both storage packs of EVs and centralised battery (BESS).

In order to consider the effect of dynamic and non-linear behaviour of LFP batteries, a dynamic energy model is developed. This is based on the analysis of experimental discharge and charge test results carried out on a 2.3 Ah/13.2 V LFP battery. An example of data-based voltage and current curves are reported in Fig. 2.1. Referring to the experimental results, a numeric curve-fitting is performed in order to find polynomial equations that give the best matching with charging and discharging test outcomes. In particular, a ninth-order polynomial is used in order to evaluate the discharge terminal voltage (V) as a non-linear function of the battery energy (E), as shown in (2.1).

$$V = a_0 \cdot E^0 + a_1 \cdot E^1 + a_2 \cdot E^2 + a_3 \cdot E^3 + ... + a_9 \cdot E^9. \tag{2.1}$$

Moreover, it is worth noting that the LFP battery charge process is composed of two phases: the first at constant current (CC) and the second at constant voltage

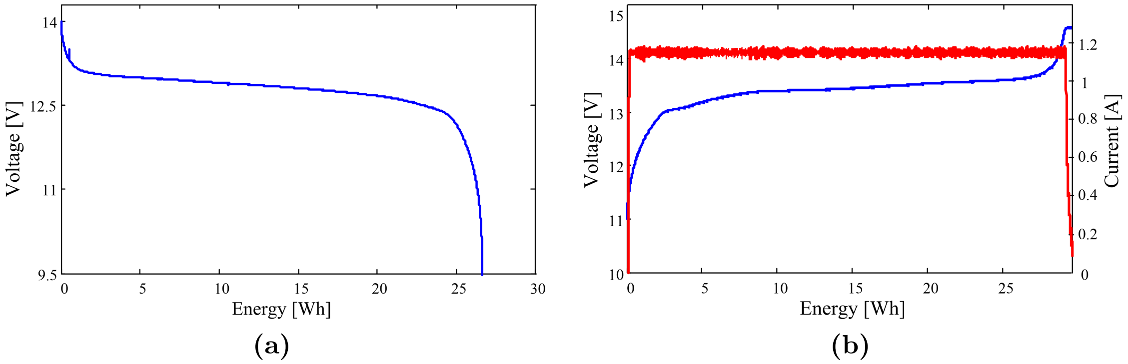

Figure 2.1: *LFP battery voltage (blue) and current (red) experimental curves. (a) 0.25 C-rate discharge test. (b) 0.5 C-rate charging test.*

(CV). While during the CC stage the terminal voltage is computed as a non linear function of the energy, in the CV phase the voltage remains constant at its maximum value (V_{max}) and the current decreases. In this case, the battery current (I) can be determined by means of a quadratic function of E:

$$I = b_0 \cdot E^0 + b_1 \cdot E^1 + b_2 \cdot E^2. \tag{2.2}$$

Clearly, (2.1) and (2.2) allow the calculation of V and I as function of the battery stored energy E and, as a consequence, of its State of Charge (SOC). In order to determine the battery power and the stored/delivered energy during a specific time interval Δt, a discrete time energy algorithm is thus considered. The battery energy in a generic time step t and, consequently, its SOC can be accordingly obtained by applying (2.3) and (2.4).

$$E(t) = E(t-1) + P(t-1)\mathit{\Delta} t, \tag{2.3}$$

$$SOC(t) = SOC(t-1) + \frac{1}{C_b} \cdot I(t-1)\mathit{\Delta} t, \tag{2.4}$$

where $E(t)$ and $SOC(t)$ are respectively the updated battery energy and state-of-charge at the generic time-step t, being C_b the nominal battery capacity and representing Δt the duration time of each interval. Furthermore, P indicates the battery power, calculated by means of (2.5) or (2.6) for discharge or charge mode, respectively.

$$P(t) = V(t) \cdot I(t) \tag{2.5}$$

$$P(t) = \begin{cases} V(t) \cdot I(t) & \text{CC Phase} \\ V_{max} \cdot I(t) & \text{CV Phase} \end{cases} \tag{2.6}$$

Still referring to (2.5) and (2.6), it is worth clarifying that $I(t)$ and consequently $P(t)$ can be either positive or negative depending on battery operation as load (charging) or generation unit (discharging). Given the value of $E(t-1)$, the corresponding voltage $V(t-1)$ can be obtained from (2.1). By setting the discharge current rate or applying (2.2) for the charge process, the value of the power $P(t-1)$ can be accordingly determined . The updated battery energy is then evaluated by (2.3) and subsequently used to calculate the next step voltage. In order to obtain a reliable and representative emulator of V2G and battery systems, the proposed battery model needs to include some operative constraints. These are defined as in (2.7) through (2.10), where j can alternatively take the meaning of BESS or EV. Particularly, the constraint (2.7) imposes upper and lower limits on the battery SOC, introduced in order to preserve the battery life and avoid battery damage due to over-charging and under-discharging phenomena [41–44]. In addition, as far as the battery pack of an EV is concerned, SOC^{min} restricts the capacity usable for V2G management purpose in order to guarantee in all cases an energy reserve for driving a preset kilometer range. The battery current constraints are outlined in (2.8), where the maximum tolerable charge/discharge current rates are considered. Batteries power is constrained by (2.9) and the power limits are specified in (2.10). The latter defines the constraints on the battery power capability at each time-step, by considering three elements [39]: the maximum battery current rates, the maximum rated capacity of the bidirectional AC/DC converter (P_C) and the maximum power flow allowed from the connection line (P_L).

$$SOC_j^{min} \leq SOC_j(t) \leq SOC_j^{max} \tag{2.7}$$

$$I_j^{min} \leq I_j(t) \leq I_j^{max} \tag{2.8}$$

$$P_j^{min} \leq P_j(t) \leq P_j^{max} \tag{2.9}$$

where:

$$\begin{cases} P_j^{min}(t) = & \mathbf{max}(I_j^{min} \cdot V_j(t), -P_C, -P_L) \\ P_j^{max}(t) = & \mathbf{min}(I_j^{max} \cdot V_j(t), P_C, P_L) \end{cases} \tag{2.10}$$

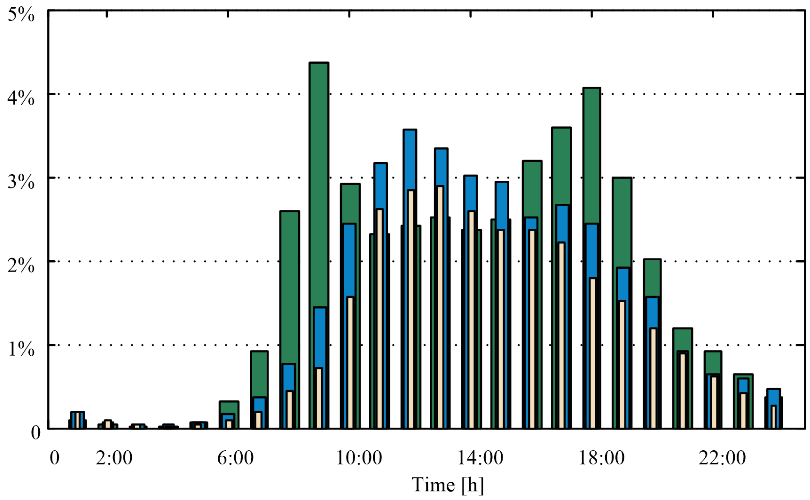

Figure 2.2: *Statistical time distribution of private cars en-route referred to a typical week: work-days (green), Saturday (blue) and Sunday (yellow).*

2.2.1.2 V2G Model

The V2G system is modelled by the aggregation of plugged EV batteries. V2G storage and power flows from/to the grid are managed by the aggregator (namely the V2G controller). It can estimate at each time-step the global available capacity, according to the number of EVs connected to the grid, EV battery SOC, current and power limits as well as driver requirements. This information allows the correct evaluation of energy services that can be effectively provided by the V2G system at each sampling interval.

The application of the V2G concept requires a detailed knowledge of driving profiles, which can be obtained referring to daily mobility habits. In particular, a proper mobility model is developed starting from the analysis of statistical time distributions of vehicles on the road, as deduced from [66] and reported in Fig. 2.2. At each time-step, the whole EVs fleet is accordingly partitioned into two groups: the first composed of vehicles on the road (r) and the second represented by parked EVs (q). Within the latter a further sub-fleet is defined by the set of parked and plugged EVs (s), as follows:

$$s(t) = q(t) \cdot \rho = [1 - r(t)] \cdot \rho \tag{2.11}$$

In (2.11), ρ identifies the plug-in ratio parameter, which represents the percentage of parked EVs that are actually plugged. Such a parameter takes into account the availability of charging infrastructure and the EV owner's willingness to physically connect the vehicle to the grid and provide V2G services. Assuming the EV fleet constituted of n_{EV} vehicles, its rated capacity and power are calculated by (2.12) and (2.13) respectively.

$$E_n = E_b \cdot n_{EV} \tag{2.12}$$

$$P_n = P_b \cdot n_{EV} \tag{2.13}$$

being E_b and P_b the EV battery rated capacity and power respectively. Therefore, based on the proposed battery and mobility models and applying (2.11) through (2.13), the V2G controller can estimate at each time-step the global available V2G capacity (E_s) from (2.14).

$$E_s(t) = \left\{ \begin{array}{c} \left[E_s(t-1) \cdot \left(1 - \dfrac{r(t)}{s(t-1)}\right)\right] + \\ + \left[E_s(t-2) \cdot \left(\dfrac{r(t-1)}{s(t-2)}\right)\right] + \\ -\left(C_{EV} \cdot r(t-1) \cdot n_{EV} \cdot \rho\right) \end{array} \right\} \tag{2.14}$$

Eq. (2.14) consists of three terms. The first evaluates the energy at the time t based on the stored energy at the previous step $E_s(t-1)$. From this quantity the capacity subtracted by EVs which start their trips at the time t has been subtracted. The second term represents a further additive component which takes into account the energy added by EVs arrived to their destinations at the time t, which were en-route in the previous step $(t-1)$ and parked and plugged at the time $(t-2)$. The third term finally deducts the energy consumption of EVs (C_{EV}) on the road at the time $(t-1)$. At each t-sampling interval, the V2G controller needs to compute also the boundaries of the available V2G energy capacity, as defined in (2.15)-(2.16).

$$E_s^{min} \le E_s(t) \le E_s^{max} \tag{2.15}$$

where:

$$\begin{cases} E_s^{max}(t) = \left(SOC_{EV}^{max} - SOC_{EV}^{min}\right) \cdot E_n \cdot s(t) \\ E_s^{min}(t) = SOC_{EV}^{min} \cdot E_n \cdot s(t) \end{cases} \tag{2.16}$$

Still referring to (2.15) and (2.16), the energy charged in the plugged EVs battery can not exceed $E_s^{max}(t)$, which represents the maximum aggregated battery available at the considered time interval; whereas the energy supplied to the grid must be lower limited by the energy $E_s^{min}(t)$, necessary for guaranteeing emergency leavings. Finally, the V2G controller complies with the following constraint, applied for the definition of the actual power outputs of the aggregated V2G battery:

$$P_s^{min} \leq P_s(t) \leq P_s^{max} \tag{2.17}$$

In (2.17), the maximum charge/discharge power capability of the V2G system are calculated from the current limits of plugged EVs and rating power of the line connection, in accordance with (2.10). It is worth noting that when the V2G system is considered unavailable, P_s is equal to zero and thus there is no energy exchange between plugged EVs and the VPP.

2.2.1.3 Non-renewable Generation Unit Model

The VPP is tasked with aggregating different distributed generators both renewable and fossil. In particular, since VPPs are generally designed to supply electrical and thermal loads, a combined heat and power (CHP) is generally required. In this case, the CHP needs to be modelled in order to ensure a stable and secure management of energy supplying within the VPP. To this end, some hypnotises are put forward.

The CHP is primarily supposed to be heat driven, being a gas turbine its prime mover. Additionally, an external boiler is integrated within the CHP system at the aim of increasing the VPP flexibility and reliability. The CHP plant is hence modelled using rated thermal and electrical power, minimum loading capacity, heat to power ratio and efficiency. In particular, as can be observed in Fig. 2.3, the gas turbine efficiency (η_G) depends on the load power (P_G), and it is consequently modelled by a second order exponential function, as follows:

$$\eta_G = \alpha \cdot e^{\beta P_G} + \gamma \cdot e^{\varepsilon P_G}. \tag{2.18}$$

By implementing such a model, the EMS is able to evaluate the CHP electrical efficiency as the electrical power changes. Consequently, it is possible to estimate the variations in fuel consumption due to partial load operating conditions. The modulation of the CHP electrical power is limited by the constraints of its maximum rated power (P_G^{max}) and technical minimum (P_G^{min}).

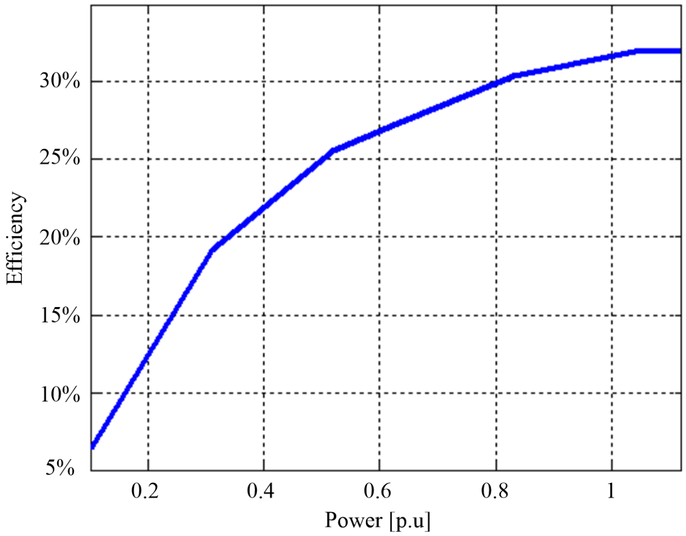

Figure 2.3: *Efficiency curve of a medium-size gas turbine as a function of load power (p.u.).*

2.2.1.4 RES and Load Models

The power productions of wind (P_W) and PV (P_{PV}) generators as well as VPP loads (P_L) are modelled from real input data obtained from two German network operators. The measurement data were then normalised to the measured peak load, obtaining synthetic hourly profiles. These are depicted in Fig. 2.4 for an average week.

2.2.2 Energy Management Operating Strategy

The main goal of the EMS is satisfying the VPP load requirements as much as possible, by the exploitation of the VPP's GUs and storage systems. In order to achieve this primary purpose, a rule-based management strategy, derived from load following criteria and energy balance equations, is proposed. The flow chart diagram reported in Fig. 2.5 illustrates the main steps in the synthesis of the EMS strategy. Basically, the management algorithm starts from the hourly evaluation of load demand and generation units production. The status of BESS and EVs operating in V2G mode together with maximum and minimum charge and discharge capabilities are estimated as well, by implementing the battery and V2G models described in (2.1) through (2.17). The expected load and power sources productions are then used to compute the VPP electric balance and detect the presence of an energy imbalance

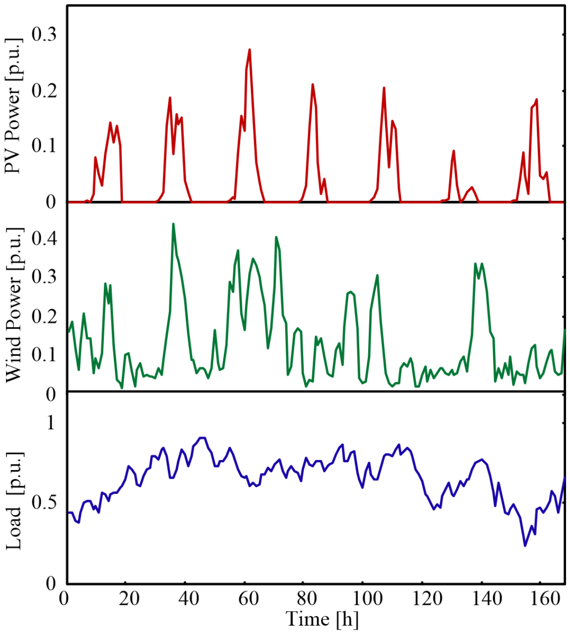

Figure 2.4: *Weekly power production of PV (red) and wind (green) generators and load power demand (blue).*

condition in accordance with (2.19).

$$P_T(t) = P_L(t) - P_G(t) - P_W(t) - P_{PV}(t). \tag{2.19}$$

The identification of an electricity surplus or deficit event defines the specific control action with the aim of completely satisfying the electric load requirements. The sequence of management actions enables ESSs to priority support the VPP when imbalance events occur, within the limits of their capacities and availability. In fact, the introduction of energy storage systems in the VPP could be essentially exploited to relax several energy management constraints, reducing modulation actions on the VPP's GUs and controllable loads, as clarified in the following. Moreover, although the required balance services can be carried out by V2G and BESS, the proposed strategy prioritizes the exploitation of V2G resources in order to reduce the sizing needs for the centralised storage. The actual discharge/charge power of the V2G system is defined as shown in Fig. 2.6a. Similarly, the power set-point for the BESS system is determined on the basis of the decision process of Fig. 2.6b. If ESSs are not able to cover the whole imbalance, GUs and controllable loads are dispatched accordingly, following the set-point definition procedure of Fig. 2.6c. Assuming an overproduction event, the EMS could act a reduction of the local fossil fuel energy

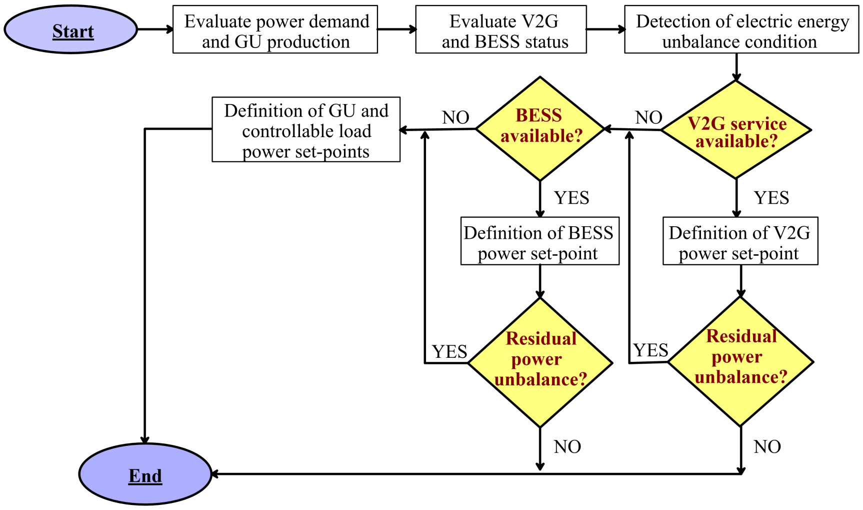

Figure 2.5: *Flow chart of the EMS algorithm*

production, followed by modulation of RES generators, if the energy balance condition is still not satisfied. It is worth observing that, since the CHP is heat driven, when a power reduction is required, the CHP controller activates the external boiler in order to cover the whole heat demand. In case of energy underproduction, the EMS modulates fossil fuel plants by increasing their energy production and then, if the deficit condition persists, the controllable loads are regulated by resorting to demand response (DR) agreements.

The EMS management strategy allows the recharge of EVs only when an overproduction occurs, preventing VPP overload which could be caused by unmanaged charging. In spite of this, EV mobility requirements are in any case preserved thanks to the introduction of proper constraints on SOC of V2G batteries, as in (2.7).

The applied EMS operating control is implemented assuming a decision making interval equal to one hour. The choice of an hourly operating step is fundamentally related to the sampling interval of the majority of the data-set used for modelling electrical energy production and demand.

2.2.3 The VPP optimal design problem

The problem of optimally sizing the power capacity of wind and PV power plants (P_W^b and P_{PV}^b, respectively) and the EVs fleet dimension (n_{EV}) for an autonomous VPP is modelled by (2.20) through (2.26). The proposed economic optimisation algorithm determines the minimum VPP annual total cost (TC) for the defined

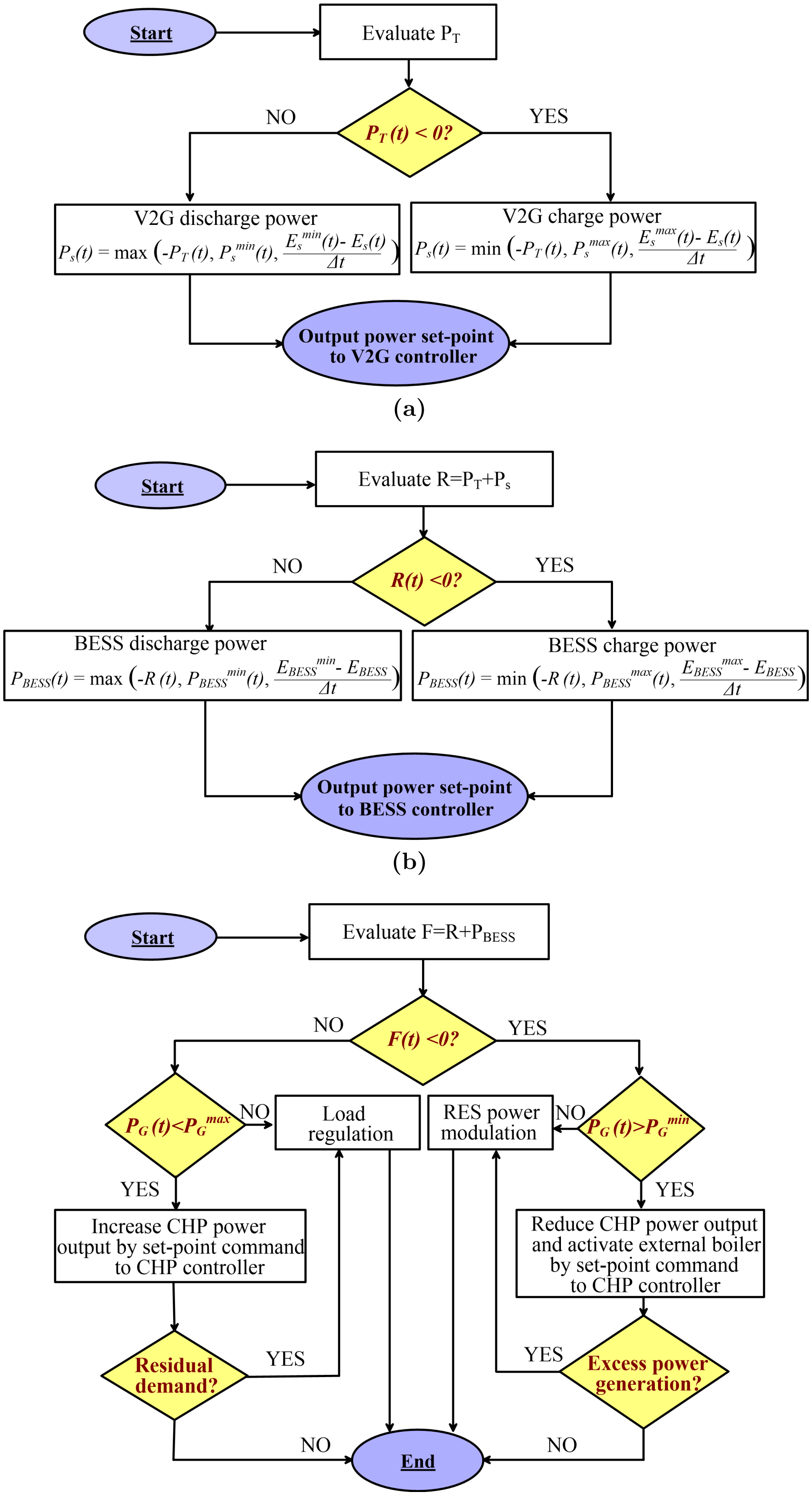

(a)

(b)

(c)

Figure 2.6: *EMS operations: definition process of VPP resource set-points. (a) V2G. (b) BESS. (c) GU and controllable loads.*

ensemble of decision variables, using the objective function reported in (2.20). The TC is updated at each iteration by running a full simulation of the VPP operations throughout a whole year with an hourly resolution. The optimal problem is hence formulated as follows:

$$\textbf{min}\,\mathrm{TC} = \textbf{min} \sum_{t=1}^{8760} \sum_{i,j} G_i(t) + B_j(t) + M(t) + D(t) \tag{2.20}$$

subject to (2.21)-(2.22) $\forall t \in [1, 8760]$,

$$\begin{cases} P_L(t) + P_s(t) + P_{BESS}(t) - P_G(t) - P_W(t) - P_{PV}(t) = 0 & (2.21) \\ Q_L(t) - Q_G(t) = 0 & (2.22) \end{cases}$$

and constrained by (2.23) through (2.26):

$$\begin{cases} \displaystyle\sum_{t=1}^{8760} P_W(t) + P_{PV}(t) = 0.2 \cdot \sum_{t=1}^{8760} P_L(t) & (2.23) \\ P_{PV}^{b,min} \leq P_{PV}^{b} \leq P_{PV}^{b,max} & (2.24) \\ P_{W}^{b,min} \leq P_{W}^{b} \leq P_{W}^{b,max} & (2.25) \\ n_{EV} \geq n_{EV}^{min}, & (2.26) \end{cases}$$

where G_i is the generation cost of the power plant i, including CHP, PV and wind resources; B_j represents the storage cost for BESS and EVs, while M symbolises the cost associated to RES power production modulation and D typifies the load deficit cost. Moreover, Q_G defines the thermal power output of the CHP plant, being Q_L the thermal power load demand.

As far as the problem constraints are concerned, (2.21) and (2.22) represent respectively the hourly electrical and thermal VPP energy balance conditions, whereas (2.23) defines the VPP design constraint connected to RES European Strategic energy plan goals. This particularly implies RES annual energy productions supplying the 20% of the yearly demand of the district loads. Local RES and electric mobility planning constraints are applied by (2.23)-(2.26), which could take into account both the renewable plants capacity limits and local environmental planning restrictions.

The calculation of the TC in the objective function is based on four terms. Firstly, the energy generation cost G_i is computed by means of the Levelised Unit Energy Cost (LUEC) approach [67, 68]. It consists of both annualised investment and oper-

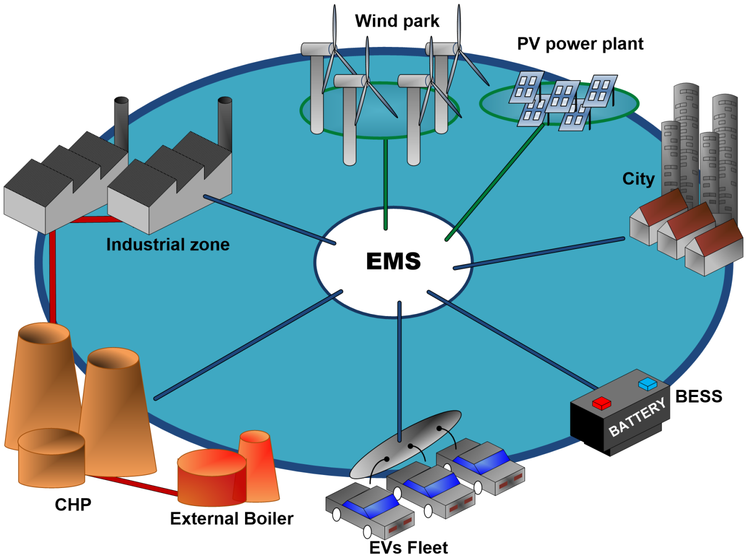

Figure 2.7: *Virtual Power Plant structure: case of study.*

ating costs of each generator, the latter including annual fuel and maintenance costs of RES plants, CHP and external boiler. In particular, (2.18) is properly employed for the correct evaluation of the CHP fuel cost. The V2G cost (included in the B_j term) considers subsidiaries for the purchase of EVs and the cost of meter and communication infrastructures, levelised during the EV life-time. Additionally, B_j includes the annualised investment costs of the centralised storage system. Referring to M, the cost associated to wind and PV production curtailment is estimated conservatively by adopting the external cost concept [69]. Finally, the cost of load shedding operations is economically evaluated introducing the cost variable denoted by the Value of Lost Load (VoLL), which represents an average cost caused by the disconnection of VPP loads in periods of energy deficit. This parameter depends on several factors, such as the type of customers and activities as well as duration, frequency and time of outages [70–72]. More detailed information on the economic assumptions used for calculating the VPP total cost can be additionally found in [73].

2.2.4 Simulations

In order to evaluate the effectiveness of the proposed EMS and VPP structure, a simulation study is carried out by means of the Matlab Software Package. The reference energy system is the benchmark industrial district illustrated in Fig. 2.7. The VPP is basically composed of three energy suppliers: a 20 MW CHP plant, a wind farm and a PV power plant. The proposed VPP supplies both electrical and thermal energy to an industrial zone and a city with 20,000 habitants. The maximum residential load is 10 MW, while the industrial electrical and thermal peak loads are assumed both equal to 17 MW. The car fleet of the overall VPP consists of 11,000 vehicles, corresponding to about 550 passenger cars per 1,000 inhabitants [74]. A variable number of automobiles is then assumed to be replaced by pure plug-in electric vehicles, characterised by C_{EV} equal to 0.145 kWh/km in accordance with the average energy consumption of commercial EVs. Moreover, a 23 kWh battery capacity is considered. However, since the SOC range of the battery usable for V2G services is limited by (2.7), the SOC is effectively bounded to a range of $45\% - 95\%$. This allows the EV to have a supplemental kilometre range of 40 km, which accounts for unexpected and additional journeys. In addition, EVs are assumed to be plugged through power lines with a maximum rated power and current-carrying capacity of 3.3 kW and 16 A, respectively. Regarding the plug-in ratio parameter ρ, the percentage of parked EVs that are actually plugged is set constant to 0.8 for each simulation time-interval. Based on this value it is possible to determine the corresponding time distributions of vehicles providing V2G services, as shown in Fig. 2.8.

The rule-based management algorithm integrated in the optimal problem is recursively applied in order to determine the optimal size of VPP units by means of (2.20) through (2.26). Therefore, planning constraints (2.24), (2.25) and (2.26) need to be specified for the presented case of study. Particularly, a minimum EVs number equal to 100 is set, whereas PV rated power P_{PV}^{b} is considered varying between 5 MW and 10 MW. Finally, a variation range of 10 MW-22 MW is hypothesised for the wind park.

In the following, three scenarios are analysed in order to compare the effectiveness of different storage solutions for the autonomous VPP. The first is the reference scenario, where no ESSs is deployed; the second evaluates VPP performance and resources optimal rating considering the V2G system as distributed ESS; finally the integration between V2G and stationary BESS is analysed in the third scenario.

2.2.4.1 Reference Scenario

In this scenario, the application of the optimisation algorithm allows to define the optimal sizes of PV and wind generators that minimise the VPP annual total cost, satisfying the design constraints. Referring to the VPP configuration of the refer-

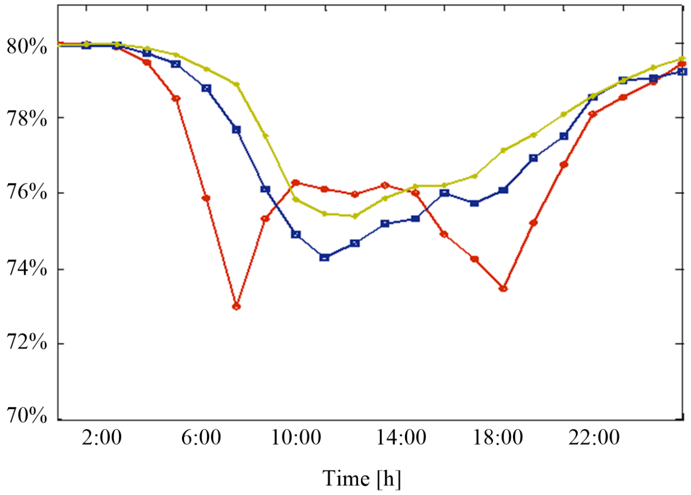

Figure 2.8: *Statistical time distribution of EVs available for V2G services referred to a typical week: work-days (red), Saturday (blue) and Sunday (yellow)).*

ence case, Fig. 2.9a shows the hourly time evolution of VPP electrical consumption, potential production without EMS actions, and the results of the management strategy for a general three-days period. It can be observed that the VPP balance is not globally achieved and the EMS has to resort to load shedding, especially in the peak load periods. A summary of the reference scenario results is reported in Table 2.1.

2.2.4.2 Second Scenario

In the second scenario, a Vehicle-to-Grid algorithm is integrated into the EMS procedure in order to improve the VPP reliability by managing the charging/discharging cycles of PEVs batteries. The optimisation problem results can be observed in Table 2.1, whereas the corresponding hourly operation for a three-days period is depicted in Fig. 2.9b. It is worth noting that the introduction of an EVs fleet operating in V2G mode reduces the total cost by 2.3% and cuts load deficit cost by 64% respect to the reference scenario results. However, it can be also observed that some conditions of imbalance still occur and these are mainly distributed during peak load hours.The annual frequency distribution of power deficit is depicted in Fig. 2.10 and shows the inability of the VPP to supply the totality of load demand, resorting to load curtailment operations for nearly 500 hours per year. The minimum number of EVs necessary to reduce to zero the energy not supplied and reach the VPP energy autonomy is consequently calculated, resulting in a fleet of 1895 EVs (i.e. 17.2% of the overall VPP cars) Nevertheless, since the rise in storage costs is higher than the

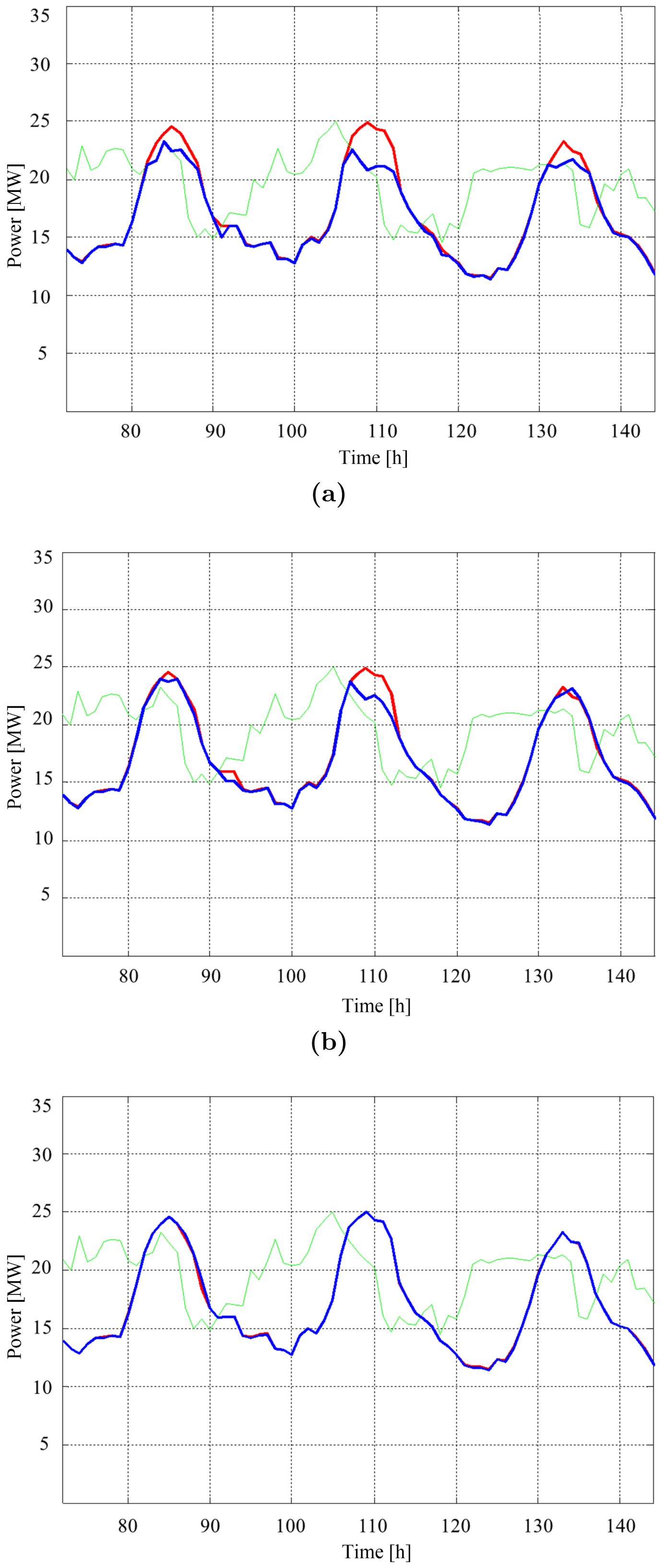

(a)

(b)

(c)

Figure 2.9: *Time evolution of VPP electrical consumption (red), potential production without EMS actions (green), and the results of the management strategy (blue). (a) Reference scenario. (b) First scenario. (c) Second scenario.*

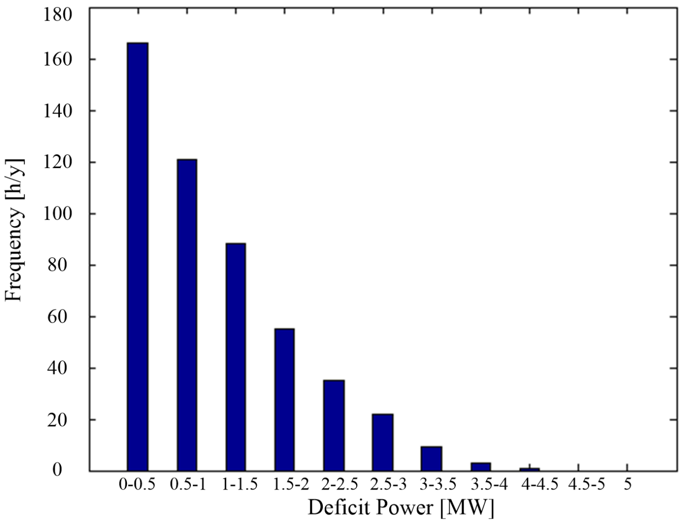

Figure 2.10: *Annual frequency distribution of power outages for the second scenario optimal configuration.*

deficit cost reduction, this solution results in increasing TC by 7.9% respect to the reference scenario.

2.2.4.3 Third Scenario

In this scenario the centralised battery system supports the VPP during peak hours in addition to the distributed V2G storage. The aim is finding the optimal dimension of the EVs fleet which permits VPP islanding operations without resorting to load shedding actions. To this end, the optimisation problem is formulated differently from (2.20), adopting as objective function the minimisation of the load deficit cost and using as decision variable the sole EVs number. Consequently, in this case, the same optimal RES power plant dimension of the second scenario is assumed. Moreover, the rated power and capacity of the stationary BESS are set equal to 0.9 MW and 6 MWh respectively. Such a sizing has been obtained from the analysis of the annual distribution and value of power outages detected in the second scenario as reported in Fig. 2.10. The optimal solution results in an minimum EVs number equal to 1180, which represents the 8.4% of the whole VPP car fleet. As can be observed in Fig. 2.9c and in Table 2.1, the proposed integrated storage system is effectively managed in order to obtain a reliable autonomous VPP, reaching the full hour energy balance with no power shortfalls. Nevertheless, the economic results of Table 2.1 also show a total cost rise of 1.8% respect to the reference scenario and

Table 2.1: *Scenarios relevant results.*

	Unit	**1^{st} Scenario**	**2^{nd} Scenario**	**3^{rd} Scenario**
P^b_{PV}	MW	5	5	5
P^b_W	MW	10	16	16
n_{EV}		-	506	1180
Generation Cost	M€/y	10.89	11.44	11.35
EV Cost	M€/y	-	0.66	1.54
BESS Cost	M€/y	-	-	0.24
Deficit Cost	M€/y	1.45	0.52	0
Total Cost	M€/y	12.93	12.63	13.16

4.2% in comparison to the second. Such an outcome is mainly due to the growth in the EVs annual costs. In fact, the EVs number is computed in order to minimise the annual VoLL cost and not to optimise the VPP total cost, as in the previous scenarios. In spite of this, it is interesting to point out that the complete satisfaction of the VPP electricity demand can be achieved at a lower total cost respect to the sole V2G implementation suggested in the second scenario, where 1895 EVs are necessary to reach the same result.

2.2.4.4 Sensitivity analysis

The emulation of the V2G storage presented in the previous sections is implemented in the EMS algorithm considering a plug-in ratio ρ equal to 80%. At the present time, this percentage would be very hardly achievable due to the low diffusion of infrastructures suitable for the implementation of the V2G technology. For these reasons, the evaluation of effects induced by lower plug-in ratios is fundamental in order to validate the robustness of the obtained results. Therefore, the sensitivity of total cost to ρ and n_{EV} variables is analysed. Particularly for the third scenario, the results shown in Fig. 2.11 reveal that the integration of V2G with the stationary BESS makes the VPP robust to weaknesses of V2G infrastructure. This statement can be deduced by using the total cost as a management quality index that annually quantifies the energy balance into the VPP. In fact, assuming constant the number of EVs as well as battery size, and variable the plug-in ratio, the total cost variation can be only associated to the rise of the load curtailment actions, which in turn

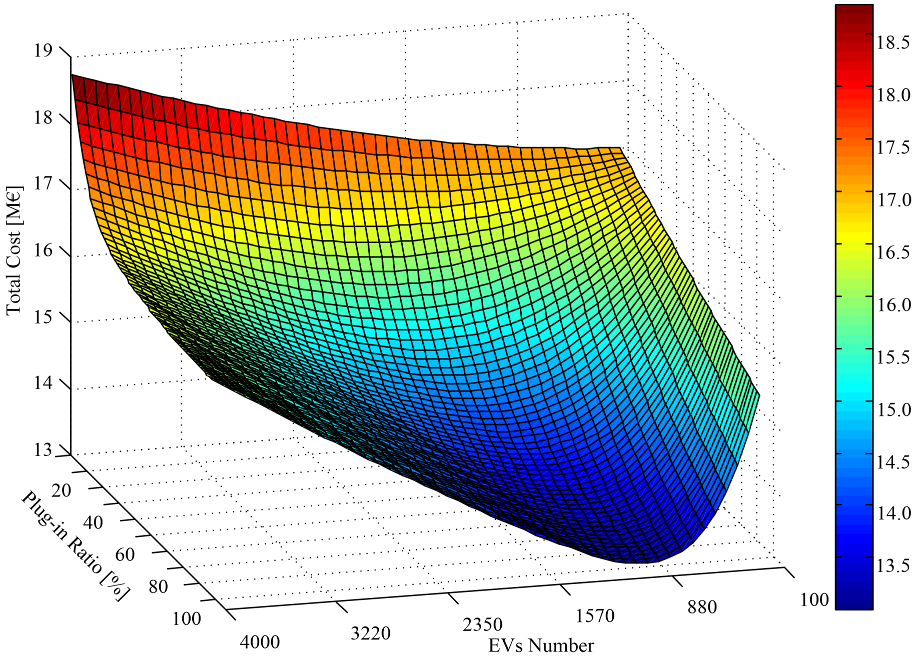

Figure 2.11: *Evolution of total cost function versus EVs number and plug-in ratio for the third scenario.*

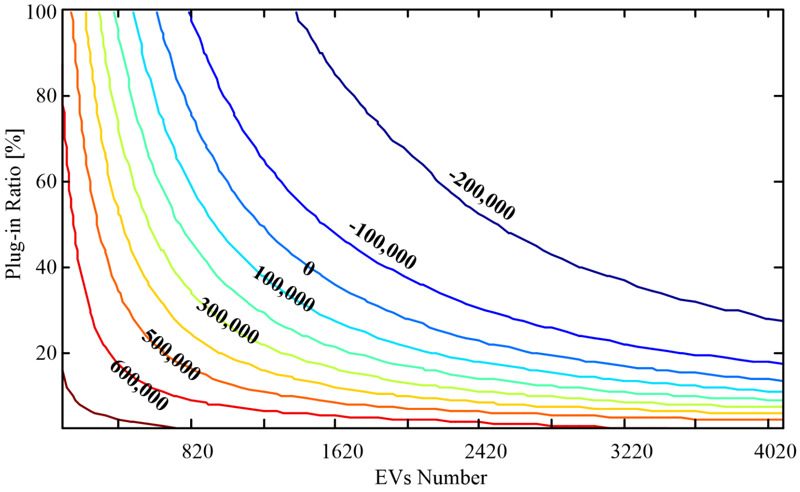

Figure 2.12: *Differential annual cost versus EVs number and plug-in ratio.*

are mainly related to the reduction of ρ. For example, considering fixed the VPP configuration reported in Table 2.1 for the third scenario, the assumption of ρ equal to 10% results in a 3.4% increase in TC from the value obtained with a plug-in ratio of 80%. Therefore, considering the limited impact on the TC, such an outcome points out the low sensitivity of the integrated ESS configuration to ρ variations.

From a summary analysis of the second scenario, it's clear that ρ has a more significant impact on total cost and VPP energy management, since in this case the V2G system is the only ESS of the VPP. In order to better quantify the consequences of the integration between stationary BESS and V2G in an autonomous VPP, a comparison between the two storage-based scenarios has been carried out, evaluating the mathematical difference (Δ) between the total cost functions of the second and third scenario (referred to same conditions of ρ and n_{EV}). Fig. 2.12 graphically summarizes the obtained outcomes, showing the dependence of the differential cost Δ on ρ and n_{EV}. Each trace represents a mathematical set of points in the (n_{EV}, ρ) plane characterised by a constant Δ, where a positive Δ indicates total cost of the second scenario greater than that of the third. Referring to the trace for $\Delta = 0$ as the reference curve, it can be observed that the Δ evolution is characterised by a different gradient in the two side of the plane (n_{EV}, ρ) which assumes relevant values when a combination of low (n_{EV}, ρ) occurs. Particularly, a plug-in ratio lower than 15% results in total cost of the third scenario less than that of the second for every dimension of the EVs fleet. This shows the advantage of the $V2G + BESS$ configuration in term of robustness, making it more suitable to support the VPP especially during the start-up period of the V2G technology, when low values of both ρ and n_{EV} are highly probable. From these considerations, its evident that the approach of minimising the VPP total cost does not provide always the best solution. In fact, it gives only an economic evaluation of the VPP configurations and does not take into the account the uncertainty of some system parameters, such as ρ and n_{EV}, which can significantly influence the VPP performance. Since this critical remark does not emerge by the sole comparison of optimisation results reported in Table 2.1, the proposed sensitivity analysis appears of utmost importance in order to correctly estimate the feasibility of the VPP in every n_{EV}-ρ condition. In conclusion, simulation results have highlighted the economic and energy benefits for an autonomous VPP featuring an integrated ESS. In particular, the synergy between V2G and BESS allows the achievement of more robust VPP configuration, permitting to make the results of the proposed optimisation procedure less dependent on the uncertainty connected to V2G infrastructures.

2.3 ESS Integration in an Industrial Microgrid

The previous section has highlighted the viability of centralised battery storage in active power networks, especially when integrated with other ESS technologies. In fact, although energy- and power-intensive services can be both provided by several electrochemical storage technologies, the use of a sole stationary battery system for smart grid services will likely result in storage oversizing and related unnecessary investment costs. Referring to an islanded MG, its reliability can be ensured by installing adequate generation resources and ESS, the latter operating as both energy back-up and power compensating unit. However, the strict specifications in terms of capacity and power capability imposed in this case may not be satisfied by a single storage technology without incurring in oversize and over-costs. The concept of Hybrid Energy Storage System (HESS) is accordingly introduced, indicating a system composed of two complementary ESS technologies. Generally, the most diffused HESS configuration is based on a BESS coupled with high power ESSs, such as flywheels or supercapacitors. Nevertheless, different combinations could be implemented, for instance exploiting the synergistic integration of thermal and electrical storage systems.

A novel approach is represented by the deployment of thermal energy storage (TES) associated with small-scale Concentrating Solar Power (CSP) plants as supporting units of micro smart grids. In fact, the use of thermal storage enables the dispatchability of CSP plants, making this solar technology suitable for shifting energy, reducing feed-in-power variability, smoothing electricity production as well as providing base load generation and scheduled power-to-grid profiles [75–77]. Therefore, CSP plants with TES could be able to provide several energy services to the MG, representing an ideal complement to battery systems. In fact, BESS can be used for balancing the forecasting errors or compensating the fast power variations of loads and RES generators. As a result, a proper sizing of the BESS could be obtained considering its exploitation mainly for power applications.

In this Section, a rule-based management strategy for an industrial MG integrating electrochemical and thermal storage systems is proposed. It aims at fully supplying the MG loads by 100% RES generation and ensuring the accomplishment of scheduled power-to-grid profiles. The microgrid will be developed from an existing municipal waste treatment platform, which includes gasometers and CHP generators as well as several energy-consuming processes. Therefore, a detailed analysis of its

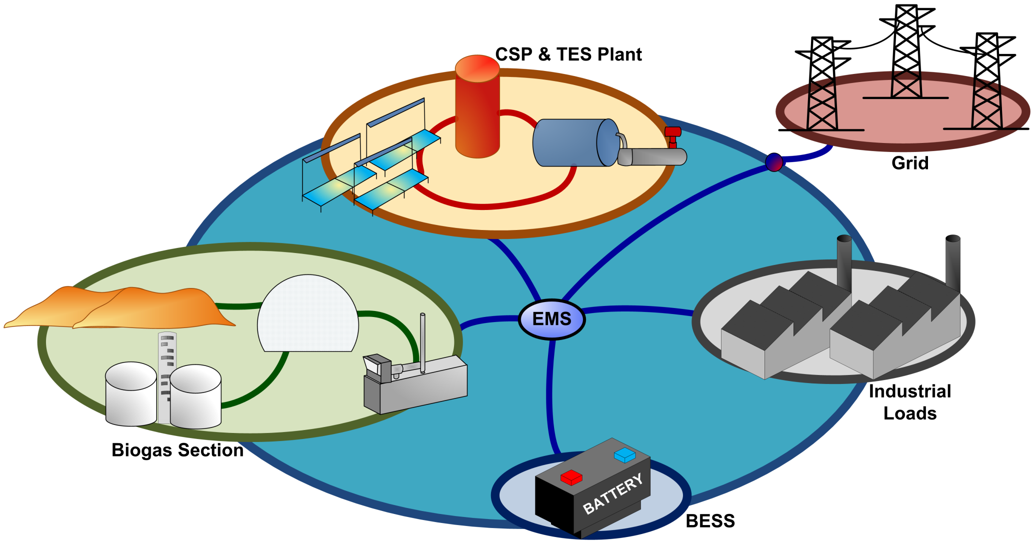

Figure 2.13: *Schematic representation of the industrial microgrid.*

electrical loads and a proper evaluation of the whole system energy balance is firstly presented. Then, the necessity of effectively managing the available resources of the waste treatment plant and determining charge/discharge cycles of storage systems is addressed by the proposed management approach. To this end, the microgrid power dispatching has been determined by controlling all the RES generators and storage systems in a synergic way, considering also the different dynamics of demand variations during the day and the week. Finally, the simulation results demonstrate the feasibility of a small scale CSP plant combined with thermal and electrochemical storage systems in order to enhance the reliability and autonomy of the industrial microgrid, highlighting the effectiveness of the proposed management algorithm, as well.

2.3.1 Microgrid Energy Balance and Modelling

The development of the reference industrial MG (schematically represented in Fig. 2.13) is planned in order to integrate a CSP-TES plant and a BESS in an existing waste treatment platform within the Concentrating Solar Power Project [78]. The project is co-funded by the European Union in the framework of the ERDF 2007-2013 and will be realised in the industrial district of Villacidro, in the south of Sardinia (Italy). There, a waste treatment plant is already in place and includes a landfill, an anaerobic digestion plant, a gasometers and a CHP system based on a couple of internal combustion engines. The biogas produced by the anaerobic digestion process feeds one of the CHP units, and then the electricity production is used to power the waste treatment plant. However, such a renewable generation is not sufficient to cover all the electric load demand, requiring the purchase of energy from the local distribution utility in order to fully supply the residual load. Since energy interruptions in the platform operations would result in technical problems and economic losses, the MG needs to effectively rely on its own generators and storage in order to guarantee secure and optimal energy supply to continuous processes, also in presence of power system failure. The installation of the CSP plant and BESS has hence the primary purpose of improving the security of load supply, fully balancing the residual load by the sole MG RES generators and storage systems. Consequently, the MG power balance can be expressed as:

$$R(t) + S(t) - P_J(t) - P_{CSP}(t) = G(t) \tag{2.27}$$

where P_G represents the power production of the CHP generator supplied by the biogas from the landfill, P_{CSP} being the power output of the concentrating solar power plant, including also the TES system. Moreover, S is the power supplied or absorbed by the battery storage, while G denotes the power exchanged by the MG with the distribution grid. Finally, R indicates the MG residual load, further defined as in (2.28).

$$R(t) = L(t) - P^a_{CHP}(t) \tag{2.28}$$

being L the total load of the waste treatment plant and P^a_{CHP} the power supplied by the CHP unit associated with the anaerobic digestion plant. The daily power evolution of the residual load R during typical working and non-working days is reported in Fig. 2.14. In particular, referring to Fig. 2.14a, the platform base load can be identified, which represents the standby condition typical of non-working hours and Sundays. On the other hand, the power profile of residual load during working-days clearly shows high variability and fast dynamics, as can be observed in Fig. 2.14b. Based on such considerations, R can be decomposed in three terms in accordance with (2.29).

$$R(t) = R_b(t) + R_m(t) + R_d(t) \tag{2.29}$$

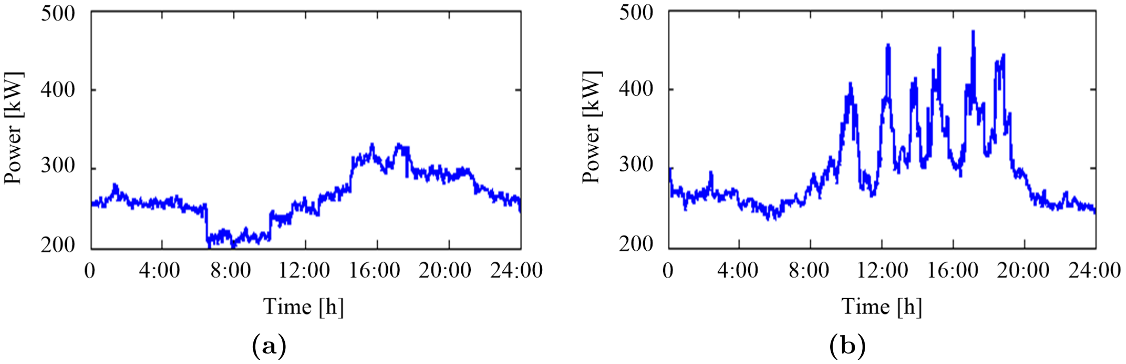

Figure 2.14: *Typical residual load power profiles. (a) Sundays. (b) working days.*

The first element (R_b) represents the base load, while the second (R_m) indicates the average demand, R_d accounting for the fast load variations. Due to their slower response rates, the RES generators are not able to compensate the sudden variations of power demand, highlighting the necessity of decoupling slow and fast load dynamics. Particularly, BESS can be used in order to provide the power compensation of the unavoidable unbalance conditions due to the slower dynamic response of the RES generators.

2.3.1.1 Battery System

Considering a generic battery system, the power effectively exchanged with the grid S can be obtained by (2.30).

$$S(t) = P_c(t) + P_d(t), \tag{2.30}$$

P_d and P_c denoting respectively the power effectively delivered to and drawn from the grid. It is worth noting that P_d and P_c are alternatively equal to zero, since the battery cannot supply and absorb energy from the grid simultaneously. As a consequence, the power S takes positive values when charging and negative when discharging. Moreover, S is constrained by the BESS power exchange boundaries (2.31), defined by the maximum battery charge/discharge current and by the power capabilities of the bidirectional converter.

$$S_{min} \leq S(t) \leq S_{max} \tag{2.31}$$

The stored energy (E) can be subsequently calculated by (2.32).

$$E(t) = E(t-1) + \int_t \left(\frac{P_d(t)}{\eta_d} + \eta_c \cdot P_c(t) \right) dt \tag{2.32}$$

in which η_c and η_d represent the overall charging and discharging efficiency, respectively. Finally, E must comply with upper (E_{max}) and lower (E_{min}) boundaries defined in order to preserve both battery rated performance and lifetime. On the basis of these considerations, the constraints imposed on E lead to:

$$E_{min} \leq E(t) \leq E_{max}. \tag{2.33}$$

2.3.1.2 CHP Generator and Biogas Storage

The existing CHP plant of the waste treatment platform is composed of two identical internal combustion engines, each supplied by different biogas sources as reported in Table 2.2. As previously stated, the J_1 electrical production is completely exploited to power the platform loads whereas the J_2 generation is modulated in order to cover the base residual load and/or the long-period load variations, accounting also for the biogas availability. In fact, the biogas extracted from the landfill (l_G) is stored in a gasometer, which directly feeds the J_2 unit. This means that the power output P_J needs to be properly managed taking into account the corresponding biogas consumption (r_G) and the resultant storage level (SOC_G). Denoting by k the lower heating value and by η_J the efficiency of the CHP genset, (2.34) and (2.35) hold.

The modulation of the CHP electrical power is clearly limited by global constraints given by its maximum rated power (P_J^{max}) and technical minimum (P_J^{min}); however, at each time-step it must also comply with the actual limitation related to the biogas flow and consumption as well as gasometer SOC boundaries (2.36).

$$r_G(t) = \frac{P_J(t)}{\eta_J(t) \cdot k}, \qquad \eta_J = f(P_J) \tag{2.34}$$

$$SOC_G(t) = SOC_G(t-1) + \frac{1}{C_G} \int_t \big(l_G(t) - r_G(t) \big)\, dt \tag{2.35}$$

$$SOC_G^{min} \leq SOC_G(t) \leq SOC_G^{max} \tag{2.36}$$

Table 2.2: *Main characteristics of biogas supplied to CHP units.*

	Anaerobic Digestion	**Landfill**
CHP Unit	J_1	J_2
Methane Content	70%	45%
Lower Heating Value	25120 kJ/Nm^3	16920 kJ/Nm^3

2.3.1.3 CSP Plant

The concentrating solar power plant consists of three main sections: the solar field, the power block and the thermal energy storage system. The solar field is based on the linear Fresnel technology, while the power block is constituted of an Organic Rankine Cycles (ORC) unit with a rated power output of 600 kWe and a 20% net efficiency. The thermal energy storage consists of a packed bed single-tank based on the thermocline principle and containing a low-cost filling material. It has a storage capacity of 14.85 MWh, corresponding to about 5 hours of operation of the power block at design conditions. The performance of the CSP plant is inferred from [79], as a function of solar radiation and position.

2.3.2 Energy Management Operating Strategy

The proposed Energy Management System (EMS) consists of an appropriate rule-based scheduling procedure, as summarized in Fig. 2.15. The management strategy is developed in order to reach a full annual energy balance, obtained by satisfying the instantaneous equality (2.27) at each time-step t. It is worth noting that the term G in (2.27) generally refers to the power transferred from and to the utility grid. However, the EMS aims primarily at satisfying the load demand only by exploiting the microgrid resources, resulting in a power drawn from the main network equal to zero. In this case, G is always negative and represents the MG electric generation delivered to the grid. In order to complain with electricity market requirements and grid operator regulations, feed-in power is often expected to respect forecast productions and/or scheduling programs. In fact, their accomplishment enhances the RES programmability and penetration level, additionally avoiding RES owners to incur in imbalance penalty charges. Based on these considerations, G will henceforth denote the power-to-grid bids of the whole MG system, which are supposed to be constant and mainly related to the expected production of the CSP plant. As a consequence,

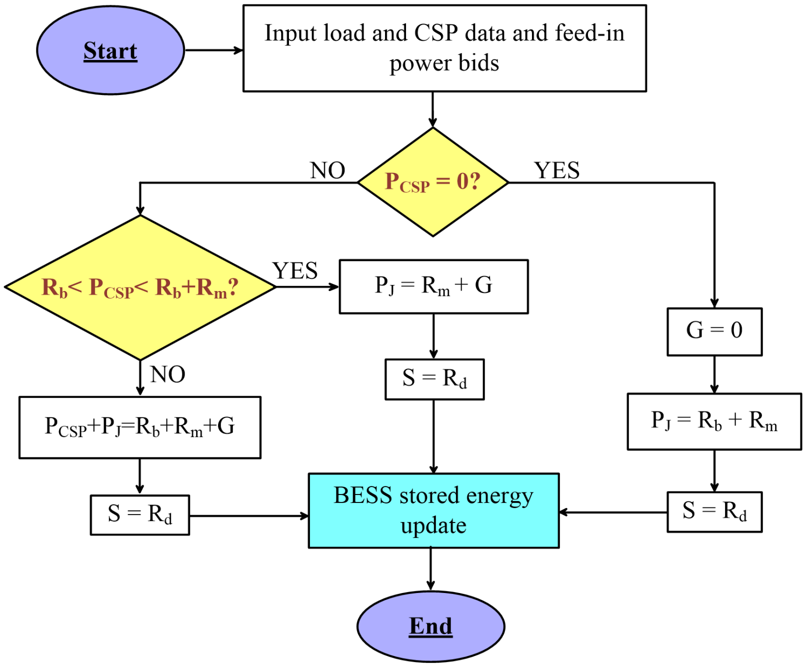

Figure 2.15: *Flow chart of the EMS algorithm: definition process of the MG resource set-points.*

the proposed management strategy has a twofold purpose: besides balancing the MG load, the EMS is in fact required to respect the feed-in power scheduling programs. The flow chart diagram reported in Fig. 2.15 illustrates the main steps in the synthesis of the management strategy. Essentially, the EMS bases the decision process on the evaluation of the potential production of the CSP plant, obtained by considering that this RES system can be turned in a partially dispatchable resource by well-managing its integrated TES. This, in fact, allows the optimal control of the CSP electrical production in order to accomplish the two aforementioned EMS tasks. Additionally, the status of BESS and biogas tank together with maximum and minimum CHP power capabilities are estimated as well, by implementing the battery and CHP models described in (2.30) through (2.36). The expected MG demand and dynamics of residual load variations are then identified and computed by applying (2.28) and (2.29). Finally, the CHP landfill-unit, CSP plant and storages power set-points are determined by following the power dispatching rules summarise in Fig. 2.15, which are mainly built on the following assumptions:

- scheduled power-to-grid profiles: constant and predictable;
- BESS compensates the fast load dynamic variations;

- CSP production: keep constant by exploiting the thermal storage capability;
- CHP genset management rule: minimum load operations rather than shutting down when the whole average and base load is supplied by the CSP plant.

The EMS management strategy enables the recharge of the battery by exploiting the CSP over-production in off-load periods. Moreover, in order to preserve a defined reference state at the end of the control horizon, the BESS could be recharged by the CHP plant during night hours.

The applied EMS operating strategy is implemented in the following simulation studies, assuming a 1-minute decision making interval. Such an operating step has been chosen in order to well-compute the short-term variations of loads and determine the most adequate battery power response accordingly.

2.3.3 Simulations

In order to evaluate the effectiveness of the proposed EMS, a simulation study is carried out by means of the Matlab Software Package. The simulations of the MG operations under the proposed EMS strategy are carried out over a period of two weeks, considering the measured residual load evolution and applying the expected CSP power profiles. Moreover, a BESS characterised by a 500 kWh nominal capacity and 250 kW rated power is taken into account. Since the performance of the microgrid strictly depends on the CSP production, the feasibility of the proposed management strategy needs to be demonstrated under various weather conditions. Consequently, several simulation scenarios were defined in order to compare the results achievable with different CSP power outputs. In particular, the expected CSP production is implemented considering typical days of January, April and July, which are representative of the winter, spring/autumn and summer periods, respectively. However, in order to test the robustness of the proposed microgrid management strategy under challenging operating conditions and to demonstrate its effectiveness regardless of the CSP generation, only the worst scenario is reported and related simulation results analysed. In this case, the two-weeks CSP power profile is obtained considering alternately a sunny day and a cloudy day. Specifically, a zero CSP generation is set for the latter, while the former is referred to the production assessed for a typical sunny day of January. By applying the CSP and TES models from [79] and extrapolating the site solar radiation conditions from the Meteonorm® software, the total production of the CSP plant can be estimated. As previously stated, the

CSP-TES power output is managed in order to achieve a constant profiles over the day: particularly, for the presented case-study, it is assumed to be constant at 400 kWe from 10 a.m. to 5 p.m.

2.3.3.1 Simulation Results

The simulation results can be observed in Fig. 2.16. Specifically, Fig. 2.16a shows the time evolution of MG resources power outputs for a general two-weeks period whereas Fig. 2.16b focus closely on a shorter time-horizon of two-days, giving a more extensive appreciation of the management outcomes. In addition, the battery power and stored energy profiles are detailed in Fig.2.16c for the whole simulation period. It can be observed that the proposed microgrid configuration and management strategy allow the dispatch of power to the main grid with a programmable profile. The feed-in power is in fact set constant to 200 kW during CSP operating hours. Such a value can be effectively achieved and maintained by exploiting also the CHP unit operations at minimum load. The lower load demand recorded during weekends allows the power-to-grid profile to be then increased to 300 kW, providing a non-null CSP production. Different observations need to be made when the power profiles derived for cloudy days are analysed. In this case the CHP unit supplies both the average and base residual load, while the fast load dynamics are compensated by the battery in accordance with the EMS dispatching rules in Fig. 2.15. Since the priority of the strategy is fully balancing the microgrid electrical energy demand, the power-to-grid is in this case fixed to zero.

Overall, the reported results highlight that the integration between the CSP-TES system and the battery storage, along with the adoption of a proper energy management strategy, makes the achievement of the annual and instantaneous electrical balance feasible for the benchmark MG. This could consequently result in the reduction of contracted power of the waste treatment plant, substantially cutting its electricity bill. Moreover, the EMS goal of trading energy respecting scheduling profiles is accomplished, as well. The reliability of feed-in power scheduling programs could be a very remunerative requirement, additionally avoiding to incur in economic duties related to errors in forecasting of local demand and production. Finally, the integration of the small-scale CSP-TES plant and the BESS would provide more flexibility to the overall system, increasing the security of power supply even in the case of outage of the distribution grid or problems with a CHP unit.

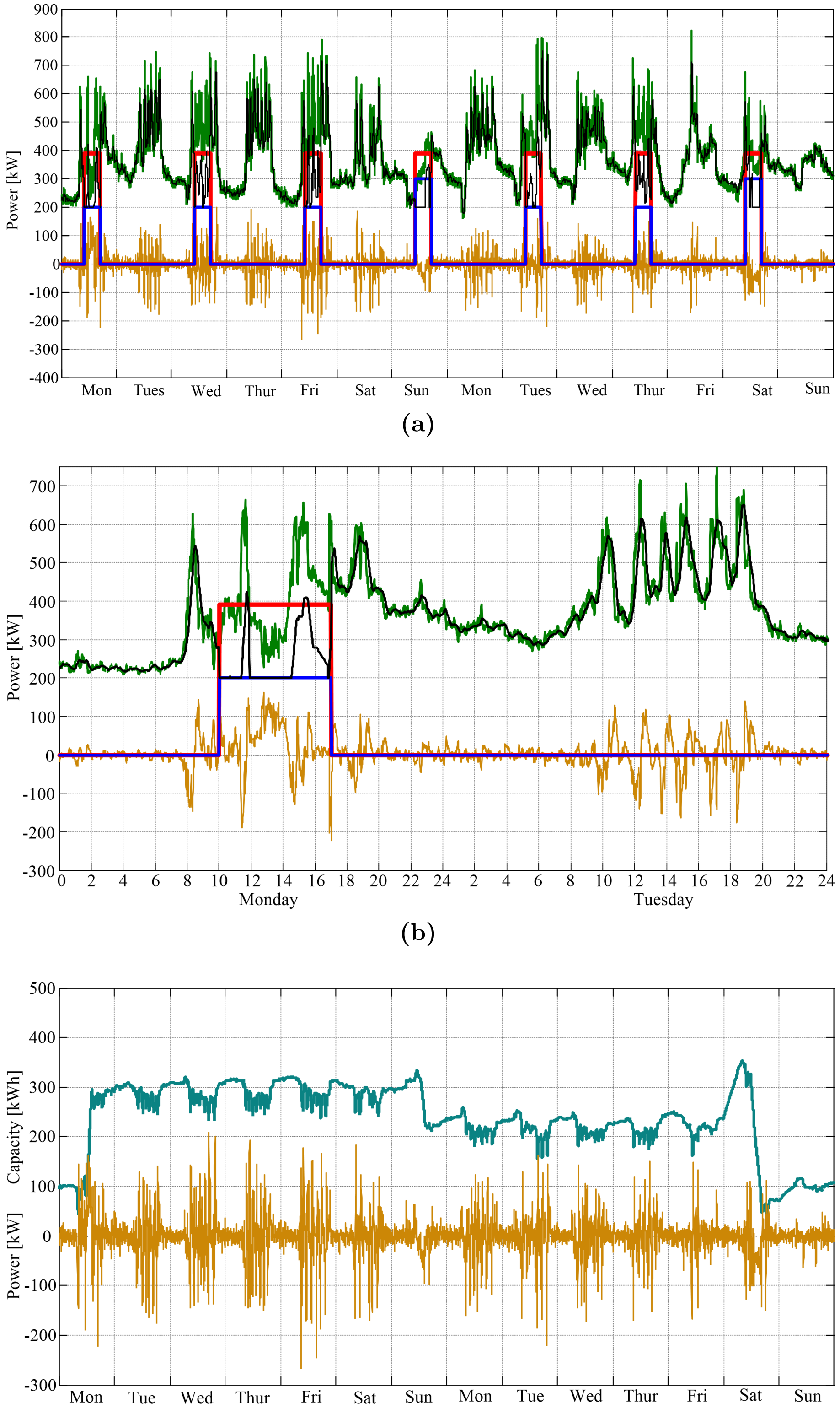

Figure 2.16: *Time evolution of MG electrical residual load (green), CHP landfill-genset production (black), CSP plant power output (red), battery charge/discharge power (purple) and feed-in power (blue). (a) Two weeks. (b) Detail: two days. (c) Two weeks evolution of BESS stored energy (orange) and power (purple).*

2.4 EV Storage System in a Cluster of Microgrids

The previous sections have demonstrated the improvements in MG and VPP operations due to the integration of storage systems both in centralised and distributed configurations. As highlighted in the preceding analyses, the feasibility of achieved results is strictly related to the effectiveness of the applied management algorithm, which is derived from rule-based strategies (RBS) in the case-study of Sections 2.2-2.3. These management strategies are characterised by a combinational behaviour in which past and future estimations related to the evolution of the system are neglected. In fact, the energy manager takes decision based only on current information. Due to such characteristics, RBS require low computational effort and consequently are suitable for on-line implementation. However, they need a wide knowledge of the system application and component models in order to determine proper and effective management rules. Presently, several applications implement this kind of energy management strategies: such as storage-photovoltaic systems [80], HES, microgrids and Electric Vehicles [81]. In such cases, the RBS can become quite complex because of the large number of control parameters involved. For instance, the EMS needs to take into account several conditions, including the SOC of the ESS, loads power requirements, operation mode, etc. As a consequence, the set of possible conditions greatly increases, making the effectiveness of the management strategy less robust in case of system modifications. Clearly, the RBS are capable of controlling the application system but do not ensure its optimal behaviour. To this end, optimisation methods need to be applied.

Several strategies have been proposed in the literature [53, 82–88] to solve the problem of optimising a given performance index by determining profiles of control and state variables. For the applications listed above, optimal controllers based on dynamic programming (DP) are often implemented [50–52]. This numerical method is based on the Bellman's principle of optimality and guarantees the global optimal solution but requires the knowledge of the entire system evolution. Moreover, since DP solves partial differential equations, the computational load exponentially rises with the increase of state variables dimension. This disadvantage is called *curse of dimensionality* and amplifies the computational complexity, limiting the DP implementation for large systems and real-time applications. Another approach is based on analytical optimisation methods that consider the whole system evolution as well, but use an analytical problem formulation to find the solution in a closed form. Among these methods, Pontryagin's minimum principle (PMP) has been recently introduced and implemented, especially in order to control hybrid electric vehicles [54, 89, 90].

PMP is a special case of Euler-Lagrange equation originating from the calculus of variations. It requires less computing time than DP because solves non-linear second-order differential equations which increase linearly with the variable dimension. However, PMP provides only necessary conditions, implying that the obtained optimal trajectory could be a local optimal and not a global solution. In spite of this, under certain assumptions the necessary conditions from PMP become sufficient for obtaining a global optimal control. Besides, PMP application allows the reduction of global criterion to an instantaneous optimisation, making feasible its real-time implementation and the achievement of a continuous-time control strategy. Therefore, this approach could be effectively used to solve the problem of the optimal management of power flows in MGs integrating storage systems and renewable generators.

In this Section, a novel application of the PMP approach is proposed referred to the optimal integration of V2G storage in a cluster of MGs. An one-day ahead scheduling procedure for global optimisation is consequently developed in order to define the daily charging/discharging profiles of each EV operating within MGs. The synthesis of the optimal solution is carried out referring to an appropriate objective function, which is defined considering the optimal contribution of each EV to the minimisation of the daily energy exchange between the MGs and the main electricity network. The worth and effectiveness of the proposed approach are subsequently verified through a simulation case study, which refers to two MGs connected in an unconventional manner by means of an EV operating in V2G mode.

2.4.1 MGs Cluster Modelling

A cluster of grid-connected MGs, which is schematically represented by the structure shown in Fig. 2.17, can be usefully adopted in order to enable a cooperative frame among MGs. In fact, heterogeneous MGs could be characterised by complementary load time distributions and power generations, thus offering the opportunity of a cooperative energy integration. In particular, the coordination and management of the power transferred to/from each MG give great opportunities to maximise the self-consumption, optimise the local use of RES production as well as improve the global stability of the grid. However, considering each MG operating by means of its

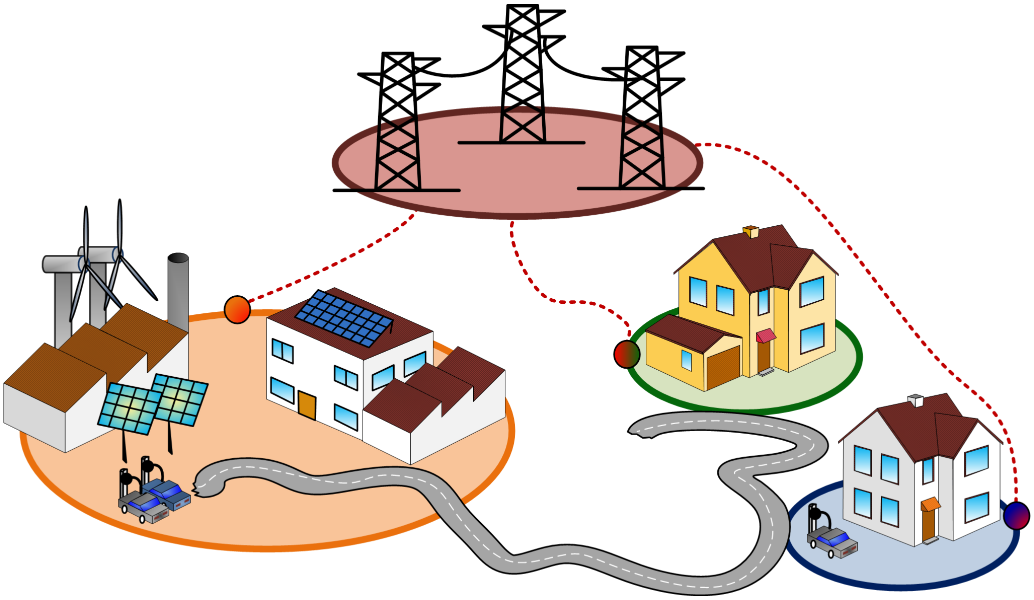

Figure 2.17: *Schematic representation of the microgrids structure.*

own point of common coupling (PCC), the direct power exchange within the cluster is not possible. In this case, an EV fleet providing V2G services could be effectively exploited as distributed and mobile storage system, becoming an unconventional and additional power network, connecting each MG to the others.

2.4.1.1 Mathematical Modelling of EV Storage Systems

The time evolution of the energy stored in the battery of the j-th EV can be described by the following continuous state equation:

$$\begin{cases} \dot{e_j}(t) = -\left(\dfrac{p_{d_j}(t)}{\eta_d} + \eta_c \cdot p_{c_j}(t) + p_{r_j}(t)\right) \\ e_j(t_0) = e_{0_j} \end{cases} \tag{2.37}$$

where η_c and η_d represent the overall charging and discharging efficiency, respectively; e_{0_j} is the energy storage state at the initial time t_0 for the j-th EV; $p_{d_j}(t)$ denotes the power effectively delivered to the grid, and $p_{c_j}(t)$ the power effectively drawn from the grid, $p_{r_j}(t)$ being the power requested to the EV battery during driving.

Subsequently, introducing the general term s_j for denoting the power effectively exchanged with the grid by the j-th EV, (2.38) holds. It is worth noting that p_{c_j} and p_{d_j} are alternatively equal to zero, since each EV cannot supply and absorb energy from the grid simultaneously. As a consequence, s_j can be obtained by (2.39). In particular, the power s_j takes positive values when discharging and negative when charging.

$$\begin{cases} p_{d_j}(t) = \frac{1}{2}\left(s_j(t) + |s_j(t)|\right) \\ p_{c_j}(t) = \frac{1}{2}\left(s_j(t) - |s_j(t)|\right) \end{cases} \tag{2.38}$$

$$s_j(t) = p_{c_j}(t) + p_{d_j}(t) \tag{2.39}$$

Moreover, s_j is constrained by the EV power exchange boundaries (2.40), defined by the maximum battery charge/discharge current and by the maximum power flow permitted by the grid interconnection line. In addition,the stored energy e_j must comply with upper (e_{max_j}) and lower (e_{min_j}) boundaries defined in order to preserve both battery rated performance and lifetime. On the basis of these considerations, the constraints imposed on e_j lead to (2.41).

$$s_{min_j} \leq s_j(t) \leq s_{max_j} \tag{2.40}$$

$$e_{min_j} \leq e_j(t) \leq e_{max_j} \tag{2.41}$$

2.4.1.2 Mathematical Modelling of V2G Integration in MGs

Referring to the structure of Fig. 2.17, a number of N MGs can be considered. The instantaneous electric power balance of the i-th MG can be consequently expressed by:

$$g^i(t) + r^i(t) + s^i(t) = 0 \qquad i \in \{1, ..., N\}. \tag{2.42}$$

Considering (2.42), g^i is the total power traded by the MG with the main grid, s^i represents the power exchanged by all the EVs plugged at the i-th MG, as defined by (2.43), while r^i indicates the MG residual load, which is obtained from (2.44).

$$s^i(t) = \sum_{j=1}^{M} s^i_j(t) \tag{2.43}$$

$$r^i(t) = P^i_{RES}(t) + L^i(t), \tag{2.44}$$

where M represents the total number of EVs managed in the involved group of MGs, P^i_{RES} being the power generated by RES and L^i denoting the electric demand of the

i-th MG.

2.4.2 Optimal V2G Management Strategy

The one-day ahead scheduling of EV charging/discharging profiles is obtained defining the optimal contribution of each EV to the minimisation of the daily energy exchange between MGs and the main grid. This aims at reducing the MGs dependence from the distribution utilities and increasing the energy autonomy of the MGs cluster. In terms of optimisation problem, such an objective function can be formulated as follows:

$$\begin{aligned} J(s_j^*(t)) &= \ \mathbf{min}\ J(s_j) \qquad\qquad \forall j \in \{1, ..., M\} \\ J(s_j(t)) &= \int_0^T f(s_j(t))\,dt = \int_0^T \left(\sum_{i=1}^{N} g^i(s_j(t))^2\right) dt \end{aligned} \tag{2.45}$$

subject to

$$\begin{cases} \dot{e}_j(t) = -(\alpha \cdot s_j(t) + \beta \cdot |s_j(t)|) - p_{r_j}(t) & (2.46) \\ e_j(t_0) = e_{0_j} & (2.47) \\ e_j(T) = e_{T_j}. & (2.48) \end{cases}$$

In particular, (2.46) is obtained by the combination of (2.37) and (2.39), α and β being defined by (2.49):

$$\begin{cases} \alpha = \dfrac{1}{2}\left(\dfrac{1}{\eta_d} + \eta_c\right) \\ \\ \beta = \dfrac{1}{2}\left(\dfrac{1}{\eta_d} - \eta_c\right) \end{cases} \tag{2.49}$$

Finally, control and state variables constraints need to be considered for the proper formulation of the optimal problem. These are defined in (2.40) and (2.41) for all $t \in [0, T]$, but can be best computed in the following forms:

$$y_j(t) = (s_j(t) - s_{min_j})(s_j(t) - s_{max_j}) \leq 0 \tag{2.50}$$

$$k_j(t) = (e_j(t) - e_{min_j})(e_j(t) - e_{max_j}) \leq 0 \tag{2.51}$$

The solution of such an optimal control problem is derived by applying the Euler-

Lagrange approach and, in particular, its generic formulation in terms of Pontryagin's minimum principle. In particular, the optimal problem can be analytically solved by finding the optimal control law which minimises the cost functional (2.45). Starting from these considerations, the problem statement can be formulated as follows:

Find a vector of optimal controls $s_j^* := \{s_j \in \Re : y_j \leq 0, \forall t \in [0,T]\}$ *and the corresponding vector of optimal responses* $e_j^* := \{e_j \in \Re : k_j \leq 0, \forall t \in [0,T]\}$ *such that the dynamic system* (2.46) *is transferred from the initial state* (2.47) *to a fixed value at the final time* T (2.48) *and such that the performance criterion* (2.45) *is minimized.*

Then, the PMP requires the definition of the Hamiltonian function which can be formulated as:

$$\mathcal{H} = f(s_j(t)) + \sum_{j=1}^{M} \lambda_j(t)\dot{e}_j(t) \tag{2.52}$$

λ_j being the adjoint variables, assuming $\lambda_0 = 1$ (regular case).

The constraints on the state variables need to be also considered in the Hamiltonian, in order to deal with the variations of the state before applying necessary conditions of optimality. Since k_j does not explicitly depend on the control variables and e_j can be controlled only indirectly via propagation through the state equations, k_j should be differentiated with respect to t in order to find a dependence on s_j as in (2.53).

$$\dot{k_j}(t) = \dot{e_j}(t)(2e_j(t) - e_{max} - e_{min}) = -(\alpha \cdot s_j(t) + \beta \cdot |s_j(t)|)(2e_j(t) - e_{max} - e_{min}) \tag{2.53}$$

Associating a proper multiplier function μ_j, the first time derivative of state constraint $\dot{k_j}$ is adjoined to $\mathcal{H}$, leading to the definition of the Lagrangian function (2.54).

$$\mathcal{L} = \mathcal{H} + \sum_{j=1}^{M} \mu_j(t)\dot{k}_j(t) \tag{2.54}$$

Moreover, the vector function μ_j must satisfy the following conditions:

$$\mu_j(t)k_j(t) = 0, \qquad \mu_j(t) \leq 0. \tag{2.55}$$

Particularly, (2.55) implies μ_j=0 each time k_j<0, which is verified in time periods when the state boundaries (2.41) are not violated. On the basis of the Euler-Lagrange equations, the necessary optimality conditions assume the form reported in (2.56) through (2.58).

$$\dot{e}_j^* = \frac{\partial \mathcal{L}}{\partial \lambda_j} \tag{2.56}$$

$$\dot{\lambda}_j^* = -\frac{\partial \mathcal{L}}{\partial e_j} \tag{2.57}$$

$$0 = \frac{\partial \mathcal{L}}{\partial s_j} \tag{2.58}$$

Furthermore, according to PMP, (2.45) is minimised when the control variables satisfy the minimum condition (2.59).

$$\mathcal{H}(s_j^*(t), e_j^*(t), \lambda_j^*, t) \leq \mathcal{H}(s_j(t), e_j^*(t), \lambda_j^*, t) \tag{2.59}$$

Remark: By applying (2.51)-(2.59), the resulting time-evolution of e_j^* could clearly highlight values of the state variables greater than the battery boundaries (2.41). As a consequence, indicating by θ_1 the instant time when the state boundary is hit (*entry time*):

$$k_j(\theta_1, e_j^*(\theta_1) = 0, \tag{2.60}$$

the adjoint variables and Halmitonian function may have discontinuities of the following form:

$$\lambda_j^*(\theta_1^-) = \lambda_j^*(\theta_1^+) + \pi_j(\theta_1)\frac{\partial k_j(\theta_1, e_j^*(\theta_1)}{\partial e_j} \tag{2.61}$$

$$\mathcal{H}(\theta_1^-) = \mathcal{H}(\theta_1^+) - \pi_j(\theta_1)\frac{\partial k_j(\theta_1, e_j^*(\theta_1)}{\partial t} \tag{2.62}$$

where $\pi_j(\theta_1)$ is a Lagrange multiplier. Condition (2.62) determines the entry time θ_1, while $\pi_j(\theta_1)$ is so chosen that the constraint (2.60) is satisfied, through the adjoint equations (2.57) and (2.61).

2.4.3 Case of Study

In order to evaluate the effectiveness of the proposed optimal V2G scheduling approach, a case study is analysed, showing a possible application of the optimal problem formulation presented in the previous section. The case study illustrated in Fig. 2.18 is supposed to be basically constituted of two MGs: a family-run company W

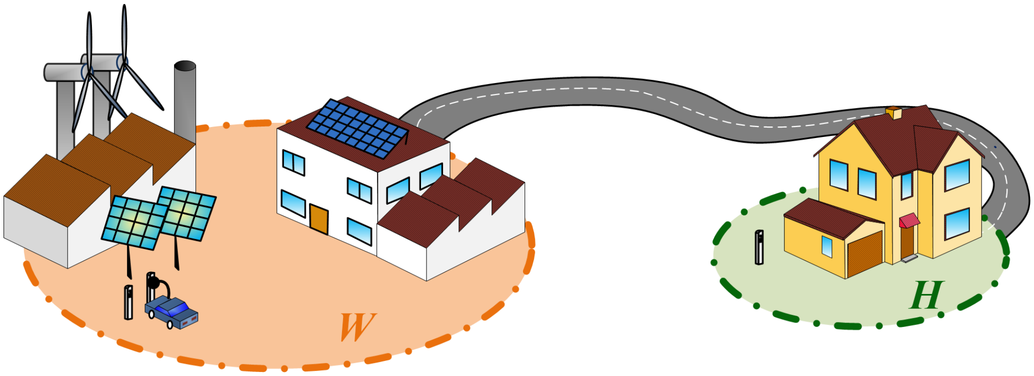

Figure 2.18: *MGs clsuter: case of study.*

and a house H, where one of the employers lives. In addition, the latter is assumed to drive an EV to commute. In this case, the mathematical formulation can assume the form reported in the following. In particular, (2.45) can be expressed as:

$$\begin{aligned} J(s^*(t)) &= \ \mathbf{min}\ J(s(t)) \\ J(s(t)) &= \int_0^T \Big(g^W(s(t))^2 + g^H(s(t))^2 \Big) dt \end{aligned} \tag{2.63}$$

As a consequence, by introducing (2.42), (2.46) and (2.63) in (2.52), the Hamiltonian becomes:

$$\mathcal{H} = \big(r^W(t) + s^W(t)\big)^2 + \big(r^H(t) + s^H(t)\big)^2 - \lambda\big(\alpha \cdot s(t) + \beta \cdot |s(t)|\,\big) \tag{2.64}$$

It's worth noting that the control variables s^W and s^H are alternative equal to zero since the EV can not be in more than one location at the same time, their corresponding relationship being defined by (2.65):

$$s(t) = s^W(t) + s^H(t). \tag{2.65}$$

Moreover, when driving there is no power exchanged between the EV and the MGs and the condition $s(t) = 0$ holds. In these time intervals, the battery energy consumption is computed by the term $p_r(t)$, as in (2.37). The optimal control $s^*(t)$ can be then synthesised by applying (2.58)-(2.59). However, considering the resulting evolution of the state variable, the obtained optimal power profile could be accordingly modified. In fact, the identification of a constraints violation for a feasible response $e(t)$ leads the system to work in a *boundary interval* $[\theta_1, \theta_2]$, where:

$$k(t) = 0 \qquad \forall t \in [\theta_1, \theta_2] \tag{2.66}$$

As soon as the violation occurs, the EV exceeding the limits will be disconnected from the MG since no more power can be accepted or delivered by the battery. As a consequence, for $t \in [\theta_1, \theta_2]$ the optimal control s^* is determined by $s^* = 0$, while $e^* = e_{max,min}$. Being e^* constant, (2.67) holds.

$$\dot{e}^*(t) = 0 \qquad \forall t \in [\theta_1, \theta_2]. \tag{2.67}$$

By introducing (2.53) and (2.67) in (2.54), the Lagrangian becomes:

$$\mathcal{L} = \mathcal{H} \qquad \forall t \in [\theta_1, \theta_2] \tag{2.68}$$

Since the Hamiltonian function does not depend explicitly on the state variable, (2.57) leads to:

$$\dot{\lambda}^* = 0 \Longrightarrow \lambda^* \equiv cost \qquad \forall t \in [\theta_1, \theta_2] \tag{2.69}$$

Referring now to a non-boundary interval, the condition $k(t) < 0$ is always verified, entailing $\mu(t) = 0$ by applying (2.55). Subsequently, the following conditions can be easily derived:

$$\mathcal{L} = \mathcal{H} \Longrightarrow \dot{\lambda}^* = 0 \Longrightarrow \lambda^* \equiv cost \tag{2.70}$$

Then, the final optimal control s^* must satisfy again the following optimality conditions derived from (2.58), (2.59) and (2.50).

$$\begin{cases} \tilde{s}^W(t) + \tilde{s}^H(t) = \lambda(\alpha + \sigma\beta) - \left(r^W(t) + r^H(t)\right) \\ \sigma = sign(\tilde{s}(t)) \end{cases} \tag{2.71}$$

$$s^*(t) = \begin{cases} \tilde{s}(t) & \text{for } y(t) < 0 \\ s_{max,min} & \text{for } y(t) = 0 \end{cases} \tag{2.72}$$

The proposed optimal control strategy for this case study is implemented in the

Matlab environment over a period T of 24 h, with a 1 minute time-resolution. For this purpose, the main characteristics of the electric vehicle and its mobility habits, W load and generator as well as H energy requirements have to be defined. First of all, an EV daily travel program is considered as reported in Table 2.3. The EV energy consumption is set equal to 0.2 kWh/km. Such a value is quite high compared to nominal consumptions reported in data-sheets of many commercial EVs. Nevertheless, real world test cases found consumption values very close to that assumed in this study [91]. Moreover, a battery capacity of 30 kWh is considered. However, since the SOC range of the battery is constrained to increase its lifetime, in the simulations the SOC is assumed to vary within a $20\% - 80\%$ range. As a consequence, the usable battery capacity is limited to 18 kWh. In addition, 3 kW bi-directional power grid connections are considered in both W and H, whereas the overall charging and discharging efficiencies are set to 90% and 85% respectively.

Regarding MGs, W is locally supplied by a 10 MW PV plant and a 3 MW wind farm which provide electrical energy to an industrial zone characterised by a peak load equal to 15 kW. Moreover, a 10 MW maximum load is assumed for the H microgrid. Specifically, the electric load and generation of W and H are chosen to be coherent with real operating conditions and for this reason they are extracted from actual data of Sardinian RES power plants and residential and commercial districts [92]. Two scenarios are then defined in order to compare results of the optimal V2G scheduling strategy in different demand and generation conditions. In greater details, the evolution of RES production in *Case A* is typical of a sunny and poor windy day, as can be seen in Fig. 2.19a. In contrast, in *Case B*, P_{RES}^{W} assumes a more fluctuating daily evolution and a much lower peak value. Similar considerations can be made for the W district load depicted in Fig. 2.19b, in which the peak demand of *Case B* doubles the one in *Case A*. As far as the power flow between the W MG and the main grid is concerned, the scenario profiles can be observed in Fig. 2.19c. It can be noticed that in *Case A* a RES overproduction

Table 2.3: *EV daily plans for 30 km commuting distance*

	0:00-7:00	**7:01-8:00**	**8:01-17:00**	**17:01-18:00**	**18:01-24:00**
Home	X				X
Work			X		
Moving		X		X	

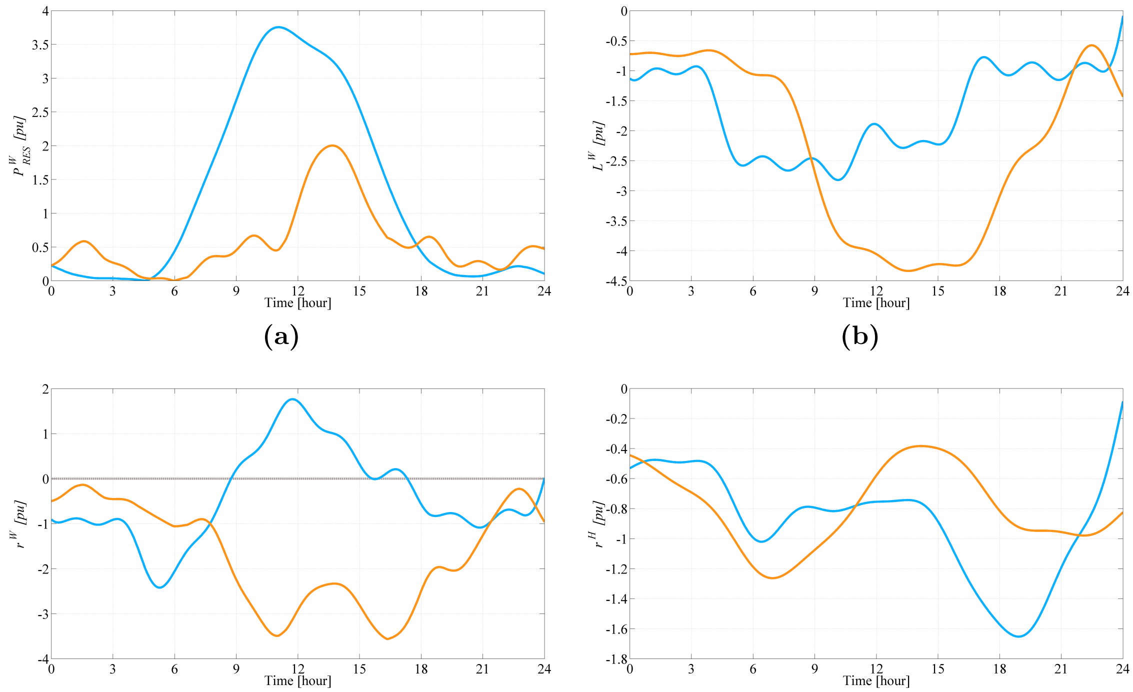

(a) **(b)**

(c) **(d)**

Figure 2.19: *The forecasted daily evolution of: (a)* P^W_{RES}*, (b)* L^W*, (c)* r^W *and (d)* r^H *in pu with respect to the EV maximum bi-directional power. Case A (cyan) and Case B (orange).*

occurs during the central hours of the day, whereas in *Case B* the W MG is always seen by the grid as a load, because L^W is always higher than P^W_{RES}. The evolutions of household load are finally shown in Fig. 2.19d. In order to verify the effectiveness of the proposed optimal management strategy, the results obtained in the two scenarios are both compared with a case in which the EV is not introduced, and a configuration where the EV is recharged by a dumb strategy. The latter recharges the EV at its rated power as soon as it is plugged into the socket, in order to reach the maximum allowed SOC. In the proposed optimal control strategy, the initial and final SOC are assumed equal to 50%, in order to avoid high average SOC, which negatively affect the battery lifetime, and to be initially ready to exchange energy with the power grid [93].

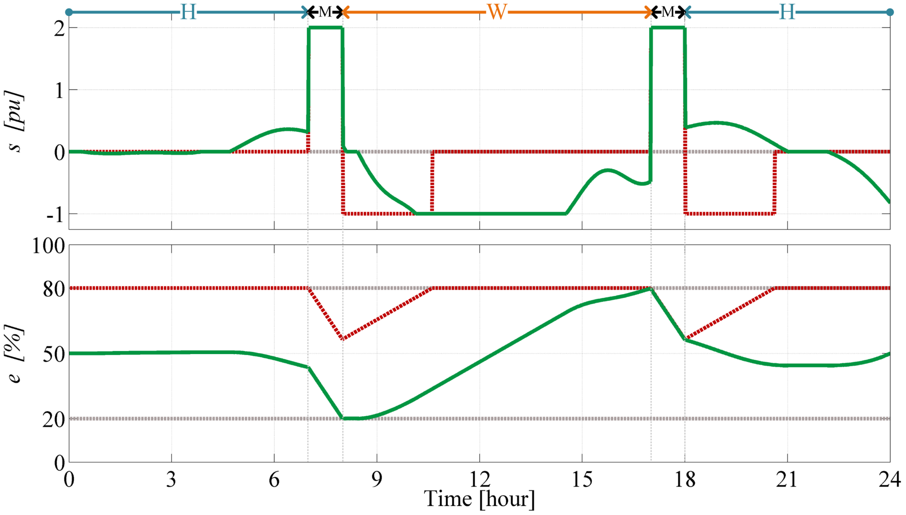

Figure 2.20: *The daily evolutions of* s^* *and* e^* *in Case A: dumb charging (red) and optimal control strategy (green).*

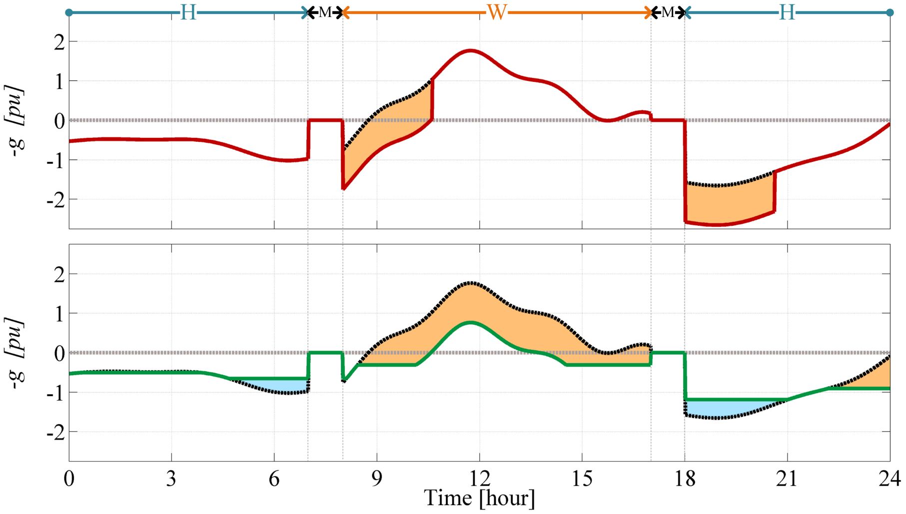

Figure 2.21: *The daily evolutions of the power exchanged between the MGs and the main grid in Case A: without EV (black), dumb charging (on the top, in red) and optimal control strategy (on the bottom, in green). The orange areas represent the energy absorbed by the EV, whereas the cyan ones represent the energy delivered by the EV storage system.*

2.4.3.1 Case A

This scenario is characterised by a H load that features two consumption peaks in the morning and in the late evening, and by a W high renewable production, particularly concentrated during the working hours. In Fig. 2.20 the daily trends of the optimal control s^* and the corresponding evolution of e^* are reported. Both

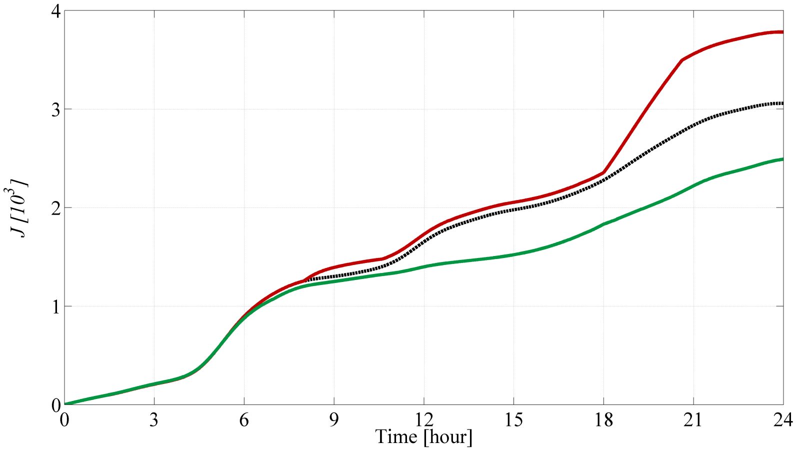

Figure 2.22: *The daily evolutions of objective function in Case A: without EV (black), dumb charging (red) and optimal control strategy (green).*

quantities are compared with those obtained by implementing the dumb charging strategy. These results can be better analysed also considering the daily trends of the power exchanged between the MGs and the main grid, reported in Fig. 2.21. Particularly, the lower sub-plot shows the energy performance of the proposed optimal control. The coloured areas highlight the effects of the V2G service to the minimisation of energy flow between MGs and the main grid. The comparison with the dumb charging, reported in the upper sub-plot, highlights the obtained improvement. By referring again to Fig. 2.20, the optimal strategy outcomes can be better appreciated. Specifically, in the first part of the day, the EV is discharged to cover the morning house loads only two hours before to leave: this in fact ensures to cover the highest load peak and have enough energy to commute. Then, at work, the EV starts charging about 20 minutes after his arrival in order to be able to absorb the most of surplus energy around midday. Here, the power drawn by the EV is limited by the boundaries on the control variable s, as highlighted in Fig. 2.20. As soon as the EV is plugged at home in the evening, the V2G process is enabled and the vehicle discharges in order to cover partially the house electrical demand during the evening peak hours. Finally, at the end of the day when the lowest demand is expected, the EV is gradually recharged up to the desired final SOC (50%). The time evolutions of the objective function J depicted in Fig. 2.22 and its final values reported in Tab. 2.4 corroborate the effectiveness of the proposed optimal V2G strategy. In fact, as expected, the EV optimal management substantially reduces (by 34%) the performance criterion respect to the dumb charging result. Furthermore, it is in-

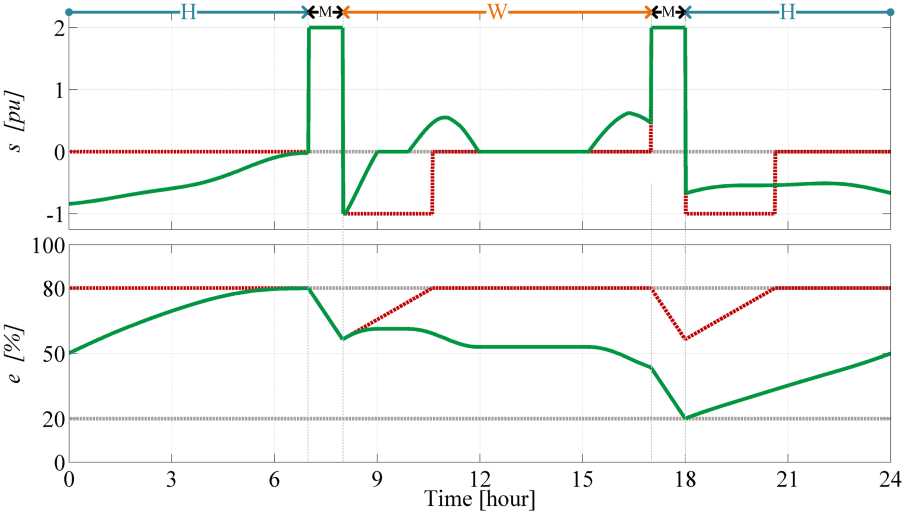

Figure 2.23: *The daily evolutions of s^* and e^* in Case B: dumb charging (red) and optimal control strategy (green).*

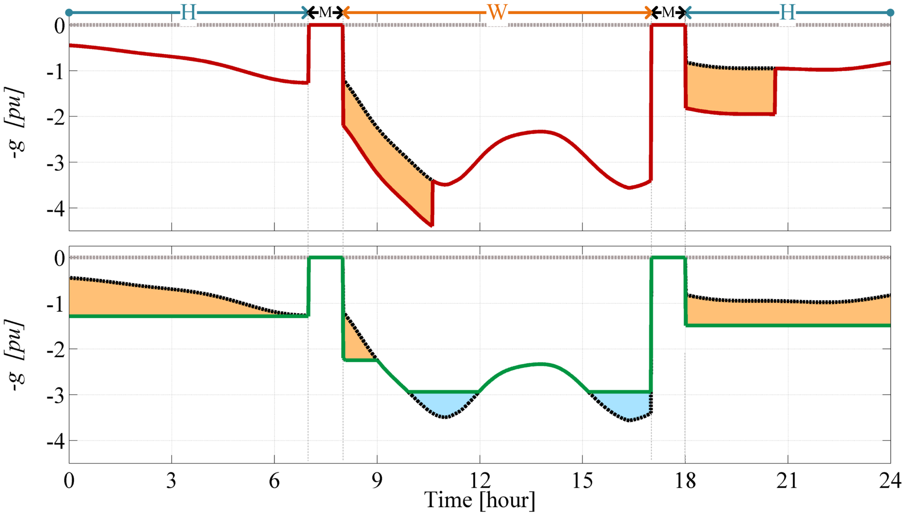

Figure 2.24: *The daily evolutions of the power exchanged between the MGs and the main grid in Case B: without EV (black), dumb charging (on the top, in red) and optimal control strategy (on the bottom, in green). The orange areas represent the energy absorbed by the EV, whereas the cyan ones represent the energy delivered by the EV storage system.*

teresting to point out that J is also optimised respect to the MGs system without EVs, indicating the worth of the presented optimal approach for the reduction of the MGs dependence from the main grid, and for the increase of their energy autonomy. Clearly, these outcomes strictly depend on the production and consumption profiles, which in this case are mainly characterised by a great excess of RES energy gener-

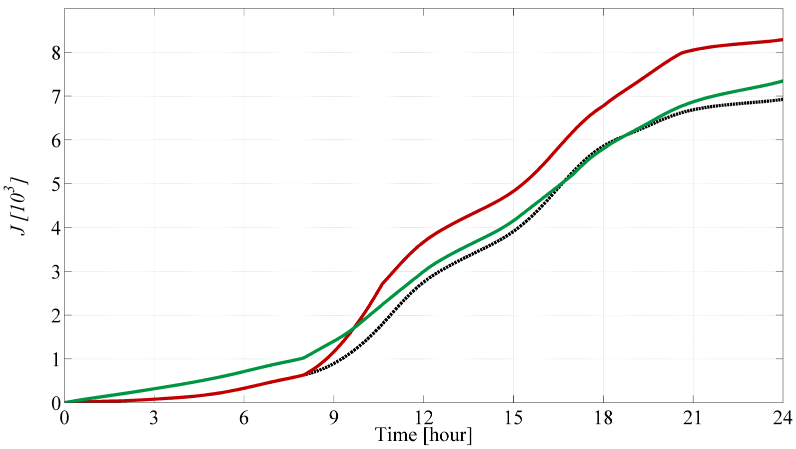

Figure 2.25: *The daily evolutions of objective function in Case B: without EV (black), dumb charging (red) and optimal control strategy (green).*

ation. Since the proposed optimal strategy aims at effectively working regardless of the PV and wind productions, a worse scenario is analysed in the *Case B*.

2.4.3.2 Case B

The same simulation results developed in *Case A* are reported for *Case B* in Figs. 2.23-2.25. The *Case B* reflects a situation that can frequently happen during the fall or winter months. In fact, the electricity generation from RES is very poor and at each hour of the day W and H have to resort to the main grid in order to cover their electric loads. As a consequence, the introduction of an EV worsens in any case the MGs energy unbalance since it needs to be recharged during the day, increasing the total load to be supplied by the main grid, as highlighted by the orange areas in Fig. 2.24. Nevertheless, referring to the results shown in Figs. 2.23-2.25 and Table 2.4, the optimal control of the EV allows the achievement of better results respect to the case of an uncontrolled charging, reducing by 13% the value of the objective function. In particular, the proposed optimal control enables the EV recharge only

Table 2.4: *Scenarios Objective Function results*

	MGs without EVs	**Dumb Charging**	**Optimal V2G**
Case A	3056.8	3780.6	2490.9
Case B	6922.8	8286.1	7342.4

during the hours when the electricity demand is the lowest, such as in the early morning, evening and at night, concentrating the discharge periods at work where the highest peak loads are expected. Moreover, it's worth observing, by the analysis of Fig. 2.23, that, initially, the battery charges up to its maximum SOC in order to be able to both commute and provide energy at work, reducing consequently the local power unbalance. From these considerations, it is evident that the proposed V2G scheduling strategy can optimally manage the charge/discharge processes even in the conditions of both low RES production and high peak load, as highlighted by the results reported for this case.

2.4.3.3 State of Charge Analysis

An important aspect to be considered when dealing with EVs charging algorithms is the influence of the management strategy on the battery lifetime. The technical literature [93,94] suggests that one of the parameters most affecting the battery ageing is the average SOC. In fact, especially high SOC are demonstrated to be a strong acceleration factor for the reduction of the battery calendar life. In particular, such states-of-charge correspond to high electrode potentials, causing electrolyte decomposition and finally the reduction of the battery capacity [93]. Moreover, [93, 94] highlight that the cycling effect, which is more emphasized in V2G applications, contributes to the overall battery ageing less than long rest periods at high SOC, hence the latter being the main cause of battery ageing. Starting from these considerations, the average SOC has been calculated for the cases A and B and compared with the dumb charging. The results are reported in Tab. 2.5 and allows to give some interesting remarks, especially when analysed together with the SOC profiles shown in Figs. 2.20 and 2.23. Particularly, it is evident that the proposed optimal EV management strategy decreases standstill time at high SOC. As a consequence, in both cases, the average SOC is drastically lower than that recorded for the dumb charging approach.

Table 2.5: *Average SOC results*

	Dumb Charging	**Optimal V2G**
Case A	0.76	0.49
Case B	0.76	0.54

In conclusion, the simulation results have highlighted that the proposed optimal V2G scheduling strategy can be effectively implemented in order to minimise the dependence of MG clusters from the main grid and increase their energy autonomy. In particular, the optimal management of EV charging/discharging processes enables the cooperation among MGs and exploits the capabilities of V2G as distributed and mobile storage system.

2.5 A Battery Management Strategy for Microgrids

The previous section has demonstrated the effectiveness of the proposed optimal management approach for the one-day ahead scheduling of V2G service. Similarly, this control strategy can be effectively implemented for centralised storage systems in order to optimise its use in *Demand Response* (DR) and RES buffering applications. In the context of smart grid, several advantages could be in fact provided to utilities, system operators and customers by optimal management strategies, including maximisation of RES energy exploitation and profitability, as well as minimisation of costs and peak loads. In particular, consumers can be stimulated by utilities to join Demand Response (DR) programs by means of dynamic electricity pricing strategies enabled by new smart metering systems [57]. Basically, dynamic pricing can be grouped into two categories: time-of-use pricing and real-time pricing. The former typically provides two or three price levels associated with specific time slots, while the latter is based on hourly energy prices, better reflecting the prices on the wholesale energy market. Clearly, dynamic prices represents an opportunity for customers (from service sector to households) to exploit price variations for the reduction of the electricity bill, also achieving additional benefits, such as lowering demand peaks, maximizing the self-consumption and optimising the local use of RES production. Despite this, in practical cases, consumers are responding less than expected to changing in electricity prices [57]. This happens mainly because a demand-side-management essentially requires a change in the customer electricity usage habits that is not always effectively implemented or practicable.

A microgrid with energy storage devices and implementing an Optimal Management Strategy (OMS) can be a promising solution for providing DR functionality without significantly forcing users to shift and adjust their consumptions [95, 96].

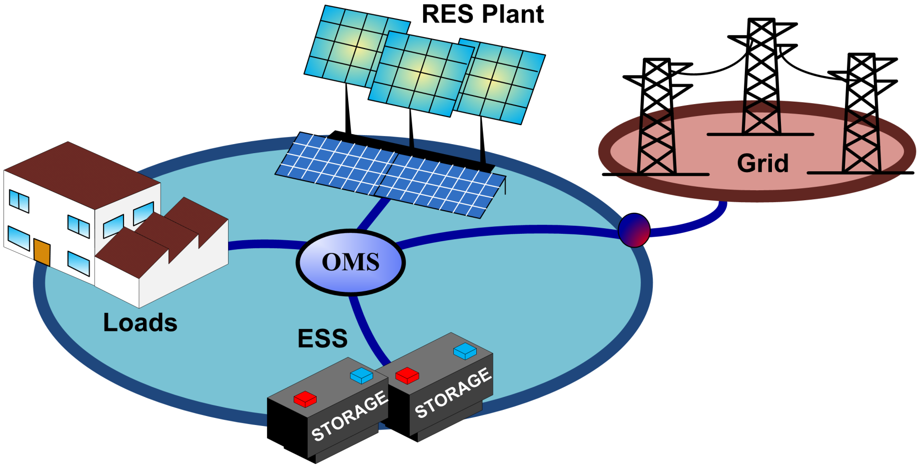

Figure 2.26: *Schematic representation of a grid-connected hybrid microgrid.*

However, the current high cost of energy storage technologies requires the development of an OMS that optimally manages the storage units, considering the ESS power limitations and state constraints as well as its degradation issues [97].

In this Section, an optimal management strategy is proposed referred to ESSs integration in grid-connected hybrid microgrids. The synthesis of the optimal solution is carried out in order to minimise the daily MG electricity costs under variable demands and dynamic prices. In particular, an optimal control problem formulation, which takes into account ESS charging/discharging inefficiencies and constraints, asymmetric real-time buying/selling prices, along with ESS degradation costs, is proposed. The effectiveness of the proposed approach is verified on a case study, which refers to a real microgrid locally supplied by two photovoltaic power plants.

2.5.1 Mathematical Modelling

Referring to the schematic representation of a grid-connected MG depicted in Fig. 2.26, it consists mainly of RES power plants, loads and storage systems. Consequently, its instantaneous power balance can be expressed as in (2.42) assuming i=1. In particular, in this case an on-site stationary storage systems is supposed to be in place, hence s being the power exchanged by the ESS within the MG. Additionally, the storage modelling follows the formulation already derived in Section 2.4 for the V2G storage by means of (2.46) through (2.51), provided j=1 and p_r=0.

2.5.1.1 ESS Degradation Cost Defintion

Among all the performance characteristics of a storage resource, the cycle life is one of the most important indexes that should be carefully considered. In fact, degradation issues are a crucial aspect of most state-of-the-art ESSs since their capacity decreases as a result of cycling. Consequently, the use of a storage system for price arbitrage could significantly affects the ESS lifetime, reducing its ability to store and deliver energy. In the definition of the OMS, a model of ESS degradation cost needs hence to be included in order to optimise MG costs without badly impairing the ESS cycle life. Considering the necessity of formulating an optimisation problem characterised by low computational complexity and suitable for on-line applications, the estimation of the ESS degradation cost is derived by means of the following simple model. In particular, the equivalent cost of storage degradation is defined in terms of energy capacity reduction as:

$$c_m = \frac{C_R \cdot d_c}{E_{EC}}. \tag{2.73}$$

In accordance with (2.73), the degradation cost (c_m, $€/kWh$) can be quantified as a function of the ESS replacement cost (C_R, $€/kWh$), energy capacity degradation due to cycling (d_c, $kWh/cycle$) and equivalent energy per full-cycle (E_{EC}, $kWh/cycle$). Whereas C_R corresponds to the kWh-cost of a new ESS, d_c is evaluated as a fractional capacity degradation, which represents the reduction of the ESS nominal energy by a finite fraction for each charging/discharging cycle. This reduction is computed by means of (2.74):

$$d_c = \frac{E_b - E_{EOL}}{N}, \tag{2.74}$$

where E_b is the storage rated energy, E_{EOL} indicates the energy capacity at the end of life (EOL), N being the number of cycle life. Generally, the cycle life refers to the capability of a battery to withstand a certain number of complete charge/discharge cycles at a given depth of discharge (DOD), commonly in the 80%-100% range. The nominal cycle life is evaluated as the maximum number of full-cycles N until the battery's end of life criteria is reached. Although partial cycling could have minor effects on performance degradation, the degree of validity of such an assertion is difficult to determine since the capacity fade is affected by other factors, namely current rates, operating temperatures and technology. In order to be as general as possible in the c_m formulation, the cycle life is, therefore, determined by proportionally adding the absolute value of the energy swings from partial and full cycling, divided by E_{EC}. Consequently, equivalent full cycles are obtained, allowing the estimation of the battery cycle life at the DOD cycling criteria provided by the producer.

2.5.2 Optimal ESS Management Strategy

The optimal ESS management proposed in this Section aims at minimising the MG energy costs over a given time horizon (T), accounting for specific energy purchasing and selling cost, as well as for ESS usage. In terms of optimisation problem, such an objective function can be formulated as follows:

$$\begin{aligned} J(s^*(t)) &= \ \mathbf{min} \ J(s(t)) \\ J(s(t)) &= \int_0^T f(s(t))\, dt \end{aligned} \tag{2.75}$$

subject to

$$\begin{cases} \dot{e}(t) = -(\alpha \cdot s(t) + \beta \cdot |s(t)|) = -(\alpha + \sigma_s \beta) \cdot s(t), \quad \sigma_s = sign(s(t)) & (2.76) \\ e(t_0) = e_0, \quad e(T) = e_T. & (2.77) \end{cases}$$

and constrained by (2.50) and (2.51). The cost function f is then defined as in (2.78).

$$f(t) = \begin{cases} c_p(t) \cdot g(t) + c_m(t) \cdot \dot{e}(t) & \text{for } g(t) \geq 0 \\ c_s(t) \cdot g(t) + c_m(t) \cdot \dot{e}(t) & \text{for } g(t) < 0 \end{cases} \tag{2.78}$$

where c_p and c_s represent the specific energy purchasing and selling cost respectively, whereas c_m accounts for the ESS degradation cost and hence for its usage. Therefore, based on (2.78), the cost function f can be better formulated by (2.79).

$$f(t) = \bar{c}(t) \cdot (1 + \sigma_g \cdot \gamma) \cdot g(t) + \big(c_m(t) \cdot \dot{e}(t)\big) \qquad \sigma_g = sign(g(t)), \tag{2.79}$$

the average energy cost $\bar{c}$ and γ being respectively defined as follows:

$$\bar{c} = \frac{1}{2} \cdot (c_p + c_s), \quad \gamma = \frac{c_p - c_s}{c_p + c_s}. \tag{2.80}$$

Then, by substituting (2.42) and (2.76) in (2.79), the relationship (2.81) is achieved:

$$f(t) = q(t) + m_f(t) \cdot s(t), \tag{2.81}$$

where:

$$q = -\bar{c} \cdot (1 + \sigma_g \cdot \gamma) \cdot r \tag{2.82}$$

$$m_f = -\bar{c} \cdot (1 + \sigma_g \cdot \gamma) + c_m \cdot (\alpha + \sigma_s \beta) \cdot \sigma_s. \tag{2.83}$$

The solution of such an optimal control problem is derived by applying the Euler-Lagrange approach and, in particular, the formulation in terms of Pontryagin's minimum principle presented in Section 2.4.2. As previously stated, the PMP requires the definition of the Hamiltonian function, which can be formulated as:

$$\begin{cases} \mathcal{H}(s(t)) = f(s(t)) + \lambda \cdot \dot{e}(t) = q(t) + m_h(t) \cdot s(t) & (2.84) \\ m_h = m_f - \lambda(\alpha + \sigma_s \beta). & (2.85) \end{cases}$$

In order to take into account the constraints on the state variable, the Lagrangian is accordingly introduced, by adding (2.53) into (2.84).

$$\begin{aligned} \mathcal{L}(s(t)) &= \mathcal{H}(s(t)) + \mu(t) \cdot \dot{k}(t) = \\ &= q(t) + [m_h(t) - \mu(t) \cdot (\alpha \cdot + \beta \cdot \sigma_s)(2e_j(t) - e_{max} - e_{min})] \cdot s(t), \end{aligned} \tag{2.86}$$

(2.55) holding. Then, on the basis of the Euler-Lagrange equations, the necessary optimality conditions assume the form reported in (2.56) through (2.58), provided that the objective function f is minimised when the control variables satisfy the minimum condition (2.59). Since (2.66)-(2.70) are still valid, $\mathcal{L} = \mathcal{H}\ \forall t \in [0, T]$. Referring hence to (2.84), it can be seen that $\mathcal{H}$ linearly varies with s, thus its minimisation occurs by either increasing or decreasing s to the maximum extent in accordance with the sign of m_h. This, in turn, depends on the sign of both s and g, as highlighted by (2.84) and (2.85). Consequently, four different conditions may occur depending on both σ_s and σ_g, as reported in Table 2.6. Proper s constraints are accordingly derived, representing the boundaries conditions to be applied in the

Table 2.6: *Control variables constraints from the proposed OMS formulation*

σ_s	σ_g	**r constraint**	**s constraint**
+1	+1	$r \leq 0$	$0 \leq s \leq \min(s_{max}, -r)$
+1	-1	$r \geq -s_{max}$	$\max(0, -r) \leq s \leq s_{max}$
-1	+1	$r \leq -s_{min}$	$s_{min} \leq s \leq \min(-r, 0)$
-1	-1	$r \geq 0$	$\max(s_{min}, -r) \leq s \leq 0$

synthesis of the optimal control s^* profile.

In addition, handling the state constraints (2.51) leads the solution of the optimal control problem (2.75) to consist of a number of constrained and unconstrained arcs. In fact, still referring to Section 2.4.2, a constrained interval requires that s is held at zero once either maximum or minimum ESS energy level is reached. Then, considering that $\mathcal{H}$ does not depend on e directly, it can be stated that λ is piecewise constant over T. A backward strategy can be finally implemented in order to find the sequence of sub-intervals as well as active state and control constraints, which gives the optimal solution to the presented problem. Then, the optimal pairs (s^* and e^*), along with the adjoint function can be derived such that all the necessary conditions of optimality are satisfied for each time-interval.

2.5.3 Case of Study

The proposed ESS optimal scheduling approach is validated referring to a case of study, which can be schematically represented by the MG already shown in Fig. 2.26. The reference MG is presently installed in a building belonging to the Technology Park of Sardinia (Italy) which hosts offices and laboratories. The MG power peak demand is about 15 kW and its own electricity production system is constituted of two PV power plants based on traditional flat-plate silicon and High Concentrator PV (HCPV) technology. The HCPV system is a 6.2 kWp Soitec Demo plant, made up of 90 modules and installed on a high precision dual-axis solar tracker. The traditional PV system is a 18.71 kWp integrated silicon monocrystalline and amorphous plant, installed on the rooftop of the building. The deployment of the PV power plants aims at reducing the MG dependency from the main electricity grid and increasing the energy self-consumption. However, the presence of the HCPV plant introduces challenging operating conditions for the energy management of the MG due to the high variability of its power production, as explained in Chapter 1. The installation of an ESS is hence assessed in order to make the HCPV system production dispatchable and programmable, enabling its integration in the MG.

For this purpose, a Sodium-Nickel Chloride battery (SNB) characterized by a rated capacity of 23.5 kWh (E_b) is selected. The battery SOC is additionally bounded within a range of 10%-95% in order to increase the battery lifetime, as generally occurs in practical applications. Moreover, due to the differences between the SNB charging/discharging electrical and thermal behaviours, asymmetrical power limitations are considered by taking into account maximum discharging and charging

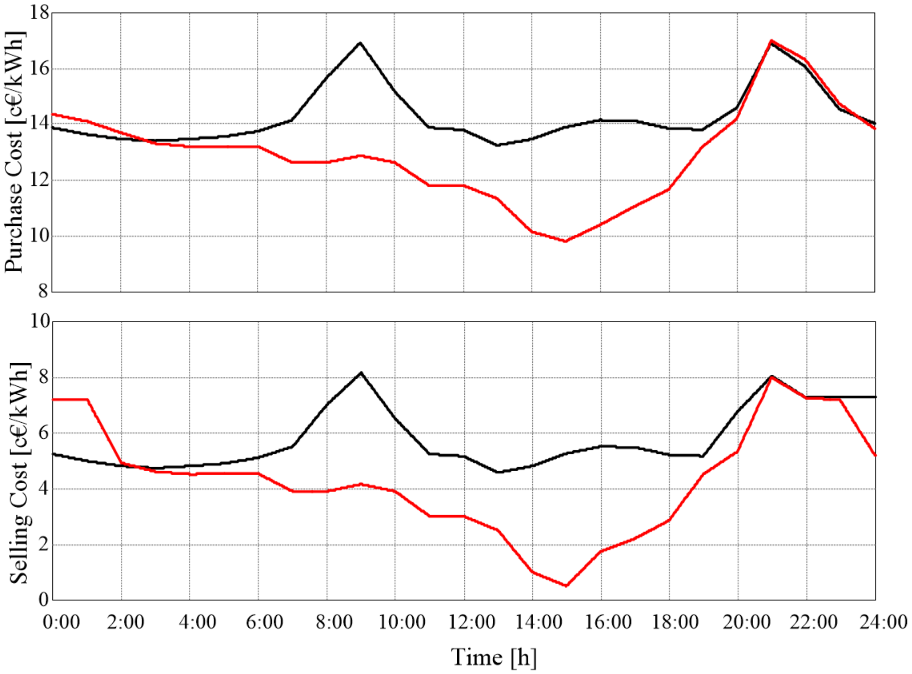

Figure 2.27: *Profiles of the purchasing cost c_p (on the top) and selling price c_s (on the bottom) for a working (black) and a weekend day (red).*

powers of 8 kW (s_{max}) and 6.25 kW ($-s_{min}$) respectively. Finally, the overall charging and discharging efficiencies are both assumed equal to 90%. In order to estimate the battery degradation cost, an analysis of the SNB capacity degradation issues has been carried out. To this end, [98] identifies a large cycling window as the dominant factor causing the battery capacity reduction. Consequently, the simple model of (2.73) and (2.74) can be effectively used in order to estimate the battery degradation cost with a good approximation. In particular, by implementing the number of life cycles and the replacement cost provided by the battery manufacturer, c_m is assumed equal to 0.01 €/kWh.

As far as the energy prices are concerned, the Italian electricity market is taken into account [99]; particularly, the Unique National energy Price (PUN) and the Sardinian Zonal Price (P_z) are used in order to define the specific energy purchasing cost c_p and selling price c_s. In fact, the retail price c_p is typically based on the PUN augmented by transmission/distribution fees and other electricity system charges, whereas the selling price c_s could be determined in accordance with the hourly zone price (P_z), since the MG can obtain economical compensation for the amount of electricity injected into the grid [100]. Different c_p and c_s profiles are then introduced

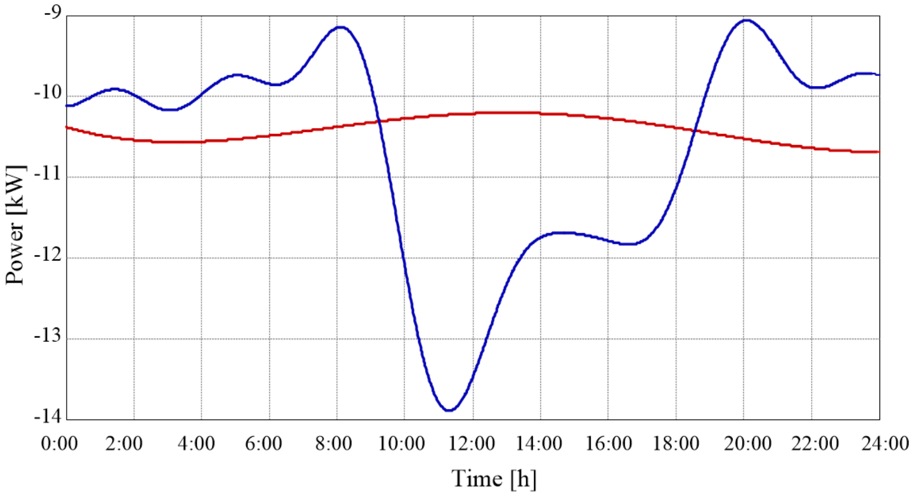

Figure 2.28: *Typical electricity demand evolution in a working day (blue) and a weekend day (red)*

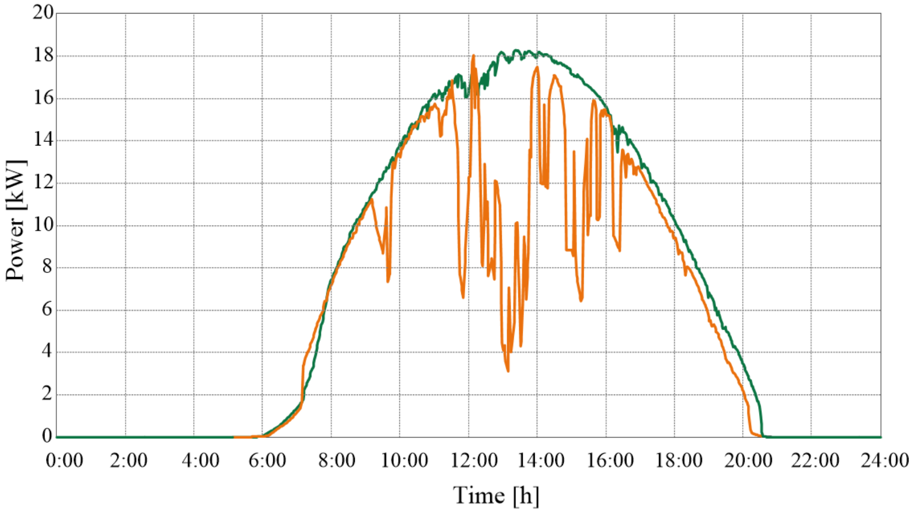

Figure 2.29: *RES production in a partially cloudy day (Case A, orange) and in a sunny day (Case B, green)*

in order to account for trends of purchase and selling prices during working and weekend days, as shown in Fig. 2.27. They represent daily reference time evolution of energy prices evaluated by means of a statistical analysis of the Italian electricity market [99]. Furthermore, it is worth of observing that the purchase costs and selling prices are fully asymmetrical, c_p being much greater than c_s: this condition is in fact typical of RES policies intended to promote the local self-consumption.

Regarding MG load and RES power profiles, several scenarios have been considered, as highlighted in Fig. 2.28 and Fig. 2.29, respectively. The profiles of Fig. 2.28 synthesize different possible MG load configurations recorded during working and non-working days. In particular, during a working day, the load trend features two consumption peaks in the morning and in the late afternoon, which are the time periods characterized by most of the laboratory activities. Moreover, the base load can be clearly identified, representing the MG standby condition typical of non-working hours and weekend days.

Finally, considering the necessity of demonstrating the feasibility of the proposed optimal ESS management strategy under different MG operating conditions, the RES production effects are taking into account referring to two weather scenarios. These are chosen in order to compare different HCPV production profiles which mainly influence the total MG power generation (P_{RES}). In particular, as can be noticed in Fig. 2.29, *Case A* refers to a partially cloudy day, whereas *Case B* considers a sunny day, resulting in a MG generation characterized by the typical production trend of PV systems. In both cases, the cost and load profiles are those already shown in Figs. 2.28 and 2.27 and previously defined, allowing the simultaneous evaluation of MG cost savings during working and weekend days.

2.5.4 Simulations

In order to evaluate the effectiveness of the proposed OMS, a simulation study is carried out by means of the Matlab Software Package. The proposed optimal management strategy is implemented for the case of study over a time horizon of 24 h, with a 1-minute time-resolution. The results obtained in both *Case A* and *Case B* are also compared to the baseline case, i.e. the MG without any ESS. For the sake of optimality, it is assumed that the final ESS energy level must be equal to the initial in order to preserve a defined reference state at the end of the control horizon. In the following simulation, the condition (2.87) is accordingly applied.

$$e_0 = e_T = 0.5 \cdot E_b \tag{2.87}$$

Referring to the *Case A*, the optimal battery power and corresponding energy evolutions are reported in Fig. 2.30. These outcomes can be better analysed also considering the daily trends of the power exchanged between the MG and the main grid shown in Fig. 2.31. Referring to Fig. 2.27, it is clear that the optimal ESS control strategy avoids the purchase of energy when c_p is high, by discharging the

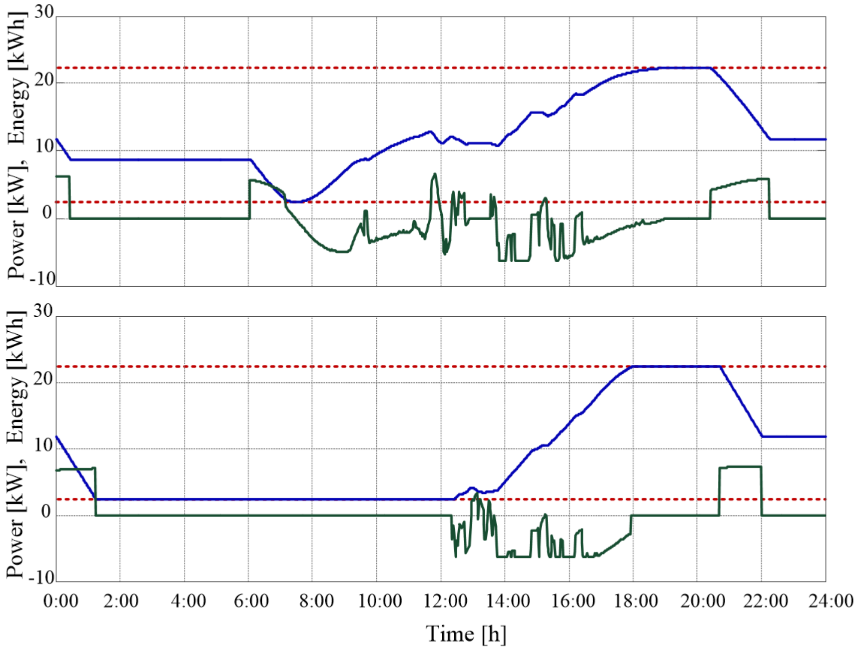

Figure 2.30: *Optimal daily profiles of stored energy in the battery (blue) and power (green) in Case A: working day (on the top) and weekend day (on the bottom).*

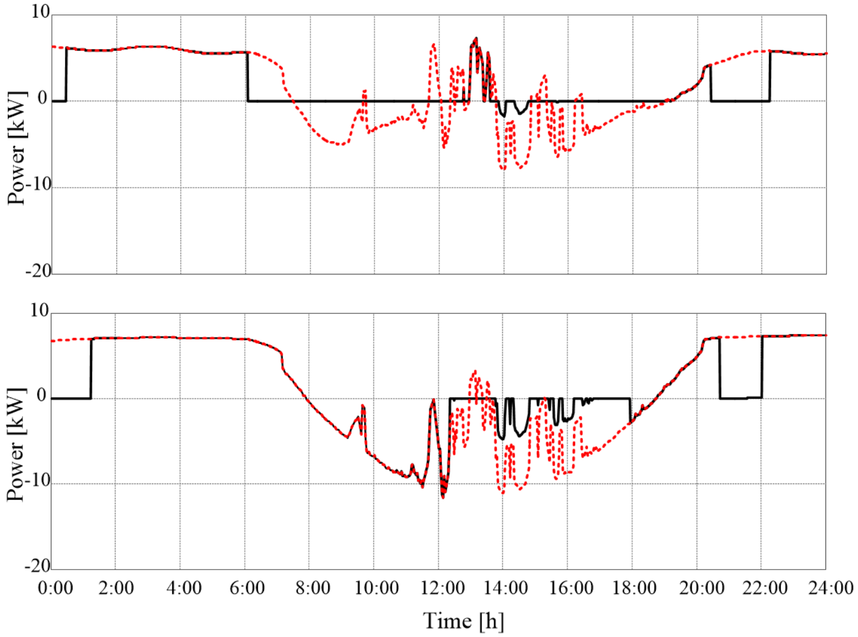

Figure 2.31: *Daily evolutions of the power exchanged between the MG and the main grid in Case A with (black) and without the ESS (red): working day (on the top) and weekend day (on the bottom).*

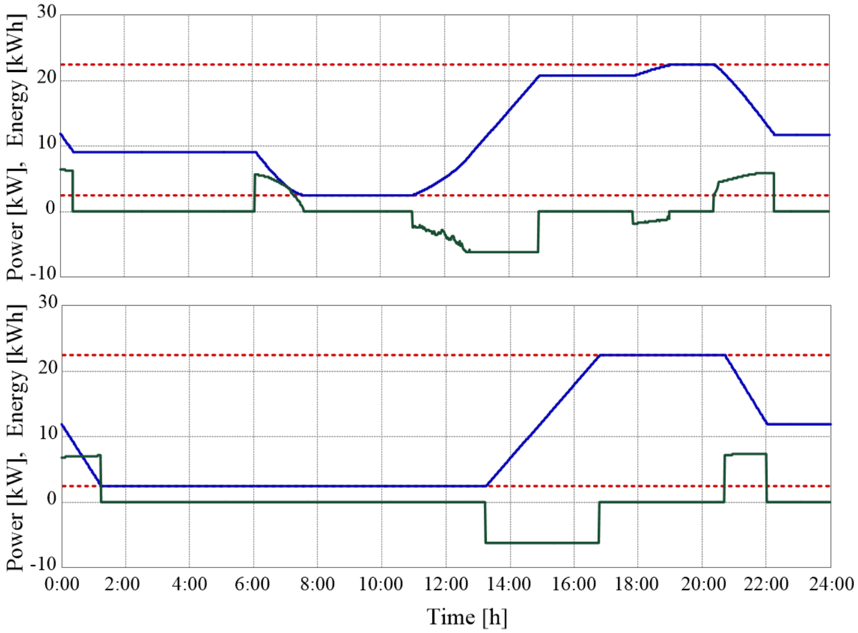

Figure 2.32: *Optimal daily profiles of stored energy in the battery (blue) and power (green) in Case B: working day (on the top) and weekend day (on the bottom).*

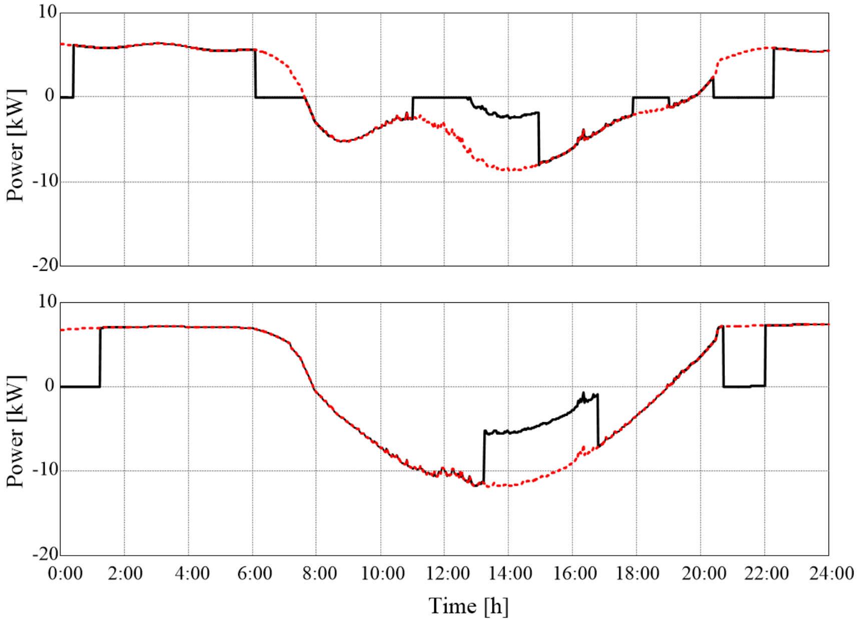

Figure 2.33: *Daily evolutions of the power exchanged between the MG and the main grid in Case B with (black) and without the ESS (red): working day (on the top) and weekend day (on the bottom).*

Table 2.7: *Cost saving results*

	Working day		**Weekend day**	
	Cost savings	**Total cost w/o ESS**	**Cost savings**	**Total cost w/o ESS**
Case A [**€**]	1.16	8.24	2.07	10.52
Case B [**€**]	1.26	5.80	2.09	9.53

battery if the load could not be fully covered by the RES production. Consequently, some energy is purchased only when the costs are expected to be the lowest, which happens in the time-periods 1:00-8:00 and 13:00-14:00. Furthermore, in the weekend days the MG has also the possibility to sell most of the RES generation due to the reduced load. In this case, the injection of energy into the main grid is managed in order to maximise the profit. In fact, the energy is mainly sold during 8:00-12:00 time-window and after 18:00. Accordingly, from 12:00 to 18:00 the battery is recharged by absorbing the most of the surplus of the energy production.

The same simulation studies carried out in *Case A* are reported for *Case B* in Figs. 2.32 and 2.33. The *Case B* reflects a typical sunny day with a high amount of RES energy surplus. This is partially used to recharge the battery when the selling prices are low, whereas the battery is discharged in order to cover the load demand when purchase costs are estimated to be high.

The cost savings achieved in both *Case A* and *Case B* are summed up in Table 2.7. Referring to *Case A* at first, the implemented ESS management substantially reduces the MG electricity cost by 14% (working day) and 19.7% (weekend day) in comparison to the baseline case. Similarly, in *Case B*, the proposed optimal strategy allows significant cost savings with respect to the MG without ESS, reducing by about 22% the value of the objective function in both working and weekend days. Finally, it is interesting to note that the power profiles of the battery are mostly influenced by the HCPV production dynamics, as easy detectable in Fig. 2.30. Such HCPV power fluctuations can be also clearly observed in the daily trend of power exchanged between the main grid and the MG without ESS. However, when the ESS is considered, the MG power profile is smoothed, as can be observed in Fig. 2.31. Therefore, the installation and proper management of the battery storage enables another important benefit besides the maximisation of the MG cost savings, that is the compensation of the HCPV power fluctuations.

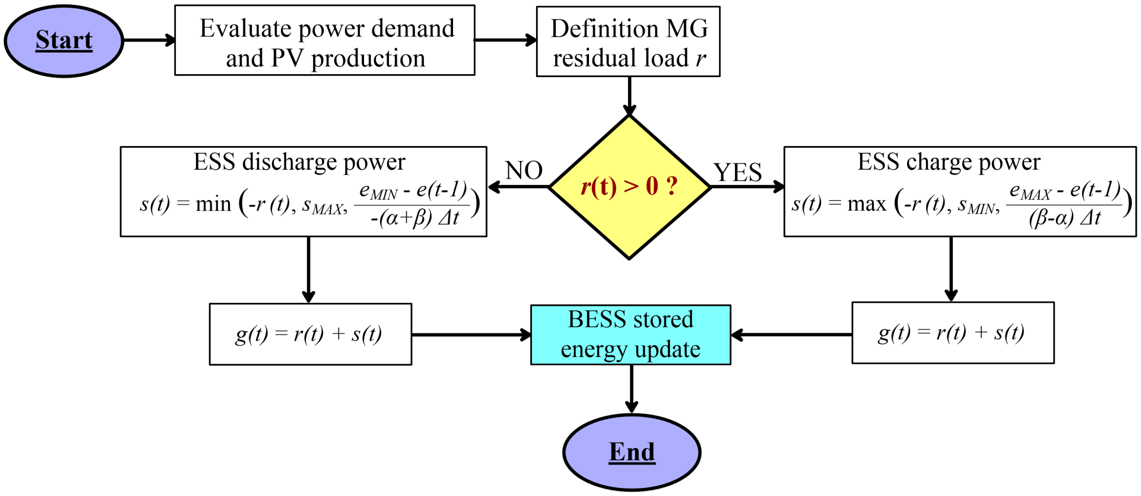

Figure 2.34: *Rule-based strategy for the benchmark MG.*

2.5.4.1 OMS VS RBS: a comparative analysis

In order to validate the behaviour of the proposed optimal ESS management strategy, a non-optimised rule-based algorithm is developed and implemented for the benchmark MG. The aim is making a comparison between both solutions, and demonstrates the superior behaviour of the optimal control strategy compared to the non-optimised one. The developed RBS is based on the flowchart presented in Fig. 2.34. Essentially, the management algorithm starts from the evaluation of load demand and PV units production. Such quantities are then used to compute the MG residual load in accordance with (2.44). The identification of a local electricity surplus or deficit event defines the specific control action by resorting to both the ESS and main grid in order to respect the MG electricity balance equation (2.42). It is worth of noting that the storage's SOC at the end of the time-period is handled by the RBS in order to reach the same value measured at the beginning of the control horizon, respecting (2.87). In this way the results from the two ESS management strategies can be correctly compared.

Referring to the non-optimised RBS, the battery power and energy profiles are reported in Fig. 2.35. These are depicted along with the results from the OMS strategy in order to facilitate their comparison. By analysing the figures, the differences in the ESS management between the two strategies can be easily detected. In fact, it's worth noting that the RBS defines the ESS power set-points on the base of the sole residual load, regardless of the purchase and selling prices. Clearly, the actual charge/discharge battery power is then limited by the constraints imposed on its

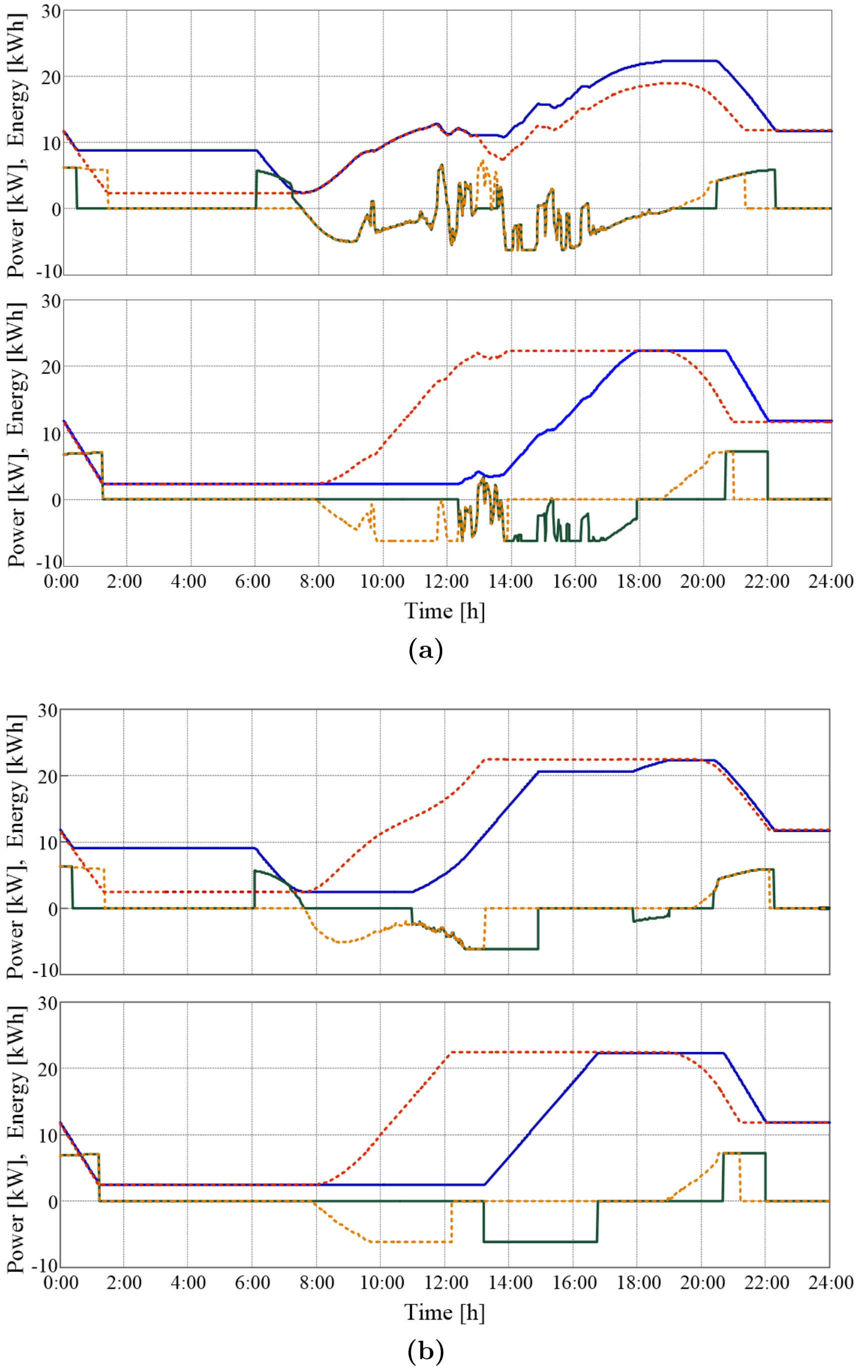

Figure 2.35: *Comparison between daily profiles of ESS stored energy and power for the OMS strategy (Energy: blue; Power: green) and for the RBS algorithm (Energy: dashed red; Power: dashed orange): working day (on the top) and weekend day (on the bottom). (a) Case A. (b) Case B.*

Table 2.8: *MG cost savings: comparison between RBS and OMS results*

	Cost savings			
	Working day		**Weekend day**	
	RBS	**OMS**	**RBS**	**OMS**
Case A [€]	1.02	1.16	1.57	2.07
Case B [€]	0.95	1.26	1.51	2.09

power and energy capacity, determining consequently the power effectively traded by the MG with the main grid. As far as the objective function is concerned, the numerical results reported in Tab. 2.8 show the greater cost savings obtained by implementing the OMS algorithm. In fact, the optimal strategy allows a reduction of the MG electricity cost by 6%-7% in the week-ends, and by 2%-6% during working days, depending on the weather conditions as well.

In conclusion, the simulation results have highlighted that the proposed optimal ESS scheduling strategy can be effectively implemented in order to minimise the MG daily electricity costs, considering real-time prices and variable MG generation. In particular, the ESS optimal management allows the achievement of significant daily cost savings, respect to both the baseline case without any ESS and a non-optimised rule-based management strategy.

2.6 Conclusions

In this Chapter several algorithms and management strategies for the integration of ESSs in different smart grid architectures have been proposed and analysed. In particular, both rule-based and optimal management strategies have been presented, showing their effectiveness and potentialities. However, it has been demonstrated that the best solutions, design or operating conditions can be ensured only by the optimal control approach. In this context, the optimal input profiles are obtained using suitable models that predict the system behaviour. Because of the presence of uncertainty, optimisation requires accurate modelling in order to actually reach optimality. In fact, a simple model could lead to significant system-model mismatching, being often insufficient to optimise the objective function in the real application. In the analysed cases of study, one of the most critical components is the ESS, which could need a more accurate modelling than that presented in the previous sections, depending on the particular application. Specifically, in dynamic optimisation problems a more complex mathematical formulation is required in order to deal with dynamic and non-linear behaviours of battery-based storage systems. Additionally, since electrochemical ESSs group a number of technologies, an "all-purpose" model can hardly represent the peculiarities of each battery system. Therefore, based on prior knowledge and measurements from real BESS, *ad-hoc* battery models need to be developed and validated to ensure that their complexity and accuracy will be adequate for their final implementation in the optimal control framework.

In the next Chapter, the issues in modelling battery technologies are addressed, particularly referring to Lithium-Iron Phosphate and Sodium-Nickel Chloride systems.

Chapter 3

Modelling of Battery Technologies for Smart Electric Systems

3.1 Introduction

The present environmental and energy policies are steering a transformation in both the power system and the automotive sector, speeding up the transition from fossil fuels to sustainable technologies. On one hand, this has led to a rapid diffusion of renewable energy resources, which are contributing to change the structure of the electricity network from a centralised to a distributed form. Wind and PV power fluctuations as well as load variations and sudden voltage drops are requiring more flexibility and intelligence in the power systems management, forcing towards the adoption of the smart grid paradigm. Energy storage systems have thus emerged as crucial elements in the integration of renewable energy into the grid: they can in fact compensate for the stochastic nature and sudden lacks of RES production, while providing power smoothing and voltage regulation. In particular, electrochemical batteries are efficient and versatile ESS technologies and, therefore, they are likely to be widely adopted in the novel smart grid configuration.

On the other hand, more sustainable transportation systems are also demanded, leading to the introduction of drive-train electrification into the automotive sector. Presently, the plug-in hybrid electric vehicle (PHEV) is considered the first step in a future prospective of a full electric mobility exemplified by the battery electric vehicle (BEV). In these systems, besides internal combustion engine and electric motors, a battery storage is used to power the vehicle, representing the key component for enhancing the electric mobility and for the integration between the vehicular field and the power grid. Batteries have thus emerged as the most promising energy storage device, attracting a significant amount of attention, as also pointed out by considerable research efforts spent on this topic [25, 27, 30, 33, 34, 93, 101–103].

As the diffusion of smart grids and EVs is worldwide fostered, greater level of accuracy in modelling the energy and dynamic performance of storages is needed. Particularly, accurate battery models are required both in the design phase, in order to validate the technology choice and sizing, and in real-time operation to estimate as precisely as possible the actual battery response to power set-points. Accurate models are also needed in electric vehicles control algorithms and battery management systems (BMSs) for the estimation of battery-pack state-of-charge, voltage evolution and available power. Therefore, accurate battery modelling is essential to ensure adequate performance and precision for the EMS in both smart grid and EVs applications. So far, a variety of battery models have been proposed with different degrees of complexity and accuracy, being basically grouped into three classes: electrochemical, mathematical and electrical [104–106]. The former provides high accurate modelling of the electrochemical reactions inside the battery, its use being mandatory in analysis of physical energy conversion processes oriented to batteries design and optimisation. However, this type of modelling requires a high computational effort to solve detailed partial differential equations, which make difficult its implementation for real-time applications. On the contrary, in the mathematical modelling approach, available experimental current-voltage characteristics are used to derive a run-time-based model by applying statistical modelling or curve fitting approaches [107]. Nevertheless, these models are not able to deal with the battery dynamics, being suitable only for static applications. Finally, electrical models describe batteries as electric circuits with parameters representing some physical phenomena of the battery. This approach is widely implemented for system-level applications because requires low computational time and memory, is simple to be used and analysed and provides accurate dynamic behaviour of the battery. Such a type of models is additionally divided into two major categories: impedance-based and Thévenin-based models. The impedance-based models are derived from the frequency domain analysis of the current-voltage behaviour of the battery and their parameters are extracted based on electrochemical impedance spectroscopy. Contrariwise, the Thévenin-based model is constituted of combinations of resistors, capacitors, and voltage sources, which are typically obtained from current-voltage experiments in time domain. Such circuit-

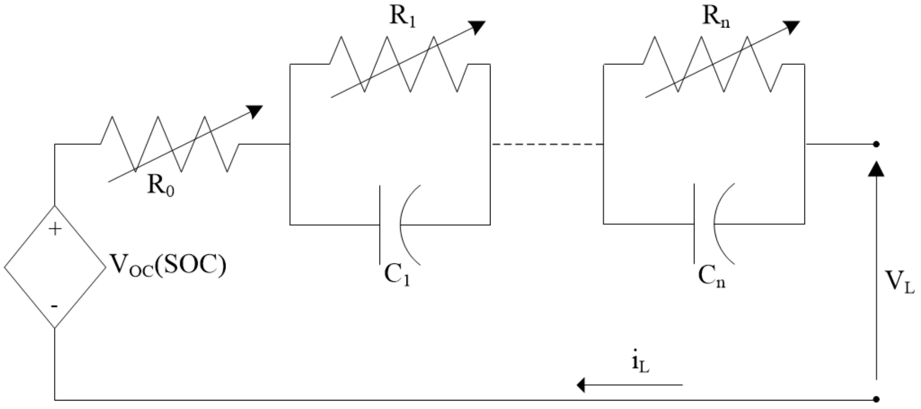

Figure 3.1: *Thévenin-based battery model.*

based models are therefore the most suitable for runtime estimations and for BMS implementation, offering different degrees of accuracy depending on the complexity of the implemented circuit.

The definition of an equivalent circuit-model is usually based on the general Thévenin structure reported in Fig. 3.1. The circuit represents the load current and the battery terminal voltage relationship, where *RC* parallel circuits are used to model the battery relaxation and dynamic effects. All resistances and capacitances are usually non-linear functions of the SOC, current rate and temperature, whereas the battery open circuit voltage (OCV) shows a strong dependence from the SOC and the current direction. The number of series connected *RC* circuits improves the model accuracy, but simultaneously increases the execution time. Two series *RC* parallel circuits are usually considered the best most appropriate compromise in battery modelling [102], however, in several studies, using one *RC* pair has shown accurate enough performance [107].

In this Chapter, the issues in battery modelling are addressed, particularly referring to Lithium-Iron Phosphate and Sodium-Nickel Chloride systems. In the first case, a simplified and unified model of lithium batteries is proposed for the accurate prediction of charging processes evolution in EV applications. In fact, the model is developed in order to be simple and accurate enough to allow its implementation in off-board chargers. The aim is on-line forecasting EV charging profiles at various C-rates and subsequently controlling the EV charging process for smart grid applications. Finally, in order to test different battery technologies and with the aim of verifying the actual performance of new storage candidates for smart and microgrid applications, a dynamic electrical modelling is presented for a high tem-

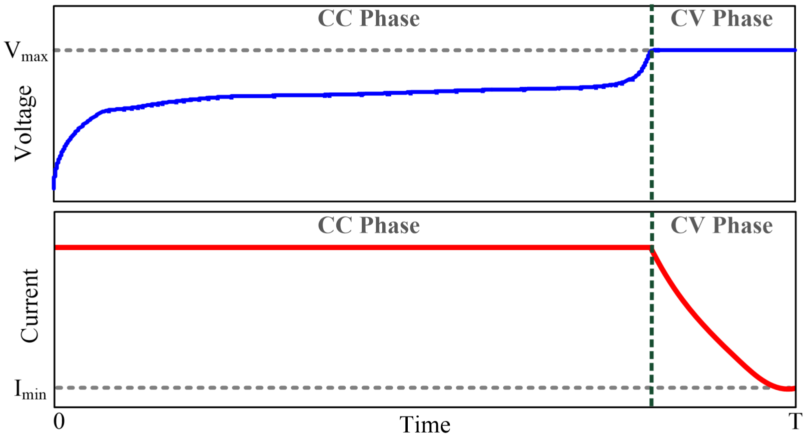

Figure 3.2: *CC-CV charging strategy.*

perature Sodium-Nickel Chloride battery. The aim is the development of an accurate model easily implementable in microgrids EMS and, hence, suitable for their on-line management and control.

3.2 A Lithium-Ion Battery Model for smart EVs

Lithium-ion (Li-ion) batteries offer the best trade-off between power-energy density and costs for EV applications and, therefore, are presently the most used power source for electrified mobility. Moreover, their capability to withstand high current rates enables the EV to be fast recharged, addressing drivers range anxiety and minimise filling duration. In this context, Level 3 fast chargers offer the possibility of charging EVs in less than 1 hour, operating like a filling gas station [108]. High current rates are consequently applied, within the limitations imposed by storage technologies. Such boundaries can differ based on chemistries and structures of distinct Li-Ion batteries, requiring suitable models to be included in off-board *general-purpose* charging devices.

Lithium-based batteries are usually recharged by applying a constant current-constant voltage (CC-CV) strategy. Such a strategy is composed of two phases, as shown in Fig. 3.2. In the first stage the battery is charged at a constant current until the voltage reaches its maximum charging value. In the second phase, a constant voltage is imposed until the current falls below a given value. Depending on the cathode chemistry of the lithium-ion battery and on the current rate, the SOC at the end of the CC charge step assumes values between 70% and 90%. In addition,

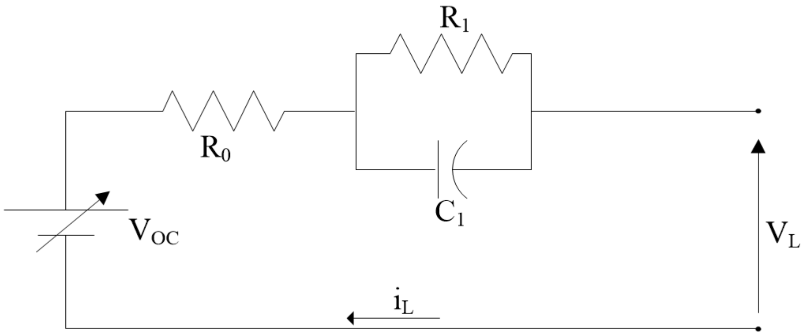

Figure 3.3: *Equivalent circuit model of a lithium-ion battery.*

the duration of this phase is related to the applied charging current, lasting about 1h at $1\mathcal{C}$ rate. Therefore the application of the CC method seems to be suitable for fast charging applications of electric vehicles. In fact, Level 3 off-board chargers typically operate with power levels between 50 and 100 kW which could entail a minimum charge time of 15 minutes, guaranteeing a 50-80% SOC [108].

The adoption and the massive diffusion of fast charging method in EVs filling stations require a strategy for the management of charging processes at high current rates (greater than $1\mathcal{C}$) that ought to take into consideration an universal, simple and efficient charging model suitable for Li-ion batteries of different chemistries and capacities. This task demands an off-board charging system capable to on-line estimate both the charging time and the EV energy demand.

In this Section, a simplified, unified and normalised model of lithium batteries is presented. The proposed estimation algorithm aims at determining the duration of charge processes and battery voltage profiles at different charging rates, providing the sole information on the battery capacity, terminal voltage and SOC. In particular, the adopted electrical modelling is experimentally validated on a Lithium-Iron Phosphate (LFP) battery. Finally, the worth of the proposed approach is highlighted by a possible application for the smart management of EV charging process.

3.2.1 Battery Modelling Methodology

The adopted model, reported in Fig. 3.3, is based on the assumptions that all electro-thermal processes are uniform and no variations of concentration and potentials occur throughout the whole battery [109]. Consequently, the battery can be modelled by lumped circuital components, extracted from experimental data. In particular, the model of Fig. 3.3 is made up of a voltage source V_{OC}, a terminal voltage V_L, an internal DC resistance R_0 and a RC parallel network, the latter accounting for the effects of the transient response. The voltage source V_{OC} represents the battery open circuit voltage (OCV) which varies with the stored charge (SC) of the battery. As far as the considered electrical battery model and its components are concerned, the following equations can be used to describe the relationships between the terminal voltage, the load current (i_L), the open circuit voltage and the cumulative charge:

$$V_{OC}(t) = V_L(t) - R_{int} \cdot i_L \tag{3.1}$$

$$SC(t) = SC(t-1) + \int_t i_L \, dt \tag{3.2}$$

$$V_L(t) = \sum_{k=0}^{n} \left(\alpha_k \, SC^k\right) + \beta \, e^{c\,SC} \, . \tag{3.3}$$

The OCV is expressed starting from the terminal voltage and subtracting the potential losses due to chemical and electrical internal resistive phenomena R_{int} (modelled by the resistances R_0 and R_1). The terminal potential V_L, as a function of the stored charge, is determined fitting the experimental results using the nth-order function reported in (3.3), where α_k, β, c represent the coefficients of the polynomial and exponential, respectively.

The procedure used to model the charging process of lithium batteries is based on the method proposed in [103]. This essentially consists of five steps, as follows:

1. a set of charging curves of a Lithium battery is acquired at different constant $\mathcal{C}$-rates, showing the dependence of the terminal voltage from the time and consequently from the stored charge, as given by (3.2)-(3.3);

2. a time normalization is performed in order to compare different charging profiles on similar time scale;

3. the DC resistance R_0 is determined and the voltage rise due to it has been removed from each charging curve, obtaining normalised and overlapped charging profiles;

4. the normalised profile is fitted by using the function reported in (3.4) and minimising the error by means of the least square algorithm;

5. in the last step, the mathematical model is obtained by applying the Laplace transformation to the time derivative of (3.4).

$$V_L(t) = \alpha_0 + \alpha_1 t + \beta e^{ct} \tag{3.4}$$

In [103], the method was applied using experimental data of a generic lithium battery, presumably based on manganese or cobalt cathode. Constant charging currents of $0.1\mathcal{C}$, $0.2\mathcal{C}$, $0.5\mathcal{C}$ and $1\mathcal{C}$ acquired at 25°C were used to carry out the series of charging tests. The model was subsequently validated by the comparison between experimental results and simulations for two lithium batteries of different capacities, verifying that the fitted model can accurately represent the charging process of a lithium-based battery. Nevertheless, the claimed generalisation of this model ought to be verified for a larger number of lithium battery chemistries. In particular, considering the increasing popularity of LFP batteries for EVs applications and the technology peculiarities in terms of voltage curve flatness, the method proposed by [103] is here applied and its accuracy evaluated for a LFP battery. Moreover, should this model be implemented into off-board fast charging systems, experimental data of charging test at high current rates are requested to be included in the fitting procedure. Consequently, charging profiles at $2\mathcal{C}$ and $3\mathcal{C}$ are considered in the parameters identification and battery model development, as discussed in the following Sections.

3.2.2 LFP Charging Model

3.2.2.1 Test-bench and battery characterisation

The tested LFP battery is made up of 4 series-connected cells by the company A123Systems and is characterized by a nominal voltage of 13.2 V, a 2.3 Ah capacity, a fast charge current of $4\mathcal{C}$, and a maximum discharge current equal to 70 A and 120 A in continuous and pulse mode, respectively. The battery was tested using the universal charger/discharger NextGeneration 7.36-8 by Schulze Elektronik, which allows to charge and discharge a battery pack at different current rates. Several charge and discharge tests were carried out in order to evaluate the battery performances and voltage profiles at various operating conditions [30]. The collected data are here used in order to develop a mathematical model of LFP batteries and subsequently for its validation.

3.2.2.2 Model Parameters Identification Process

In this Section, a LFP dynamic charging model is presented, based on the 5-steps procedure described in Section 3.2.1. As previously reported, the first step is to consider a set of charging tests performed at different $\mathcal{C}$-rates. Although several experimental data are available for the considered battery, on first approximation, only the time evolution of the battery voltage terminal at $0.239\mathcal{C}$, $0.5\mathcal{C}$ and $1\mathcal{C}$ rates have taken into account. As shown in Fig. 3.4a, a time scaling is required in order to compare the charging curves and obtain a single profile which can describe the battery dynamics at different charging currents. To accomplish this task, the profiles are normalised in the time axis, considering the rate factors and the measured charging durations. Fig. 3.4b shows the charging profiles after time normalisation. In spite of their similarity, a slight difference appears between the voltage curves, drawn the attention to the effect of the internal DC resistance (R_0). This parameter cab be obtained from the difference between charging profiles, $\Delta V_L(t)$, applying (3.5)-(3.7). In (3.7), $\Delta V_{L_j}^{mean}$ indicates the mean value of the difference between the *j-th* charging profile and the reference one, the latter corresponding to experimental data for $0.239\mathcal{C}$ charge rate. By applying the Ohm's law, the voltage rise (V_{Rj}) can be easily calculated by (3.8).

$$\begin{cases} \Delta i_{L_j} = i_{L_j} - i_{L_{0.239\mathcal{C}}} & (3.5) \\ \Delta V_{L_j}(t) = V_{L_j}(t) - V_{L_{0.239\mathcal{C}}}(t) & (3.6) \\ R_0 = \dfrac{1}{n}\displaystyle\sum_{j=1}^{n}\left(\frac{\Delta\, V_{L_j}^{mean}}{\Delta i_{L_j}}\right) & (3.7) \\ V_{Rj} = R \cdot i_{L_j}. & (3.8) \end{cases}$$

An almost perfect overlapping can be finally achieved by the removal of the effect due to the DC resistance, as illustrated in Fig. 3.4c. Such a unique profile has been subsequently considered in order to identify the electrical parameters of the proposed equivalent circuit model and estimate the battery dynamics related to the charging process.The mathematical model reported in (3.4) has been used to fit the normalised profile. In particular, the normalised terminal voltage modelled by (3.4) represents the battery dynamic response to a unit step of current at $1\mathcal{C}$. Based on these considerations, the application of the Laplace transformation to the time derivative of (3.4) allows the determination of the transfer function $H(s)$ reported in (3.9):

$$H(s) = \frac{\alpha_1}{s} + \frac{\beta c}{s + c}. \tag{3.9}$$

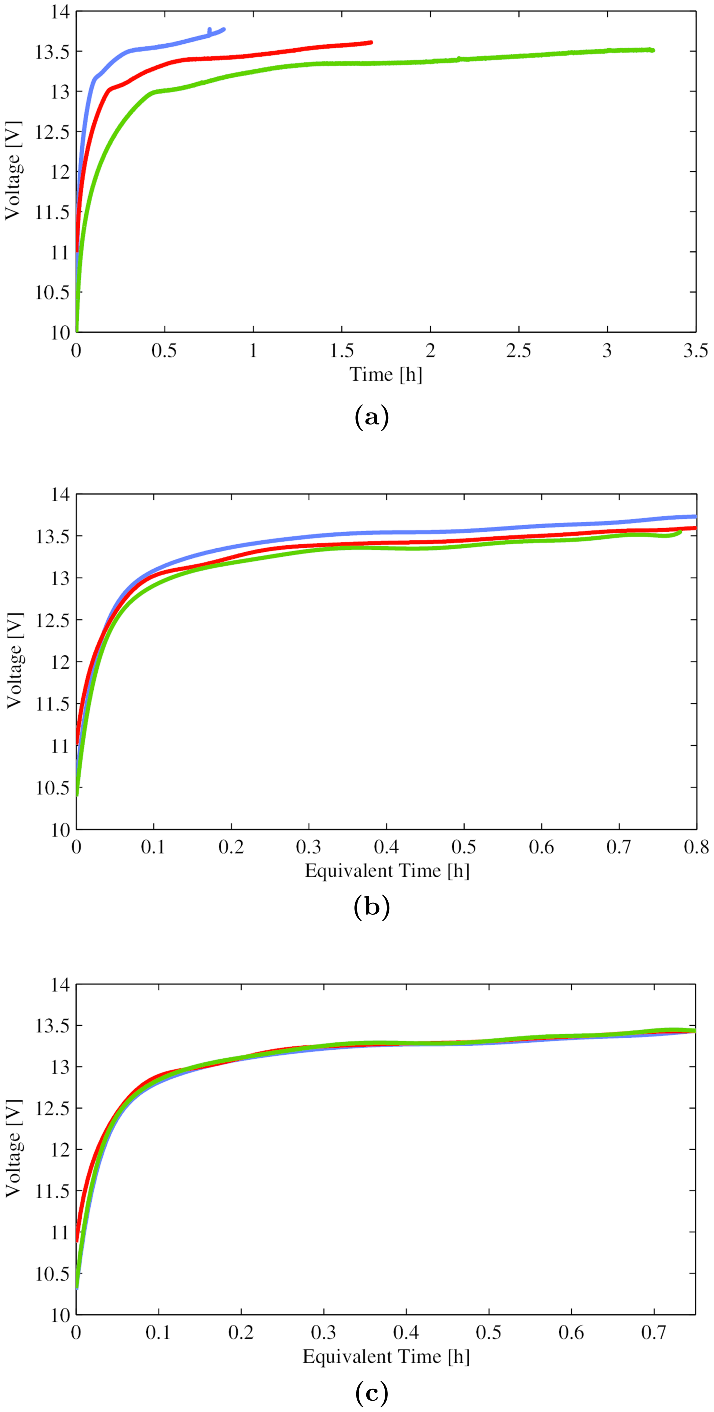

Figure 3.4: *LFP charging profiles at 0.239C (green), 0.5C (red) and 1C (blue). (a) Experimental data. (b) Time normalisation. (c) Time normalisation and DC resistance compensation.*

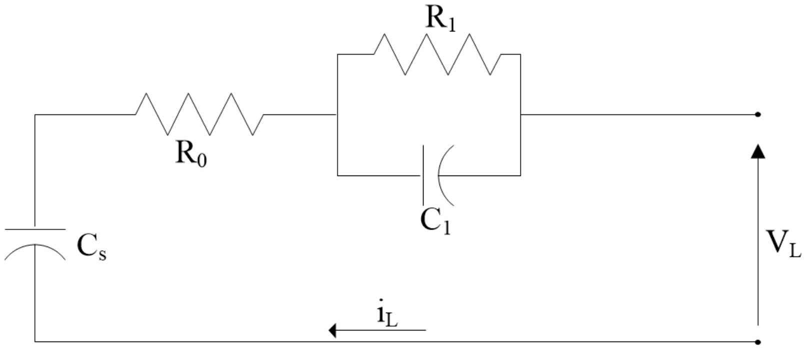

Figure 3.5: *Complete equivalent circuit model for a lithium battery.*

By adding the DC resistance of the battery, estimated by (3.7), the transfer function of the complete equivalent model assumes the following form:

$$H_B(s) = \frac{\alpha_1}{s} + \frac{\beta\, c}{s + c} + R_0 \cdot \mathcal{C}, \tag{3.10}$$

being $\mathcal{C}$ the capacity of the battery. Eq. (3.10) can be decomposed into three blocks representing: a storage element, a transient element and a resistive component. The storage element is given by the first addend of (3.10) and can be represented by a capacitor C_s, whose capacitance is obtained by applying (3.11). The second addend identifies the transfer function of the transient block (3.12), which can be modelled by a first order circuit made up of the resistor R_1 and the capacitor C_1 evaluated as in (3.13). Finally, from the analysis of the transfer function (3.10) and of its elemental blocks, the complete equivalent circuit model of the battery can be derived, as shown in Fig. 3.5. It's worth noting that the variable DC voltage source V_{OC} of the electrical circuit reported in Fig. 3.3 is replaced by the storage element C_s.

$$H_B(s) = \frac{\alpha_1}{s}; \quad C_s = \frac{3600\mathcal{C}}{\alpha_1} \tag{3.11}$$

$$H_t(s) = \frac{\beta c}{s + c} \longrightarrow H_{RC}(s) = \frac{R_1}{R_1 C_1 s + 1} \tag{3.12}$$

$$R_1 = \frac{\beta}{i_L}; \qquad C_1 = \frac{3600\mathcal{C}}{c R_1 i_L} \longrightarrow C_1 = \frac{3600\mathcal{C}}{c\beta} \tag{3.13}$$

By implementing this method in the Matlab-Simulink environment, the electric parameters of the LFP battery model can be identified at each charging rate, the

Table 3.1: *Electrical parameters of the battery model*

R_0 [Ω]	C_s [F]	C_1 [F]	R_1 [Ω]		
			1$\mathcal{C}$	0.5$\mathcal{C}$	0.239$\mathcal{C}$
0.12	122.2	13.44	1.10	2.20	4.61

obtained numeric results being reported in Table 3.1. The initial value of C_s is taken as the terminal voltage of the battery at no load condition, which ranges from 10 V to 11 V, depending on the experimental data. In order to achieve an unique charging modelling, the initial states of charge are set at 10.5 V for each charging test.

3.2.3 Model Validation

The developed charging model is validated by comparing the simulation results to the experimental data for the LFP battery under test. The voltage profiles obtained at 1$\mathcal{C}$, 0.5$\mathcal{C}$ and 0.239$\mathcal{C}$-rates according to (3.4)-(3.13) are plotted in Fig. 3.6 and

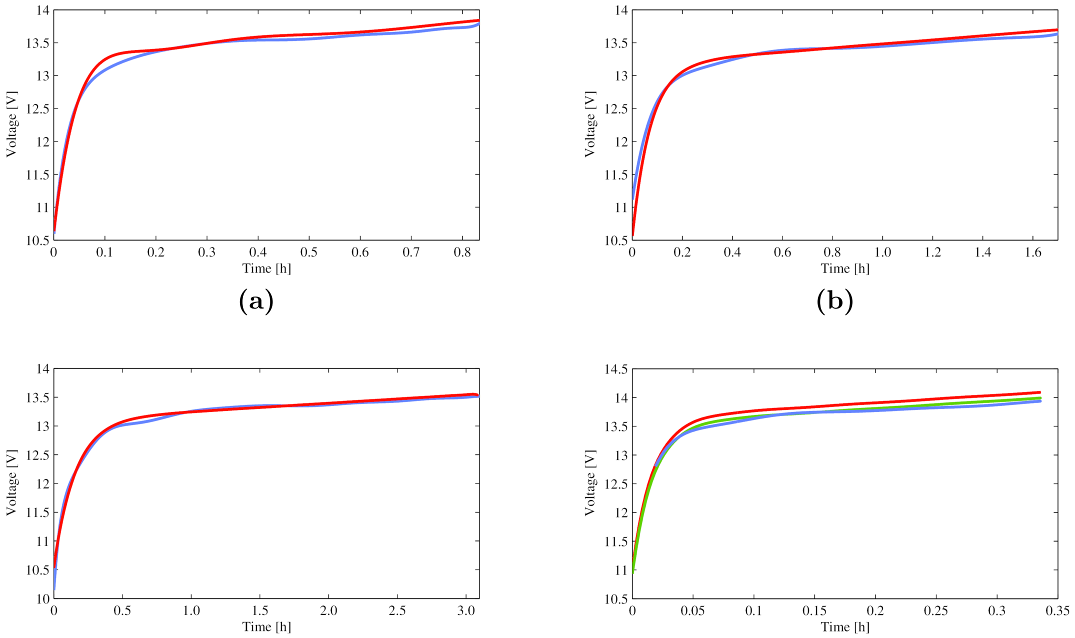

(a) **(b)** **(c)** **(d)**

Figure 3.6: *Comparison between the LFP battery charge profiles obtained from the model (red) and the experimental data (blue). (a) 1$\mathcal{C}$. (b) 0.5$\mathcal{C}$. (c) 0.239$\mathcal{C}$. (d) 2$\mathcal{C}$, with updated DC resistance (green).*

Table 3.2: *Charging model error analysis*

		$\mathbf{1\mathcal{C}}$	$\mathbf{0.5\mathcal{C}}$	$\mathbf{0.239\mathcal{C}}$
Max Error	[V]	0.095	0.553	0.128
	[%]	0.8	5	1.1
Mean Error	[V]	0.049	0.015	0.02

Table 3.3: *Error analysis results at 2$\mathcal{C}$ and 3$\mathcal{C}$, depending on DC resistance updating*

		w/o R_0 updating		with R_0 updating	
		$\mathbf{2\mathcal{C}}$	$\mathbf{3\mathcal{C}}$	$\mathbf{2\mathcal{C}}$	$\mathbf{3\mathcal{C}}$
Max Error	[V]	0.169	0.24	0.07	0.10
	[%]	1.2	1.7	0.5	0.7
Mean Error	[V]	0.134	0.193	0.035	0.054

compared with the experimental charge curves of the tested LFP battery. As can be seen from the figures, the predicted and measured profiles behave similarly and are almost superimposed. The error analyses for the fitted models are given in Table 3.2. The maximum percentage error is 5%, obtained for the simulation at 0.5$\mathcal{C}$. Such a value results from the difference between the modelled initial state of charge and the real one. In fact, in the model the terminal voltage at no load condition is set to be 10.5 V, while the measured one at 0.5$\mathcal{C}$ is about 11 V. The maximum error could be accordingly reduced to 0.7% by implementing the actual data in the battery model. Following these considerations, the measurement of the battery OCV before starting the charge process appears to be of utmost importance in order to correctly estimate both the charging process evolution and the charging time at the set $\mathcal{C}$-rate. To further verify that the proposed battery model is also accurate and effective for higher current rates, the experimental data at 2$\mathcal{C}$ and 3$\mathcal{C}$ are then included for the modelling. The corresponding charging profiles are computed by applying the equivalent circuit model and the parameters previously identified and reported in Table 3.1 (except R_1, which depends on the charging current value). The predicted results are subsequently compared to the measurements. The error analysis for each charging profiles is reported in Table 3.3. Although the found errors are quite limited, such results could be improved by including the measured data at 2$\mathcal{C}$ and 3$\mathcal{C}$ rates in the identification process of the DC resistance and updating its

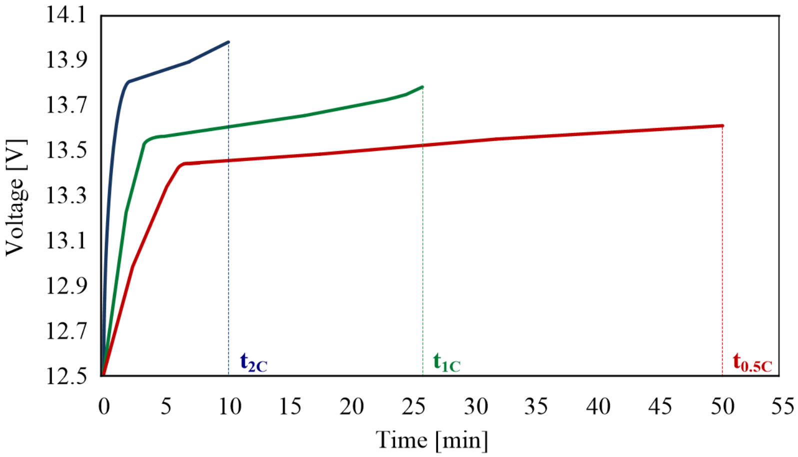

Figure 3.7: *Estimation of charging profiles at different $\mathcal{C}$-rates starting from the knowledge of battery terminal voltage.*

value consequently. A 0.101 Ω resistor is accordingly determined and used to emulate the charging profiles at the highest current rates. In Fig 3.6d, the voltage profiles predicted at $2\mathcal{C}$-rate with and without updating the DC resistance are reported and compared to the experimental data. In addition, Table 3.3 shows the error analysis results. As expected, by comprehending this new R value, the charging process evolution can be predicted with a greater accuracy. These outcomes indicate the feasibility of the proposed charging model for LFP batteries, as well as for high-rates charging applications.

3.2.4 Model Application for EV off-board Smart Chargers

The simple and accurate battery model adopted in this study clearly captures the main features and dynamics of lithium batteries charging performance both at low and high current rates, making it an excellent approach for off-board fast charging applications. In fact, such a model could be usefully implemented in off-board chargers with the aim of on-line forecasting EV charging profiles at various $\mathcal{C}$-rates. This is accomplished on the basis of information provided by the BMS to the charger as soon as the EV has been plugged in. Starting from the knowledge of battery terminal voltage and on the basis of past recharge data, the adopted strategy is able to identify the equivalent circuit model parameters and subsequently predict with a good accuracy charging voltage profiles at different $\mathcal{C}$-rates, as demonstrated in the previous section. An example of results achievable by this approach is reported

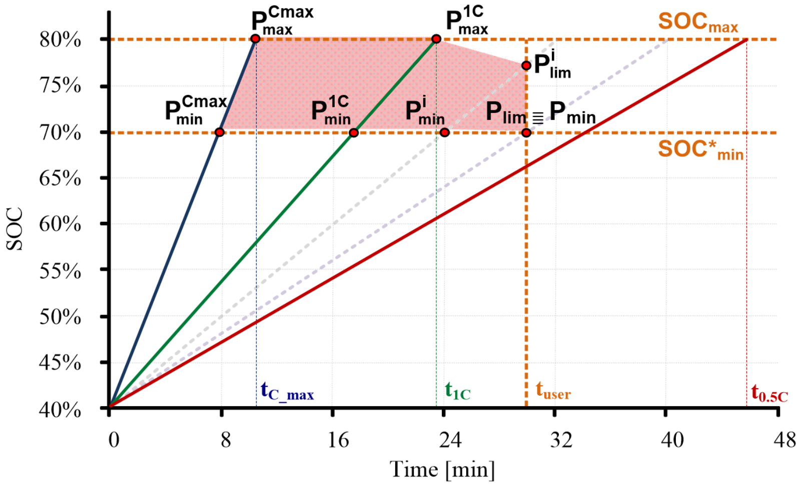

Figure 3.8: *EV's user and charger constraints representation in the (t, SOC) plane: maximum $\mathcal{C}$-rate (blue), 1$\mathcal{C}$ (green) and 0.5$\mathcal{C}$ (red).*

in Fig. 3.7, which shows the charging profiles forecasted at 0.5$\mathcal{C}$, 1$\mathcal{C}$ and 2$\mathcal{C}$ for the tested LFP battery. Such charge curves have been obtained by applying the proposed equivalent model, using the electrical parameters reported in the previous Section and the battery terminal voltage measured at no load condition. The duration of each charge process is also indicated in the figure, showing the time required to reach a battery SOC of about 80%. Another relevant aspect of such an on-line charging estimation process is the ability to identify an appropriate range of final states of charge and charging times which fulfil the EVs user requirements. In particular, these constraints can be expressed as follows:

$$t_{charge} \leq t_{user} \tag{3.14}$$

$$SOC^{*}_{min} \leq SOC \leq SOC_{max} \tag{3.15}$$

where t_{user} represents the EV plugged-in time interval, whereas SOC^{*}_{min} and SOC_{max} are the battery minimum energy level required by the driver and the maximum energy level, respectively. Specifically, the battery SOC should not exceed the upper boundary in order to preserve its rated performances and lifetime, especially at high current rates. Referring to the $(t,\ SOC)$ plane, (3.14) and (3.15) identify the area highlighted in Fig. 3.8. Such a region is also limited by the SOC profile relative to the maximum charging current drawn from the charger. As a consequence, it is possible to choose the most suitable $\mathcal{C}$-rate and EV battery final charging status

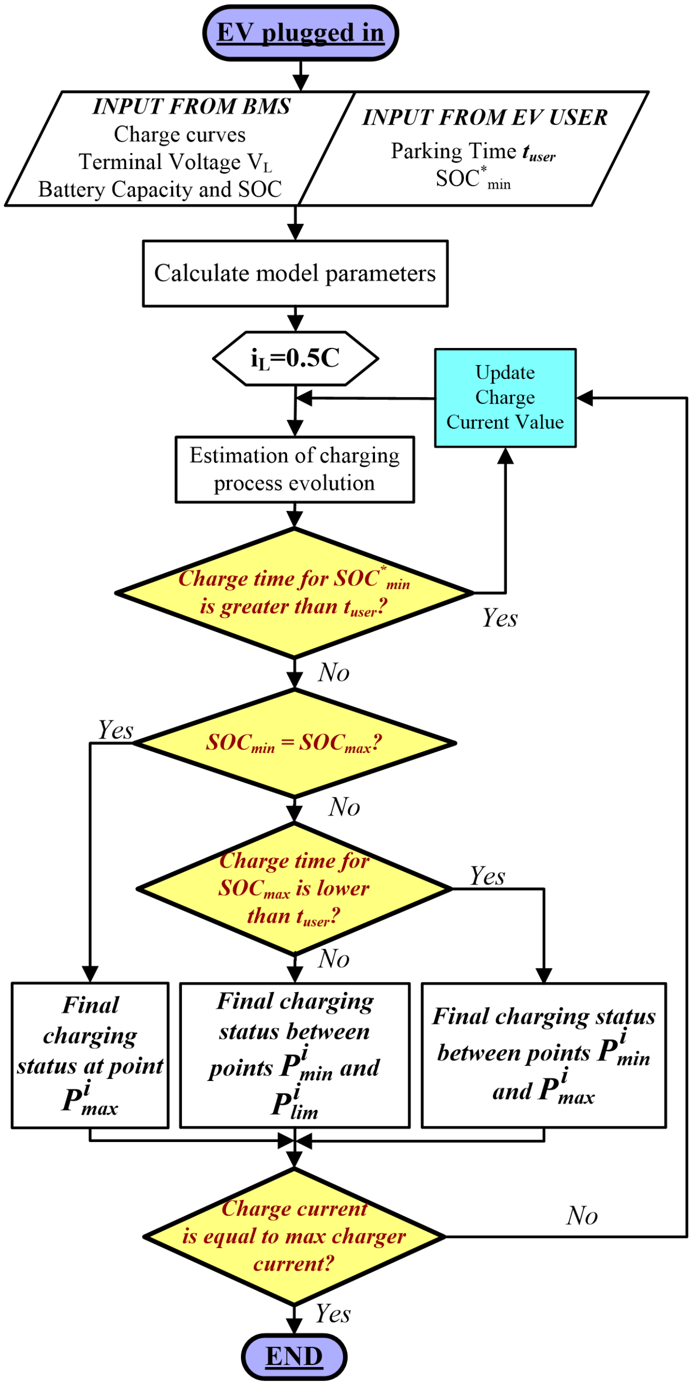

Figure 3.9: *Flowchart of the proposed approach.*

in order to primarily satisfy the EV's user requirements. In particular, following the flowchart related to this approach and illustrated in Fig. 3.9, three different final charging conditions could be found, considering only currents that allow the respect of user constraints. Such conditions identify a range of feasible points on each *t-SOC* curve. This approach could be effectively utilised together with smart charging strategies. In this case, the charge schedule can be selected by the network operator (NO) to meet the driver requirements, as well as the system operator needs. In the smart grid paradigm, an aggregative structure is required in order to enable EVs providing grid services and accessing the market. In fact, the aggregator acts as an intermediary between each EV's user and the NO, appropriately coordinating EV charging [40]. Therefore, as can be observed in Fig. 3.10, all the results of the charging estimation process could be communicated by the charger to the aggregator. Based on set-points sent from the NO and/or market operator (MO), the aggregator appropriately define the recharging power of each plugged EV, consequently determining its charging current and duration. Afterwards, the aggregator will send back the charging control signals to the corresponding charger units which in turn will estimate and communicate in real-time the actual time evolution of the EV load profile. By means of this charging approach, EVs can be hence considered controllable loads, capable of entering into demand response (DR) control programs to provide profitable grid services, such as reducing the peak load, smoothing out the load profile and scheduling the load serving for specific time intervals. Moreover, the entire scheduling process is conducted satisfying the EV's user requirements and respecting the physical constraints of both EV battery and off-board charger unit.

In conclusion, the simulation and experimental results have highlighted that the proposed simplified and generalised model of lithium batteries can accurately represent the charging process of a Lithium Iron Phosphate battery at different current rates. In particular, the modelling approach shows possible applications in the smart grid framework, e.g. for the coordination and energy management of EVs charging processes in off-board charging stations.

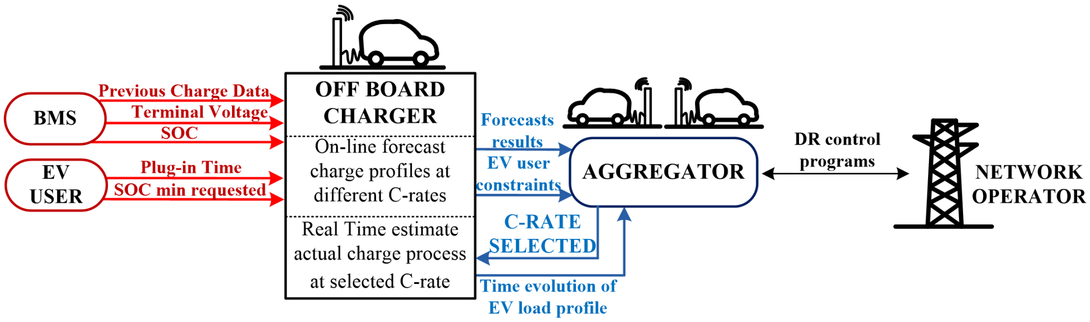

Figure 3.10: *Schematic representation of the proposed smart charging strategy.*

3.3 A dynamic Model of Sodium-Nickel Chloride Batteries

Currently, various battery technologies are already exploited in integrating RESs and in providing smart grid services, such as lead-acid, lithium-ion and sodium-sulfur (NaS) systems. However, their use in stationary energy storage applications is limited owing to several factors. For instance, lead-acid batteries suffer from limited cycle-life, toxicity of lead (Pb) and low energy density, while high energy cost as well as thermal and safety management issues are the challenges related to lithium-based technologies. Also, Na-S batteries still face several obstacles due to safety problems and incident risk [32]. Therefore, alternative battery technologies could be taken into consideration in order to provide successful storage requirement parameters such as high energy density, low cost, high safety, increased cycle-life and environmental compatibility [27].

In this framework, high temperature Sodium-Nickel Chloride batteries (SNBs) have recently emerged as one of the most interesting storage candidates for smart and microgrid applications [110], due to their high discharge rate and pulse power capability, immunity to ambient temperature, unitary coulombic efficiency and intrinsic safety [111–114]. These characteristics make this technology a viable solution to provide several grid-services, such as mitigation of RES power fluctuation, time shifting, voltage regulation and forecasting errors compensation [110]. In order to support the feasible use of this technology in smart grid applications, test and operating performance results need to be provided and analysed. However, presently there is a lack of such data since most studies and applications concern more mature technologies, particularly lithium-ion and lead-acid [104, 115–120]. Considering the importance of model accuracy for batteries deployment, the diffusion of the SNB technology is strictly related to the development and adoption of suitable models able to estimate as precisely as possible the real battery power response in the short- and long-term period. Up to now a few modelling techniques regarding SNBs have been presented in the technical literature [52, 121]. In particular, [121] models the electrochemical behaviour of the sodium-nickel chloride cell considering detailed chemical properties, such as the evolution of the positive electrode reaction front during discharging/charging. Its variations determine the state of an equivalent parallel electrical circuit, whose parameters are however difficult to be determined, especially at low SOC. A pure electrical circuit model is proposed in [52], which consists of an

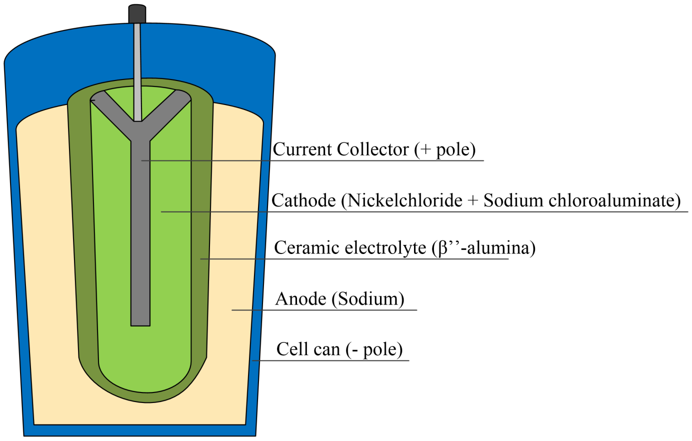

Figure 3.11: *Schematic representation of the SNB cell structure.*

ideal voltage source and a dynamic equivalent internal resistance, the latter varying with the SOC and the temperature. Such an approach is appropriate for long-term management of this kind of storage but presents inaccuracies in modelling the slow and fast dynamics of the battery as well as in forecasting the terminal voltage evolution and power pulse capability.

Based on such considerations, in this Section a two RC-branches dynamic electrical model for a sodium-nickel chloride battery is presented. The proposed modelling is developed from an extensive experimental testing and characterization of a commercial 23.5 kWh SNB, and is validated using a measured current-voltage profile, triggering the whole battery operative range. In particular, the validation results highlight the good performance of the proposed approach in the 90%-40% SOC-range, but also show its inaccuracies in modelling the dynamics and non-linearity occurring at lower SOC. Therefore, it finally demonstrates that more accurate results could be achieved only by implementing a novel equivalent circuit model, specifically developed for sodium-nickel chloride batteries.

3.3.1 The Sodium-Nickel Chloride Technology

The Sodium-Nickel Chloride cell, schematically illustrated in Fig. 3.11, consists of a liquid sodium negative electrode separated from the solid iron/nickel positive electrode by a ceramic electrolyte (β''-alumina), which allows the migration of sodium-ions while acting as a good electric insulator. As the cathode is a solid metal, a second electrolyte in liquid state (sodium chloroaluminate, $NaAlCl_4$) is needed in order to enhance the ion conducting properties of the positive electrode [111]. The melting point of this salt (158°C) determines the minimum operating temperature of the cell but the optimum performance is obtained in the 260°C-350°C temperature range [112]. In fact, at these temperatures the ionic conductivity of the solid electrolyte assumes values that guarantee the lowest contribution of the beta alumina to the internal cell resistance. Thanks to the ceramic electrolyte, the battery has no electrochemical self-discharge and the electrodes are not involved in side-reactions, resulting in a coulombic efficiency of 100% [110, 111, 113]. Additionally, the considered Sodium-Nickel cell has a capacity of 38 Ah and is characterised by an energy density level equal to 280 Wh/l [110]. The reversible reactions provide an open circuit voltage (OCV) of 2.58 V. The overall cell chemical reaction is:

$$NiCl_2 + 2Na \rightleftarrows 2NaCl + Ni \qquad @OCV = 2.58V \tag{3.16}$$

In normal working condition, the secondary electrolyte does not participate to the charge/discharge reactions, but it has a key role in case of cell failure due to β''-alumina breaking. In fact, the presence of $NaAlCl_4$ reduces the effects of the exothermic reactions and generates solid products with low vapour pressure that are not dangerous, neither corrosive nor reactive [110]. Moreover, the generated aluminium acts as a short circuit between the anode and the cathode, by-passing the faulty cell and resulting in a safely operation of the other series-connected cells.

3.3.1.1 The iron-doping effect

One of the most attractive property of this technology is the capability of providing high peak power pulses at any SOC (for a limited discharge duration) [110, 113]. This uncommon result is achieved by adding iron to the cathodic active material, and consequently forming a second sodium/iron cell that takes part in the discharge reaction. Since the open circuit voltage of the iron-chloride is 2.35 V/cell and the nickel-chloride component provides an OCV of 2.58 V/cell, only the nickel cell is discharged at voltage above the iron-cell OCV, in accordance with (3.16).

$$FeCl_2 + 2Na \rightarrow 2NaCl + Fe \qquad @OCV = 2.35V \tag{3.17}$$

In fact, the second reaction (3.17), which discharges the iron chloride, takes place only as soon as the voltage cell drops below 2.35 V [121, 122]. This means that, when the cell voltage rises above the iron-chloride OCV, for instance after a discharge

Table 3.4: *SNB module characteristics.*

	Unit	**Value**
Rated discharge power	kW	7.8
Rated Voltage	V	620
Iron-component OCV	V	564
Energy stored capacity	kWh	23.5
Nominal temperature	°C	260
Calendar life @ 80% DOD	years	15
Cycle-life @ 80% DOD	cycles	4500

power pulse, the iron cell is recharged from the remaining nickel-chloride as in (3.18), making the SNB immediately ready for another high power pulse.

$$NiCl_2 + Fe \rightarrow Ni + FeCl_2 \tag{3.18}$$

This advantage is however combined with a penalty in terms of specific energy reduction because about 20% of the cell capacity is discharged at lower voltage [121].

3.3.1.2 Module structure and electrical characteristics

The tested commercial module is made up of 240 cells connected in series, featuring a total stored energy of 23.5 kWh [110]. The main basic rated operating data of the considered SNB module are reported in Table 3.4. In the module, the cells are enclosed in a metallic battery container and packaged within a sealed, vacuum modular casing. The complete assembly includes also the ohmic heater, which is controlled by the battery management system (BMS) for internal temperature control. Besides, the BMS provides a number of additional functions, namely charge regulation, monitoring and diagnostic through measurement and elaboration of battery parameters, as well as remote maintenance and supervising by means of CAN-bus and/or LAN interfaces and communication protocols [113].

3.3.2 SNB Modelling

Based on the previous analysis of battery modelling approaches, the non-linear two RC-branches dynamic electrical model reported in Fig. 3.12 is applied for the SNB

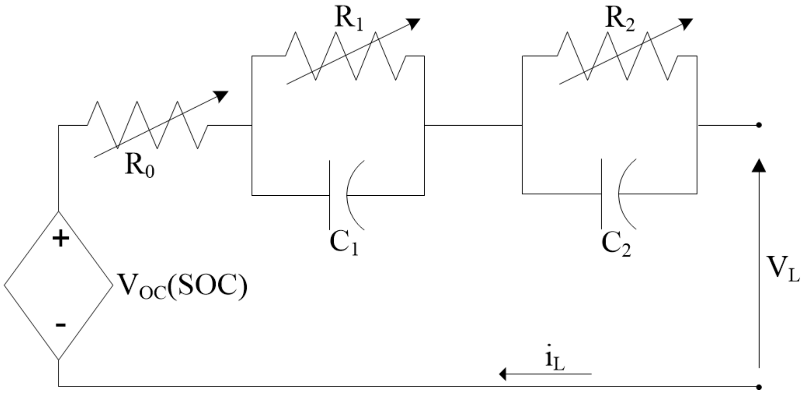

Figure 3.12: *Proposed equivalent circuit model for the SNB module.*

technology. The implemented SNB model consists of three main parts: a controlled voltage source V_{OC} representing the battery open circuit voltage, an internal resistance R_0 and two parallel polarization RC circuits. In particular, V_{OC} is the equilibrium potential of the battery; R_0 is the ohmic internal resistance of circuit and electrodes; while the two RC parallel elements model the transient response of the battery. In fact, R_1 and C_1 describe the fast battery dynamics related to reaction kinetics and surface effects on the electrodes arisen from double-layer formation, whereas R_2 and C_2 represent the slower dynamics typical of diffusion processes in the electrolyte and active materials. The model parameters depend non-linearly on the battery SOC, temperature and current rate. In addition, their values are also influenced by the current path, which takes into account whether the battery has recently experienced a charge or discharge process. In order to define the model parameters and correctly evaluate battery performance, the SOC-tracking during battery operation is of particular importance. Referring to the SNB technology, the SOC estimation can be simply evaluated by applying the coulomb-counting method, since the cells are 100% coulombically efficient:

$$SOC(t) = SOC(t-1) + \frac{1}{C_B} \int i_L(t)\, dt \tag{3.19}$$

where C_B represents the nominal battery capacity and i_L is the battery current, defined positive for the charging process. As far as the considered electrical battery model and the current-voltage relationships of its components are concerned, the following equations can be used to describe the battery terminal voltage V_L and the voltages over the resistor-capacitor branches:

$$V_L = V_{OC} + R_0 \cdot i_L + V_1 + V_2 \tag{3.20}$$

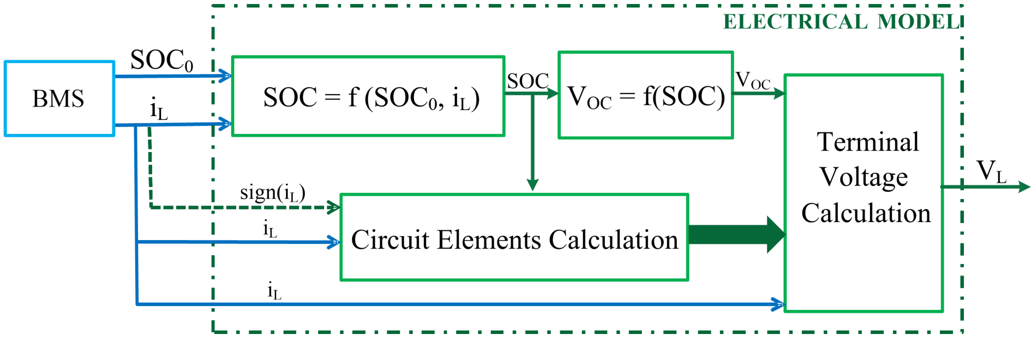

Figure 3.13: *Schematic block representation of the Simascape equivalent model.*

$$V_1 + \tau_1 \frac{dV_1}{dt} = R_1 \cdot i_L \tag{3.21}$$

$$V_2 + \tau_2 \frac{dV_2}{dt} = R_2 \cdot i_L \tag{3.22}$$

$\tau_i{=}R_iC_i$, $i \in \{1,2\}$ being the time constants of the corresponding RC-branch. Equation (3.20) implies that, during the relaxation period ($i_L{=}0$), the terminal voltage V_L approaches the battery V_{OC}, as the polarization and diffusion phenomena weaken, resulting in the RC-circuit voltage decrease with decay rates determined by the time constants τ_i. As a consequence, assuming a rest time sufficiently long, the V_{OC} can be identified by evaluating the steady-state terminal voltage of the battery. The second order battery circuit is then implemented in the Matlab/Simulink environment, by using the Simscape language. This modelling choice allows to create custom circuit elements containing either multidimensional look-up tables or mathematical functions that are used to map the non-linearity of model parameters. In fact, since the Simscape platform is a physical modelling tool, the equivalent electrical circuit elements can be developed using components like resistors and capacitors, obtaining a more intuitive battery model. Moreover, the need of correlating the SNB electrical behaviour to its thermal performance can be satisfied by exploiting the Simscape multi-domain capability. Nevertheless, for the sake of simplicity, the implemented electrical model evaluates the circuit parameters for just one internal temperature. As a result, the schematic block representation of the implemented Simscape model is depicted in Fig. 3.13.

3.3.2.1 Parameter Identification Method

The method used to identify the model parameters is based on the analysis of the battery terminal voltage evolution during pulse discharge experiments. These tests

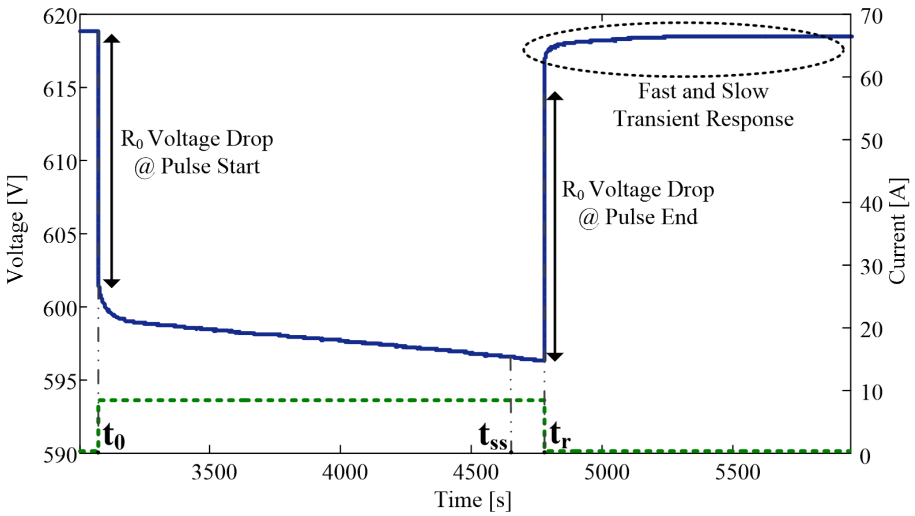

Figure 3.14: *Voltage response to a step load-current event for the SNB module: battery terminal voltage (blue) and current (dashed-green). The indication of the steady-time instant, i.e.* t_{ss}*, is intended for guidance only.*

consist of a sequence of constant current pulses aimed at characterising the whole SOC range. Between each pulse, a rest time interval is set, allowing the analysis of the voltage relaxation characteristic. The duration of rest time and the number of pulses are both a compromise between accuracy and test duration. Starting from the examination of a generic pulse, the voltage response to a step load-current event can be observed in Fig. 3.14. Firstly, the internal resistance R_0 can be easily calculated by (3.23), after the preliminary identification of the associated voltage variation (ΔV) when the current step is beginning or ending (ΔI):

$$R_0 = \left|\frac{\Delta V}{\Delta I}\right|. \tag{3.23}$$

Secondly, considering the response of the battery during the relaxation phase, the time constants of RC-branches as well as the capacitor voltages can be determined by fitting the fast and slow dynamics of the battery voltage by means of (3.24).

$$V_L = V_{OC} - U_1 \cdot e^{-t/\tau_1} - U_2 \cdot e^{-t/\tau_2}, \tag{3.24}$$

$U_{1,2}$ being the initial voltages of the two RC circuits at the beginning of the rest period (t=t_r). Subsequently, from the analysis of the capacitor responses to the initial current step and knowing $\tau_{1,2}$ and $U_{1,2}$, the preliminary estimations of R_1, C_1,

R_2 and C_2 are obtained. In particular, at $t{=}t_0^-$ before the current step is applied, the capacitors can be considered fully discharged since all the polarization and diffusion phenomena due to the previous step can be assumed to be exhausted. Because the capacitances state can not change instantaneously, their voltages are still equal to zero at $t{=}t_0^+$. Then, the battery is discharged at constant current for a period sufficiently long to assume that the steady-state has been reached ($t{=}t_{ss}$). From this time, C_1 and C_2 behave similarly to open-circuits, their voltages being those on R_1 and R_2, respectively. Based on these considerations, (3.25) holds.

$$V_i = \begin{cases} 0 & t = t_0 \\ R_i \cdot i_L & t_{ss} \leq t < t_r \end{cases} \qquad \forall i \in \{1, 2\}. \tag{3.25}$$

Thus, the complete capacitors response to the initial current step can be written as follows:

$$V_i(t) = V_i(t_{ss}) + [V_i(t_0) - V_i(t_{ss})]e^{-t/\tau_i} = R_i \cdot i_L(1 - e^{-t/\tau_i}) \quad \forall i \in \{1, 2\}. \tag{3.26}$$

By setting the time as the beginning of the rest time, i.e. $t{=}t_r$, the initial guesses of resistances and capacitances can be calculated by means of (3.27):

$$R_i = \frac{U_i}{i_L(1 - e^{-t_r/\tau_i})}; \;\; C_i = \frac{\tau_i}{R_i} \quad \forall i \in \{1, 2\}. \tag{3.27}$$

Finally, in order to optimise parameter identification and minimise the modelling error, the non-linear least-squares solver provided by the Simulink Optimization Toolbox is exploited. Specifically, each estimation task is performed in the Simulink Design Optimization environment, which provides the link between the Simscape battery model, the experimental test data, and the chosen optimisation algorithm. Furthermore, the optimisation estimation problem has been well-formulated in order to avoiding suboptimal local minima, by including suitable parameter bound constraints and initial guesses, derived from (3.23)-(3.27).

3.3.3 Experimental results

3.3.3.1 Battery Test Set-up

The characterization of the SNB module and its subsequent validation tests are performed by using the experimental DC set-up depicted in Fig. 3.15. Discharging

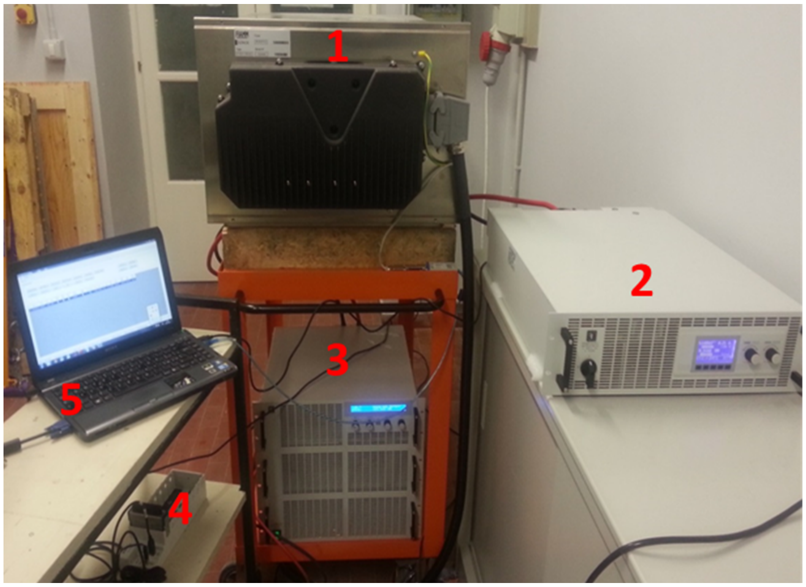

Figure 3.15: *Battery test set-up: 1) SNB module, 2) DC Power Supply, 3) DC Electronic Load, 4) Data Acquisition System, 5) Host PC.*

processes are managed by a programmable DC electronic load (EL EL-9750- 75 HP by Elektro-Automatik), which features maximum current, voltage and power of 75 A, 750 V, and 7.2 kW, respectively. An EA PSI-81500-30 3U is used as power supply during charging. It can be exploited as controlled voltage or current source with output voltage- and current-range equal to 0-1500 V and 0-30 A, respectively, its maximum output power being 15 kW. A National Instruments cDAQ-9172 equipped with a NI-9205 module is used to measure and acquire battery current and voltage. All equipment is controlled and managed by means of Virtual Instruments (VIs) specifically developed in the NI-Labview environment. All measurements can be monitored online from the host computer through the VIs Graphical User Interface (GUI), as shown in Fig 3.16. It permits to choose the device to perform the test on the SNB module and to set the threshold levels for voltage, current and SOC. The program is able to set the acquisition sampling time and to receive specific measurements from the electronic load and power supply, such as the Ah counter and elapsed time data. Discharging and charging processes are managed by properly coordinating the VIs and the BMS software. In fact, battery characterisation tests can be performed only by enabling the corresponding function into the BMS MonitorST523 management software, as reported in Fig. 3.17. It allows to check the status of the battery pack, control the warm-up and SOC-reset charge as well as empower charg-

if Level A or B is selected, current and power limit commands MUST be changed in the Block Diagram

Device array: 0
Port: ASRL6::INSTR
Device type: EL 9750-75
Device serial number: 1326170004
Device article number: 33200254
Device node: 1
Number of devices: 2
Discharge continuous currrent [A]: 11 (from 2.38A to 12 A)
Max Discharge Power[W]: 7200 (max 7.2 kW (lower values should be selected in accordance with the set current value))
Min Discharge Voltage [V]: 534 (from 480V to 540V depending on the selected discharge current)
DESIRED FINAL SOC [%]: 0
Max Discharge Capacity [Ah]: 37,98
Initial Battery Capacity [Ah]: 3,825
SAMPLING TIME [ms]: 300
PATH:
FILE NAME: .txt
Current: 0
Voltage: 0
Power: 0
Discharge Capacity [Ah]: 0
SOC [%]: 0
Elapsed Time array: 1
Ah Residui: 0

Figure 3.16: *VI User interface to control the SNB testing equipment*

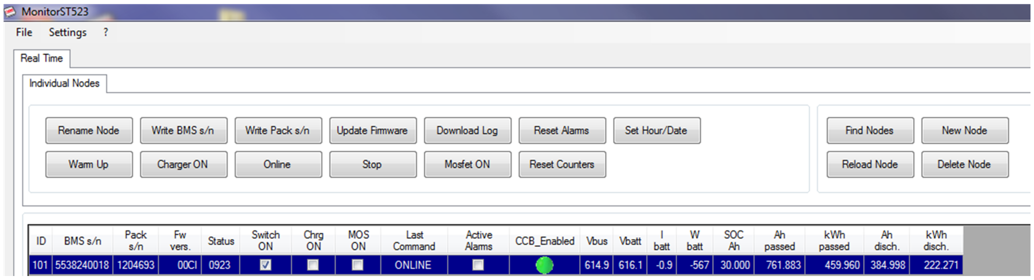

ID	BMS s/n	Pack s/n	Fw vers.	Status	Switch ON	Chrg ON	MOS ON	Last Command	Active Alarms	CCB_Enabled	Vbus	Vbatt	I batt	W batt	SOC Ah	Ah passed	kWh passed	Ah disch.	kWh disch.
101	5538240018	1204693	00CI	0923	☑	☐	☐	ONLINE	☐	●	614.9	616.1	-0.9	-567	30.000	761.883	459.960	384.998	222.271

Figure 3.17: *BMS software MonitorST523*

ing/discharging tests depending on battery temperature, SOC and voltage levels. All measurements are stored in the BMS memory and can be downloaded as a *.bin* file and decoded in a *.csv* format for an easier handling. Current voltage and temperature data are recorded by the BMS at variable time steps, depending on their amplitude changes during the ongoing test. Therefore, data from VIs and BMS are combined and merged in order to obtain a unified data structure and consequently extract all the relevant information for the battery modelling and characterisation.

3.3.3.2 Model Parameters Identification: Analysis of Results

The pulse discharge experiment at $0.25\mathcal{C}$ rate reported in Fig. 3.18 has been carried out in order to characterise the battery OCV and extract mappings for the battery parameters in the 90%-10% SOC-range. The test provides data at 10% SOC-step with 20-minutes rest time up to 30% SOC. At lower SOC, the pulse rate is reduced to 5% and the relaxation period increased to 40 minutes in order to better analyse the effects of iron-doping on the battery voltage and parameters. In fact, as can be observed in Fig. 3.18, the iron chloride OCV is hit during the discharge step between 40%-30% SOC, resulting in a significant impact on the voltage dynamics, especially

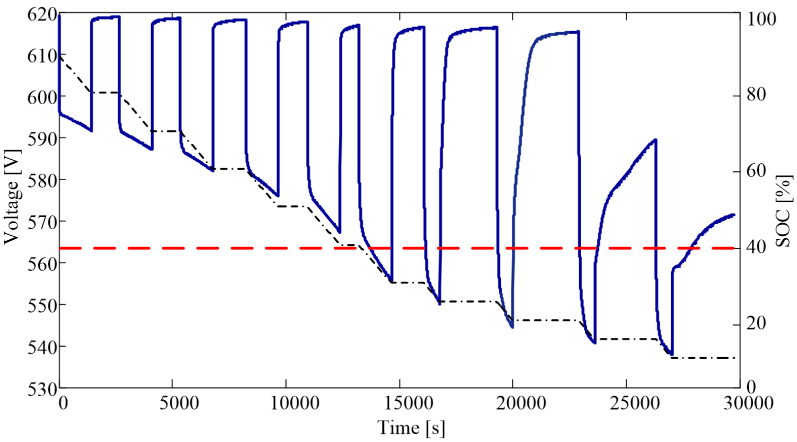

Figure 3.18: *Pulse discharge experiment at 0.25C rate. Measured voltage (blue) and iron-component open circuit voltage (dashed red) on the left axis, and SOC (dashed black) on the right axis.*

at the beginning of the relaxation phases. The resulting parameter mappings are presented in Fig. 3.19, whereas the simulation outcomes can be observed in Fig. 3.20. As can be seen from the figures, the predicted and measured profiles behave similarly and are almost superimposed. The mean absolute percentage error (MAPE) and the maximum percentage error (PE_{max}) are 0.19% and 1.9%, respectively. Such a value of PE_{max} can be explained by noting that the error greatly rises during transients below 30% SOC, due to the effect of the iron-doping, as previously mentioned. Particularly, three different discharging behaviours can be identified in the experimental stepped voltage curve:

1. 90% – 40% *SOC-range*: both the discharge and rest phases are influenced only by the nickel-component of the cathode;

2. 30% – 20% *SOC-range*: during the discharge process also the iron-reaction takes place. As soon as the current-step terminates, the battery voltage rises above the iron-chloride OCV and the iron cell is gradually recharged from the remaining nickel-chloride;

3. 15% – 10% *SOC-range*: the nickel-cell is almost totally depleted and is not able to substantially boost the restoration process of the battery OCV during the rest time. Consequently, the steady-state voltage is not reached within the 40-minutes relaxation period.

Clearly, two *RC* circuits are not able to capture such a real behaviour of the SNB. As

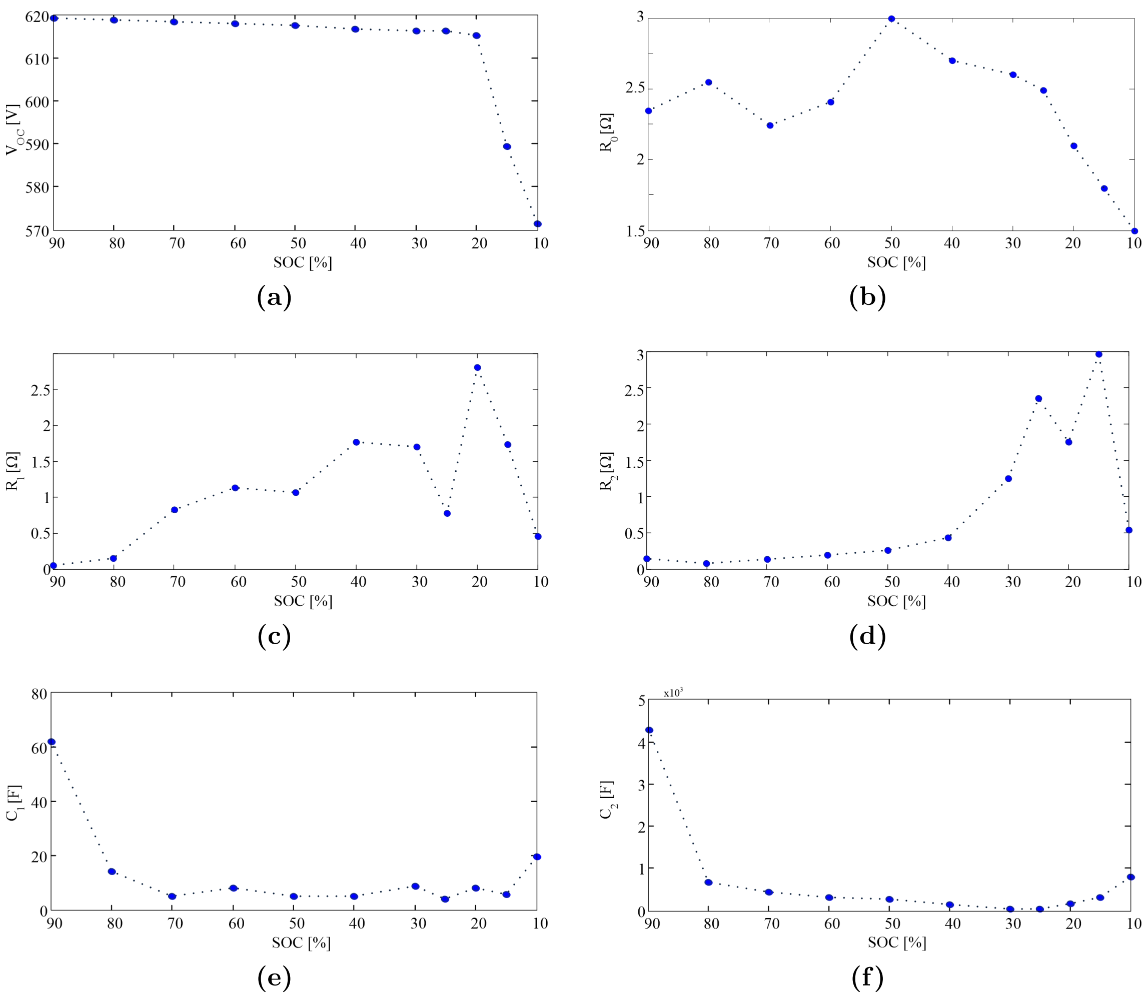

Figure 3.19: *Battery parameter mappings: (a)* V_{OC}*, (b)* R_0*, (c)* R_1*, (d)* R_2*, (e)* C_1*, (f)* C_2*.*

a consequence, a novel equivalent circuit model needs to be specifically developed in order to represent the very uncommon dynamics and non-linearities of this battery technology.

3.3.3.3 Model Validation

The model has been validated using a measured current-voltage profile of the SNB module. The test was performed by discharging the battery at asymmetrical current pulses spaced out by variable rest time intervals in order to trigger the whole SOC range at different operating conditions. The results of the validation experiment can

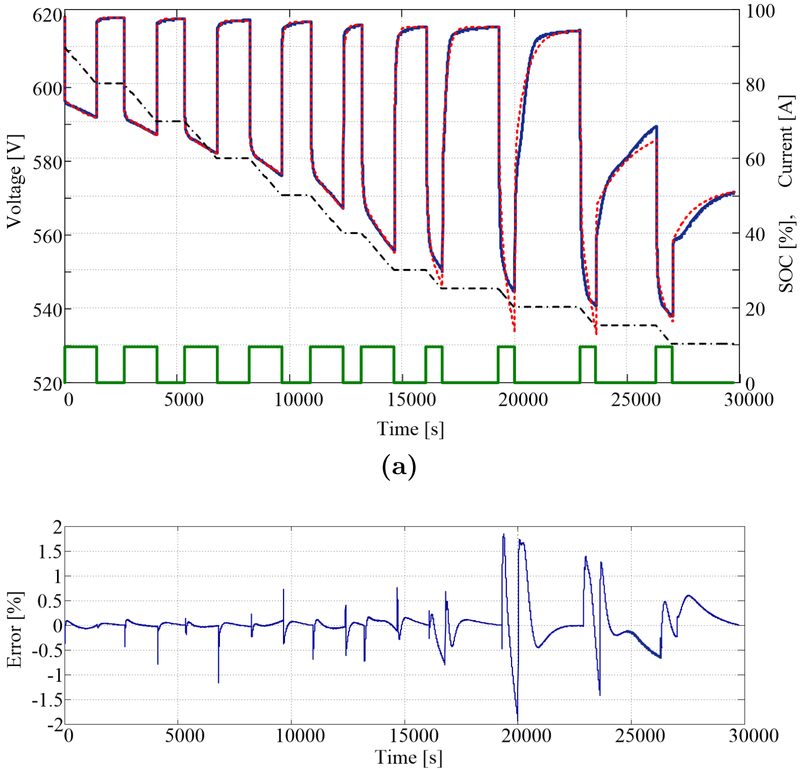

(a)

(b)

Figure 3.20: *Pulse discharge experiment at 0.25C rate. (a) Measured (blue) and simulated voltage (dashed red) on the left axis, and measured current (green) and SOC (dashed black) on the right axis. (b) Voltage percentage error.*

be observed in Fig. 3.21. As expected, the predicted profile is accurate in the 90%-40% range, but is not able to follow the battery dynamics at lower SOC, particularly below 20%. In fact, even small inaccuracies in modelling have great influence on the simulation results, because of the high non-linearity of the OCV-curve at this stage. The analysis of Fig. 3.21b shows that with a second-order model the MAPE and PE_{max} are 0.6% and 2.8%, respectively. The development of a specific model, which can predict the peculiar dynamics and behaviour of the SNBs, is necessary to further improve the results accuracy.

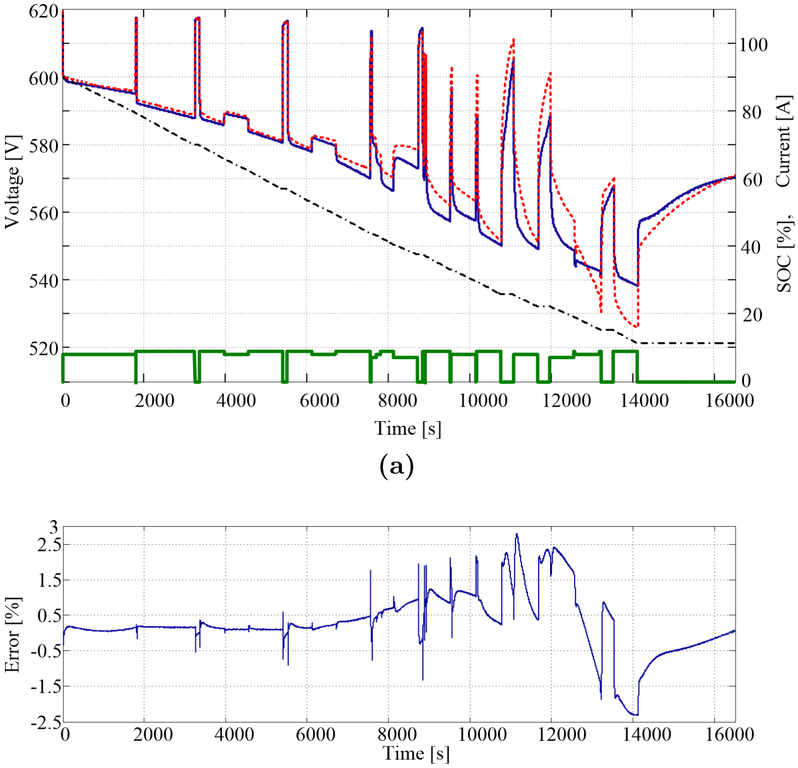

(a)

(b)

Figure 3.21: *Validation test at asymmetrical current pulses. (a) Measured (blue) and simulated voltage (dashed red) on the left axis, and measured current (green) and SOC (dashed black) on the right axis. (b) Voltage percentage error.*

3.3.3.4 Hysteresis Effect

The iron-doping of the positive electrode causes also an evident hysteresis effect on the battery OCV, as shown in Fig. 3.22. In fact, the measurement of steady-state voltage after charging and discharging pulses highlights the strong dependence of the battery OCV on the current path from 5% to 30% SOC. This phenomenon happens because, when charging begins, the iron and nickel components are recharged at the same time, contrary to what happens during the discharge process, as previously explained. This result implies that the dependence of battery parameters from the current path needs to be take into account in developing an accurate SNB model. Particularly, the novel model should be able to well-represent the different impact of the iron-doping during charging and discharging processes, as well.

In conclusion, the simulation and experimental results have highlighted that the

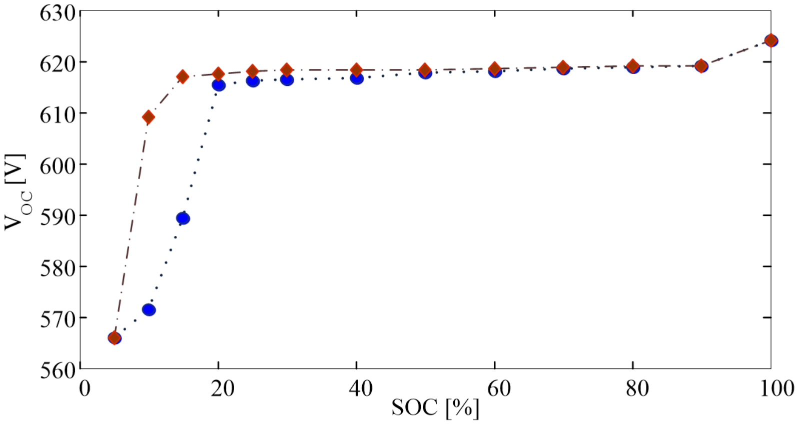

Figure 3.22: *Hysteresis effect between discharge V_{OC} curve (dashed-circle blue) and charge V_{OC} curve (dashed-diamond orange)*

proposed two RC-branches dynamic electrical model for sodium-nickel chloride batteries can accurately represent DC dynamics and behaviour in the 90%-40% SOC range. The analysis of the experimental performance has however revealed a strong impact of the cathodic iron doping on the battery operations. The dynamics and non-linearities occurring at lower SOC are hence mainly due to the mixed iron/nickel cathode and are the principal cause of the model inaccuracies. It finally demonstrates that more accurate results could be achieved only by implementing a novel equivalent circuit model, specifically developed for sodium-nickel chloride batteries and able to deal with the non-linearities introduced by the iron-doping.

Conclusions and Future Developments

The increasing use of Renewable Energy Sources (RESs), supported by economic subsidies and environmental policies, is changing the structure of the power system, contributing to its transformation from a centralized to a distributed form. However, the critical issues related to RES production (such as variability, discontinuity and poor predictability) are giving rise to new challenges in terms of reliability and control of electrical power systems. One of the solutions proposed to deal with these challenges is the integration of Energy Storage Systems (ESSs), which represent hence a key component in the deployment of active electricity network configurations. However, the presence of ESSs both in centralised and distributed configuration can make the management of power balance and the definition of the supervisory strategy a challenging task. In fact, storage devices introduce additional degrees of freedom in the control of the system that thus needs to be carefully defined. Defining the best management and operating mode for ESSs can have a significant impact on the power systems operation since storage power outputs can be controlled in order to reach several objectives (e.g. reducing the system energy cost, minimising power losses, shifting peak load, compensating RES power fluctuations and forecasting errors, and reducing the dependence from the main utility grid).

In this PhD dissertation, several algorithms and methodologies for the management of microgrids (MGs) and Virtual Power Plants (VPPs), integrating RES generators and battery ESSs, are proposed and analysed for four cases of study, aimed at highlighting the potentialities of integrating ESSs in different smart grid architectures. In particular, a rule-based management strategy for VPPs integrating Vehicle-to-Grid (V2G) storage systems and stationary batteries has been firstly proposed. It aims at hourly balancing the VPP load demand and generation by properly coordinating all the VPP power units (fossil and RES generators, controllable loads and storage systems). Simulation results have highlighted the economic and energy benefits given by the integrated ESS configuration. In particular, the synergy between V2G and battery ESS allows the achievement of more robust VPP configuration, permitting to make the results less dependent on the uncertainty connected to V2G infrastructures. Then, an EMS (Energy Management System) rule-based strategy has been presented in order to manage a 100% RES-based MG, which will be developed from an existing municipal waste treatment platform. Its preliminary design aims at studying the possibility to effectively integrate a small-scale Concentrating Solar Power (CSP) plant with a thermocline thermal storage tank and a stationary battery system in an industrial MG. In particular, the simulation results have demonstrated that an *ad-hoc* management strategy could be effectively implemented in order to completely satisfy the load demand and ensure the accomplishment of scheduled microgrid power-to-grid profiles, highlighting the effectiveness of the proposed management algorithm, as well. An optimal control problem formulation, based on the control theory of trajectory optimization, has been finally proposed. This choice allows the application of Pontryagin's Minimum Principle (PMP), which can be solved analytically with low computational effort, making it suitable for on-line applications. The worth and effectiveness of the proposed approach have been verified through two simulation cases of study. The former refers to the optimal integration of V2G storage in a cluster of MGs, while the latter concerns ESSs integration in grid-connected hybrid microgrids. In both cases, the simulation results have highlighted that the proposed optimal V2G and ESS scheduling strategies can be effectively implemented in order to minimise the dependence of MG clusters from the main grid and increase their energy autonomy as well as optimise MGs daily electricity cost, considering real-time prices and variable MG generation.

The promising results obtained in the energy management of power systems by means of the use of ESSs and V2G technologies have highlighted the importance of reliable component models in the implementation of the control strategies. In fact, the performance of the EMS is only as accurate as the data provided by models, batteries being the most challenging element in the presented cases of study. Therefore, in the second part of this Thesis, the issues in modelling battery technologies are addressed, particularly referring to Lithium-Iron Phosphate (LFP) and Sodium-Nickel Chloride (SNB) systems. Firstly, an LFP charging model for smart EV applications has been proposed. The aim is the on-line forecast of EV charging profiles at various C-rates in order to subsequently control the process by its implementation in off-board chargers. The model has been experimentally validated testing a 2.3 Ah LFP battery. The comparison between the experimental results and the simulations at different charging conditions have highlighted a good accuracy, even at high C-rates. Secondly, a high temperature SNB dynamic model has been suggested. The proposed model is based on an extensive experimental testing and characterization of a commercial 23.5 kWh SNB, paying specific attention to the analysis of the iron doping effect on the battery operation. The model has been validated using a measured current-voltage profile, constituted of an asymmetrical sequence of current steps and relaxation intervals. The validation results demonstrate the good performance of the proposed approach in a defined SOC range. However, due to the particular chemical composition of the battery positive electrode, a novel modelling approach specific for the SNB technology has been finally demonstrated to be necessary.

In conclusion, as the diffusion of smart grids and EVs is worldwide fostered, electrical storage systems will play an increasing crucial role, becoming critical elements of the future power networks. Their modelling and management are therefore two of the main challenges which need to be addressed in the short-mid period. The presented results highlight the effectiveness of the developed approaches for the useful integration of several storage technologies in the smart grid framework. Nevertheless, the need for strategies directly implementable on-line opens for further development of adaptive-PMP algorithms and for their field testing in experimental pilot power plants. Moreover, future works are planned in order to face the challenges of modelling Sodium-Nickel Chloride batteries, by researching and developing a novel equivalent circuit model, specifically developed for this storage technology and able to deal with the non-linearities introduced by the cathode iron-doping.

Bibliography

[1] Lopes, J. A. P., A. G. Madureira, and C. C. L. M. Moreira (2013) "A view of microgrids," *WIREs Energy Environ*, **2**, pp. 86–103.

[2] Jenkins, N., J. Ekanayake, and G. Strbac (2010) *Distributed Generation*, Institution of Engineering and Technology.

[3] Melhem, Z. (2013) *Electricity Transmission, Distribution and Storage Systems*, Woodhead Publishing.

[4] Commission of the European Union (2010), "Smart Grids European Technology Platform," `http://www.smartgrids.eu`.

[5] Su, W. and J. Wang (2012) "Energy management systems in microgrid operations," *The Electrity Journal*, **25**(6), pp. 45–60.

[6] Lasseter, R. and P. Paigi (2004) "Microgrid: a conceptual solution," in *IEEE Annual Power Electronics Specialists Conference, Electrical Drives, Automation and Motion*, pp. 4285–4290.

[7] Chowdhury, S., S. P. Chowdhury, and P. Crossley (2009) *Microgrids and Active Distribution Networks*, Institution of Engineering and Technology.

[8] Asmus, P. (2010) "Microgrids, Virtual Power Plants and Our Distributed Energy Future," *The Electricity Journal*, **23**(10), pp. 72 – 82.

[9] Hatziargyriou, N. (2014) *Microgrids: Architectures and Control*, Wiley-IEEE Press.

[10] Palizban, O., K. Kauhaniemi, and J. M. Guerrero (2014) "Microgrids in active network management Part I: Hierarchical control, energy storage, virtual power plants, and market participation," *Renewable and Sustainable Energy Reviews*, **36**, pp. 428–439.

[11] Musio, M. and A. Damiano (2010) "Vehicles to Grid (V2G) concept applied to a Virtual Power Plant Structure," in *IEEE International Conference on Electrical Machines - (ICEM)*, pp. 1–6.

[12] NREL - National Center for Photovoltaics (2015), `http://www.nrel.gov/ncpv`.

[13] Philipps, S. P., A. W. Bett, K. Horowitz, and S. Kurtz (2016) *Current status of concentrator photovoltaic (CPV) technology*, *Tech. rep.*

[14] (2013) "Australia's largest CPV solar power station opened," *Renewable Energy Focus*, **14**(4).

[15] (2011) "Soitec CPV plant powers COP17 climate talks," *Renewable Energy Focus*, **12**(6).

[16] Fernndez, E. F., P. Prez-Higueras, A. J. Garcia Loureiro, and P. G. Vidal (2013) "Outdoor evaluation of concentrator photovoltaic systems modules from different manufacturers: first results and steps," *Progress in Photovoltaics: Research and Applications*, **21**(4), pp. 693–701.

[17] Ghosal, K., D. Lilly, J. Gabriel, M. Whitehead, et al. (2014) "Semprius Field Results and Progress in System Development," *IEEE Journal of Photovoltaics*, **4**(1), pp. 703–708.

[18] Luque, A. and V. Andreev (2007) *Concentrator Photovoltaics*, Springer.

[19] Chong, K.-K., S.-L. Lau, T.-K. Yew, and P. C.-L. Tan (2013) "Design and development in optics of concentrator photovoltaic system," *Renewable and Sustainable Energy Reviews*, **19**, pp. 598 – 612.

[20] Garcia, I., P. Espinet-Gonzaalez, I. Rey-Stolle, and C. Algora (2011) "Analysis of chromatic aberration effects in triple-junction solar cells using advanced distributed models," *IEEE Journal of Photovoltaics*, **1**(2), pp. 219–224.

[21] Almonacid, F., P. Prez-Higueras, E. F. Fernndez, and P. Rodrigo (2012) "Relation between the cell temperature of a {HCPV} module and atmospheric parameters," *Solar Energy Materials and Solar Cells*, **105**, pp. 322 – 327.

[22] Chemisana, D., A. Vossier, L. Pujol, A. Perona, and A. Dollet (2011) "Characterization of Fresnel lens optical performances using an opal diffuser," *Energy Conversion and Management*, **52**(1), pp. 658 – 663.

[23] Garcia, I., C. Algora, I. Rey-Stolle, and B. Galiana (2008) "Study of non-uniform light profiles on high concentration III-V solar cells using quasi-3D distributed models," in *IEEE Photovoltaic Specialists Conference*, pp. 1–6.

[24] Herrero, R., M. Victoria, C. Domnguez, S. Askins, et al. (2012) "Concentration photovoltaic optical system irradiance distribution measurements and its effect on multi-junction solar cells," *Progress in Photovoltaics: Research and Applications*, **20**(4), pp. 423–430.

[25] Malhotra, A., B. Battke, M. Beuse, A. Stephan, et al. (2016) "Use cases for stationary battery technologies: A review of the literature and existing projects," *Renewable and Sustainable Energy Reviews*, **56**, pp. 705 – 721.

[26] Ibrahim, H. and A. Ilinca (2013) *Energy Storage - Technologies and Applications*, InTech.

[27] Cho, J., S. Jeong, and Y. Kim (2015) "Commercial and research battery technologies for electrical energy storage applications," *Progress in Energy and Combustion Science*, **48**, pp. 84 – 101.

[28] Boicea, V. A. (2014) "Energy Storage Technologies: The Past and the Present," *Proceedings of the IEEE*, **102**(11), pp. 1777 – 1794.

[29] Jiayuan, W., S. Zechang, and W. Xuezhe (2009) "Performance and characteristic research in LiFePO4 battery for electric vehicle applications," in *IEEE Vehicle Power and Propulsion Conference*, pp. 1657–1661.

[30] Marongiu, A., A. Damiano, and M. Heuer (2010) "Experimental analysis of lithium iron phosphate battery performances," in *2010 IEEE International Symposium on Industrial Electronics*, pp. 3420–3424.

[31] Sandia National Laboratories (2013) *DOE/EPRI 2013 Electricity Storage Handbook*, *Tech. rep.*

[32] (2012), "NAS battery fire incident and response. Nagoya; NGK," `http://www.ngk.co.jp/english/news/2012/0607.html`.

[33] Benato, R., N. Cosciani, G. Crugnola, et al. (2015) "Sodium nickel chloride battery technology for large-scale stationary storage in the high voltage network," *Journal of Power Sources*, **293**, pp. 127–136.

[34] Alotto, P., M. Guarnieri, and F. Moro (2014) "Redox flow batteries for the storage of renewable energy: A review," *Renewable and Sustainable Energy Reviews*, **29**, pp. 325 – 335.

[35] Tan, X., Q. Li, and H. Wang (2013) "Advances and trends of energy storage technology in Microgrid," *International Journal of Electrical Power & Energy Systems*, **44**(1), pp. 179 – 191.

[36] Quinn, C., D. Zimmerle, and T. Bradley (2012) "An evaluation of state-of-charge limitations and actuation signal energy content on plug-in hybrid electric vehicle, vehicle-to-grid reliability, and economics," *IEEE Transaction on Smart Grid*, **3**(1), pp. 483–491.

[37] Kempton, W. and J. Tomi (2005) "Vehicle-to-grid power implementation: From stabilizing the grid to supporting large-scale renewable energy," *Journal of Power Sources*, **144**(1), pp. 280 – 294.

[38] Tomi, J. and W. Kempton (2007) "Using fleets of electric-drive vehicles for grid support," *Journal of Power Sources*, **168**(2), pp. 459 – 468.

[39] Kempton, W. and J. Tomic (2005) "Vehicle-to-grid power fundamentals: Calculating capacity and net revenue," *Journal of Power Sources*, **144**(1), pp. 268–279.

[40] Damiano, A., G. Gatto, I. Marongiu, et al. (2014) "Vehicle-to-grid technology: State-of-the-art and future scenarios," *Journal of Energy and Power Engineering*, **8**(1), pp. 7–15.

[41] Wang, Z. and S. Wang (2013) "Grid power peak shaving and valley filling using Vehicle-to-Grid systems," *IEEE Transactions on Power Delivery*, **28**(3), pp. 1822–1829.

[42] Dallinger, D., D. Krampe, and M. Wietschel (2011) "Vehicle-to-Grid regulation reserves based on dynamic simulation of mobility behavior," *IEEE Transactions on Smart Grid*, **2**(2), pp. 302–313.

[43] Pillai, J. R. and B. Bak-Jensen (2011) "Integration of Vehicle-to-Grid in the Western Danish power system," *IEEE Transactions on Sustainable Energy*, **2**(1), pp. 12–19.

[44] Lund, H. and W. Kempton (2008) "Integration of renewable energy into the transport and electricity sectors through V2G," *Energy Policy*, **36**(9), pp. 3578–3587.

[45] Hartmann, N. and E. zdemir (2011) "Impact of different utilization scenarios of electric vehicles on the German grid in 2030," *Journal of Power Sources*, **196**(4), pp. 2311 – 2318.

[46] Lassila, J., J. Haakana, V. Tikka, and J. Partanen (2012) "Methodology to analyze the economic effects of electric cars as energy storages," *IEEE Transaction on Smart Grid*, **3**(1), pp. 506–516.

[47] Sortomme, E. and M. El-Sharkawi (2012) "Optimal scheduling of vehicle-to-grid energy and ancillary services," *IEEE Transaction on Smart Grid*, **3**(1), pp. 351–359.

[48] Stadler, M., C. Marnay, R. Sharma, G. Mendes, et al. (2011) "Modeling electric vehicle benefits connected to smart grids," in *2011 IEEE Power and Propulsion Conference (VPPC)*, pp. 1–8.

[49] Su, W. and J. Wang (2012) "Energy Management Systems in Microgrid Operations," *The Electricity Journal*, **25**(8), pp. 45 – 60.

[50] Sundstrom, O., D. Ambuhl, and L. Guzzella (2009) "On Implementation of Dynamic Programming for Optimal Control Problems With Final State Constraints," *Oil Gas Science and Technology*, **65**(1), pp. 91–102.

[51] Riffonneau, Y., S. Bacha, F. Barruel, and S. Ploix (2011) "Optimal power flow management for grid connected pv systems with batteries," *IEEE Transactions on Sustainable Energy*, **2**(3), p. 309320.

[52] Grillo, S., M. Marinelli, S. Massucco, and F. Silvestro (2012) "Optimal Management Strategy of a Battery-Based Storage System to Improve Renewable Energy Integration in Distribution Networks," *IEEE Transactions Smart Grid*, **3**(2), pp. 950–958.

[53] Geering, H. P. (2007) *Optimal Control with Engineering Applications*, Springer.

[54] Serrao, L. and G. Rizzoni (2008) "Optimal control of power split for a hybrid electric refuse vehicle," in *2008 American Control Conference*, pp. 4498–4503.

[55] Rahbar, K., J. Xu, and R. Zhang (2015) "Real-Time Energy Storage Management for Renewable Integration in Microgrid: An Off-Line Optimization Approach," *IEEE Transactions on Smart Grid*, **6**(1), pp. 124–134.

[56] Ahn, S., S. Nam, J. Choi, and S. Moon (2013) "Power scheduling of distributed generators for economic and stable operation of a microgrid," *IEEE Transactions on Smart Grid*, **4**(1), pp. 398–405.

[57] de Ven, P. V., N. Hedge, L. Massoulie, and T. Salonidis (2013) "Optimal control of end-user energy storage," *IEEE Transactions on Smart Grid*, **4**(2), pp. 789–797.

[58] Dagdougui, H., A. Ouammi, and R. Sacile (2014) "Optimal Control of a Network of Power Microgrids Using the Pontryagin's Minimum Principle," *IEEE Transactions on Control Systems Technology*, **22**(5), pp. 1942 – 1948.

[59] Qiang, F., A. Hamidi, A. Nasiri, V. Bhavaraju, et al. (2013) "The Role of Energy Storage in a Microgrid Concept: Examining the opportunities and promise of microgrids." *IEEE Electrification Magazine*, **5**(2), pp. 21–29.

[60] Pudjianto, D., C. Ramsay, and G. Strbac (2007) "Virtual power plant and system integration of distributed energy resources," *IET Renewable Power Generation*, **1**(1), pp. 10–16.

[61] Giuntoli, M. and D. Poli (2013) "Optimized Thermal and Electrical Scheduling of a Large Scale Virtual Power Plant in the Presence of Energy Storages," *IEEE Transactions on Smart Grid*, **4**(2), pp. 942–955.

[62] Xin, D., H.and Gan, N. Li, et al. (2013) "Virtual power plant-based distributed control strategy for multiple distributed generators," *IET Control Theory and Applications*, **7**(1), pp. 90–98.

[63] Khan, H., S. Dasouki, V. Sreeram, et al. (2013) "Universal active and reactive power control of electronically interfaced distributed generation sources in virtual power plants operating in grid-connected and islanding modes," *IET Generation, Transmission and Distribution*, **7**(8), pp. 885–897.

[64] Nikonowicz, L. and M. J. (2012) "Virtual power plants general review: structure, application and optimization," *Journal of Power Technologies*, **92**(3), pp. 135–149.

[65] Petterson, S. B., J. Apt, and J. F. Whitacre (2010) "Lithium-ion battery cell degradation resulting from realistic vehicle and vehicle-to-grid utilization," *Journal of Power Sources*, **195**(8), pp. 2385–2392.

[66] DIW Berlin & DLR-Institut fur Verkehrsforrschung (2008), "MiD-2008. Mobilitat in Deutschland," `http://www.clearingstelle-verkehr.de`.

[67] International Energy Agency and Nuclear Energy Agency (2005) *Projected Costs of Generating Electricity*, *Tech. rep.*

[68] Bhattacharyya, S. C. (2011) *Energy Economics: Concepts, Issues, Markets and Governance*, Springer.

[69] European Commission (2003) *External Costs. Research results on socio-environmental damages due to electricity and transport*, *Tech. rep.*

[70] Ratha, A., E. Iggland, and G. Andersson (2013) "Value of Lost Load: How much is supply security worth?" in *IEEE Power and Energy Society General Meeting (PES)*, pp. 1–5.

[71] Heylen, E., G. Deconinck, and D. V. Hertem (2015) "Impact of value of lost load on performance of reliability criteria and reliability management," in *IEEE PowerTech Conference*, pp. 1–6.

[72] Lombardi, P., P. Vasquez, and Z. Styczynski (2009) "Plug-in electric vehicles as storage devices within an Autonomous power system. Optimization issue," in *IEEE PowerTech Conference*, pp. 1–7.

[73] Musio, M. and A. Damiano (2012) "A virtual power plant management model based on electric vehicle charging infrastructure distribution," in *IEEE PES International Conference and Exhibition on Innovative Smart Grid Technologies*, pp. 1–7.

[74] European Commission, "Energy, Transport and environment indicators," `http://ec.europa.eu/eurostat`, year = 2010.

[75] Pousinho, H. M. I., H. Silva, V. Mendes, et al. (2014) "Self-scheduling for energy and spinning reserve of wind/CSP plants by a MILP approach," *Energy*, **78**, pp. 524–534.

[76] Forrester, J. (2014) "The Value of CSP with Thermal Energy Storage in Providing Grid Stability," *Energy Procedia*, **49**, pp. 1632–1641.

[77] Pfenninger, S., P. Gauch, J. Lilliestam, et al. (2014) "Potential for concentrating solar power to provide baseload and dispatchable power," *Nature Climate Change*, **4**, pp. 689–692.

[78] Sardegna Ricerche - Renewable Energy Cluster (2015), "Concentrating Solar Power Project," `http://www.sardegnaricerche.it/en/`.

[79] Cau, G. and D. Cocco (2014) "Comparison of medium-size concentrating solar power plants based on parabolic trough and linear Fresnel collectors," *Energy Procedia*, **45**, pp. 101–110.

[80] Teleke, S., M. E. Baran, S. Bhattacharya, and A. Q. Huang (2010) "Rule-Based Control of Battery Energy Storage for Dispatching Intermittent Renewable Sources," *IEEE Transactions on Sustainable Energy*, **1**(3), pp. 117–124.

[81] Sorrentino, M., G. Rizzo, and I. Arsie (2011) "Analysis of a rule-based control strategy for on-board energy management of series hybrid vehicles," *Control Engineering Practice*, **19**(12), p. 14331441.

[82] Waschl, H., I. Kolmanovsky, M. Steinbuch, and L. del Re (2014) *Optimization and Optimal Control in Automotive Systems*, Springer International Publishing.

[83] Betts, J. (2010) *Practical Methods for Optimal Control and Estimation Using Nonlinear Programming*, Society for Industrial and Applied Mathematics.

[84] Chachuat, B., B. Srinivasan, and D. Bonvin (2009) "Adaptation strategies for real-time optimization," *Computers & Chemical Engineering*, **33**(10), pp. 1557 – 1567.

[85] Biegler, L. (2009) "Technology Advances for Dynamic Real-Time Optimization," in *10th International Symposium on Process Systems Engineering: Part A* (C. A. O. d. N. Rita Maria de Brito Alves and E. C. Biscaia, eds.), vol. 27, Elsevier, pp. 1 – 6.

[86] Bonvin, D. and B. Srinivasan (2013) "On the role of the necessary conditions of optimality in structuring dynamic real-time optimization schemes," *Computers & Chemical Engineering*, **51**, pp. 172 – 180.

[87] Lifshitz, D. and G. Weiss (2015) "Optimal energy management for grid-connected storage systems," *Optimal Control Applications and Methods*, **36**(4), pp. 447–462.

[88] Kriett, P. O. and M. Salani (2012) "Optimal control of a residential microgrid," *Energy*, **42**(1), pp. 321 – 330.

[89] Kim, N., S. Cha, and H. Peng (2011) "Optimal Control of Hybrid Electric Vehicles Based on Pontryagin's Minimum Principle," *IEEE Transactions on Control Systems Technology*, **19**(5), pp. 1279–1287.

[90] Ngo, V., T. Hofman, M. Steinbuch, and A. Serrarens (2012) "Optimal Control of the Gearshift Command for Hybrid Electric Vehicles," *IEEE Transactions on Vehicular Technology*, **61**(8), pp. 3531–3543.

[91] Raab, A. F., M. Ellingsen, and A. Walsh *Mobile Energy Resources in Grids of Electricity (MERGE). Grant Agreement: 241399 WP 1 Task 1.6 Deliverable D1.4 Learning from EV field tests*, *Tech. rep.*

[92] Autonomous Region of Sardinia (2016), "Sardinian Regional Energy Plan 2015-2030," `http://www.regione.sardegna.it`.

[93] Lunz, B., Z. Yan, J. B. Gerschler, and D. U. Sauer (2012) "Influence of plug-in hybrid electric vehicle charging strategies on charging and battery degradation costs," *Energy Policy*, **46**, pp. 511–519.

[94] Lacey, G., T. J., P. G., and R. Kotter (2013) "The effect of cycling on the state of health of the electric vehicle battery," in *48th International Universities'Power Engineering Conference (UPEC)*, pp. 1–7.

[95] Malysz, P., S. Sirouspour, and A. Emadi (2014) "An optimal energy storage control strategy for grid-connected microgrids," *IEEE Transactions on Smart Grid*, **5**(4), pp. 1785–1796.

[96] Zhu, D., Y. Wang, N. Chang, and M. Pedrant (2014) "Optimal design and management of a smart residential PV and energy storage system," in *IEEE Design, Automation and Test in Europe Conference and Exhibition*, pp. 1–6.

[97] Garcia-Torres, F. and C. Bordons (2015) "Optimal economical schedule of hydrogen-based microgrids with hybrid storage using model predictive control," *IEEE Transactions on Industrial Electronics*, **62**(8), pp. 100–111.

[98] Li, G., X. Lu, J. Kim, et al. (2013) "Cell degradation of a $NaNiCl_2$ (ZEBRA) battery," *Journal of Materials Chemistry A*, **1**(47), pp. 14935–14942.

[99] Gestore dei Mercati Energetici (GME) (2015), `http://www.mercatoelettrico.org/en/Default.aspx`.

[100] Autorità per l'Energia Elettrica e il Gas e il Sistema Idrico (AEEGSI), "del. 578/2013/R/eel, Dec. 2013." .

[101] V. Marano, a. S. O., Y. Guezennec, et al. (2009) "Lithium-ion batteries life estimation for plug-in hybrid electric vehicles," in *IEEE Vehicle Power and Propulsion Conference*, p. 536543.

[102] Zhang, H. and M.-Y. Chow (2010) "Comprehensive dynamic battery modeling for PHEV applications," in *IEEE PES General Meeting*, pp. 1–6.

[103] Tsang, K., L. Sun, and W. Chan (2010) "Identification and modelling of Lithium ion battery," *Energy Conversion and Management*, **51**(12), pp. 2857–2862.

[104] Chen, M. and G. Rincon-Mora (2006) "Accurate Electrical Battery Model Capable of Predicting Runtime and IV Performance," *IEEE Transactions on Energy Conversion*, **21**(2), pp. 504–511.

[105] Kim, T. and W. Qiao (2011) "A Hybrid Battery Model Capable of Capturing Dynamic Circuit Characteristics and Nonlinear Capacity Effects," *IEEE Transactions on Energy Conversion*, **26**(4), pp. 1172–1180.

[106] Jongerden, M. and B. Haverkort (2009) "Which battery model to use?" *IET Software*, **3**(6).

[107] Rahimi-Eichi, H., U. Ojha, F. Baronti, and M. Chow (2013) "Battery Management System: An Overview of Its Application in the Smart Grid and Electric Vehicles," *IEEE Industrial Electronics Magazine*, **7**(2), pp. 4–16.

[108] Yilmaz, M. and P. T. Krein (2013) "Review of Battery Charger Topologies, Charging Power Levels, and Infrastructure for Plug-In Electric and Hybrid Vehicles," *IEEE Transactions on Power Electronics*, **28**(5).

[109] Dougal, R. (2002) "Dynamic lithium-ion battery model for system simulation," *IEEE Transactions on Components and Packaging Technologies*, **25**(3), pp. 495–505.

[110] Benato, R., N. Cosciani, G. Crugnola, et al. (2015) "Sodium nickel chloride battery technology for large-scale stationary storage in the high voltage network," *Journal of Power Sources*, **293**, pp. 127–136.

[111] Sudworth, J. L. (2001) "The sodium/nickel chloride ZEBRA battery," *Journal of Power Sources*, **100**, pp. 149–163.

[112] Dustmann, C.-H. (2004) "Advances in ZEBRA batteries," *Journal of Power Sources*, **127**, pp. 85–92.

[113] Restello, S., G. Lodi, and A. Miraldi (2012) "Sodium Nickel Chloride Batteries for telecom application: A solution to critical high energy density deployment in telecom facilities," in *IEEE 34th International Telecommunications Energy Conference*, pp. 1–6.

[114] Manzoni, R. (2015) "Sodium Nickel Chloride batteries in transportation applications," in *IEEE International Conference on Electrical Systems for Aircraft, Railway, Ship Propulsion and Road Vehicles (ESARS 2015)*, pp. 1–6.

[115] Hentunen, A., T. Lehmuspelto, and J. Suomela (2014) "Time-domain parameter extraction method for Thevenin-equivalent circuit battery models," *IEEE Transactions on Energy Conversion*, **29**(3), pp. 558–566.

[116] Hsieh, Y.-C., T.-D. Lin, R.-J. Chen, and H.-Y. Lin (2014) "Electric circuit modelling for lithium-ion batteries by intermittent discharging," *IET Power Electronics*, **7**(10), pp. 2672–2677.

[117] Rahimi-Eichi, H., F. Baronti, and M.-Y. Chow (2014) "Online Adaptive Parameter Identification and State-of-Charge Coestimation for Lithium-Polymer Battery Cells," *IEEE Transactions on Industrial Electronics*, **61**(4), pp. 2053–2061.

[118] Barali, S. and M. Ceraolo (2002) "Dynamical models of lead-acid batteries: implementation issues," *IEEE Transactions on Energy Conversion*, **17**(1), pp. 16–23.

[119] Carter, A., R.and Cruden, P. Hall, and A. Zaher (2011) "An Improved lead-acid Battery Pack Model for Use in Power Simulations of Electric Vehicles," *IEEE Transactions on Energy Conversion*, **27**(1), pp. 21–28.

[120] Tian, S., M. Hong, and M. Ouyan (2009) “An Experimental Study and Nonlinear Modeling of Discharge IV Behavior of Valve-Regulated lead-acid Batteries,” *IEEE Transactions on Energy Conversion*, **24**(2), pp. 452–458.

[121] O Sullivan, T., C. Bingham, and R. Clark (2006) “Zebra battery technologies for all electric smart car,” in *IEEE International Symposium on Power Electronics, Electrical Drives, Automation and Motion*, pp. 243–248.

[122] Gerovasili, E., J. F. May, and D. U. Sauer (2014) “Experimental evaluation of the performance of the sodium metal chloride battery below usual operating temperatures,” *Journal of Power Sources*, **251**, pp. 137–144.

Publications

1. Marco Camerada, Giorgio Cau, Daniele Cocco, Alfonso Damiano, Valeria Demontis, Tiziana Melis and **Maura Musio**, “A Pilot Power Plant Based on Concentrating Solar and Energy Storage Technologies for Improving Electricity Dispatch”, *Energy Procedia*, vol. 81, pp. 165-172, Dec. 2015.

2. **Maura Musio** and Alfonso Damiano, “A Non-Linear Dynamic Electrical Model of Sodium-Nickel Chloride Batteries”, *4th International Conference on Renewable Energy Research and Applications (ICRERA)*, Nov. 2015, pp. 1-8.

3. Marco Camerada, Giorgio Cau, Daniele Cocco, Alfonso Damiano, Valeria Demontis, Tiziana Melis and **Maura Musio**, “Villacidro Solar Demo Plant: integration of small-scale CSP and biogas power plants in an industrial microgrid”, *21st International Conference on Solar Power And Chemical Energy Systems (SolarPaces)*, Oct. 2015, pp. 1-8.

4. Valeria Demontis, Marco Camerada, Giorgio Cau, Daniele Cocco, Alfonso Damiano, Tiziana Melis and **Maura Musio**, “Progress In Preliminary Studies at Ottana Solar Facility”, *21st International Conference on Solar Power And Chemical Energy Systems (SolarPaces)*, Oct. 2015, pp. 1-8.

5. **Maura Musio**, Alessandro Serpi, Claudia Musio and Alfonso Damiano, “Optimal Management Strategy of Energy Storage Systems for RES-based Microgrids”, *41st Annual Conference of the IEEE Industrial Electronics Society (IECON)*, Nov. 2015, pp. 5044-5049.

6. **Maura Musio**, Mario Porru, Alessandro Serpi, Ignazio Marongiu and Alfonso Damiano, “Optimal electric vehicle charging strategy for energy management in microgrids”, *IEEE International Electric Vehicle Conference (IEVC)*, Dec. 2014, pp. 1-8.

7. **Maura Musio** and Alfonso Damiano, "Analysis of Vehicle to Grid and energy storage integration in a virtual power plant", *40th Annual Conference of the IEEE Industrial Electronics Society (IECON)*, Oct. 2014, pp. 3094-3100.
8. Donato Vincenzi, Stefano Baricordi, Silvia Calabrese, **Maura Musio** and Alfonso Damiano, "A Cassegrain Concentrator Photovoltaic System: comparison between dichroic and multijunction photovoltaic configurations", *40th Annual Conference of the IEEE Industrial Electronics Society (IECON)*, Oct. 2014, pp. 1900-1905.
9. Malgorzata Gawronska, Carla Sanna, **Maura Musio** and Alfonso Damiano, "Preliminary evaluation of HCPV system infield energy production in the Mediterranean area", *29th European Photovoltaic Solar Energy Conference (EU PVSEC)*, Sept. 2014, pp. 2128-2133.
10. **Maura Musio** and Alfonso Damiano, "A simplified charging battery model for smart electric vehicles applications", *IEEE International Energy Conference (ENERGYCON)*, May 2014, pp. 1429-1436.
11. **Maura Musio**, Claudia Musio, Carla Sanna, Malgorzata Gawronska and Alfonso Damiano, "Characterization of a CPV module prototype for design and performance improvement", *IEEE International Energy Conference (ENERGYCON)*, May 2014, pp. 983-990.
12. Alfonso Damiano, Ignazio Marongiu, Claudia Musio and **Maura Musio**, "Concentrator photovoltaic standards: experimental analyses of technical requirements", *39th Annual Conference of the IEEE Industrial Electronics Society (IECON)*, Nov. 2013, pp. 8074-8079.
13. Alfonso Damiano, Ignazio Marongiu, Claudia Musio and **Maura Musio**, "Outdoor characterization of a Cassegrain-type concentrator photovoltaic receiver", *39th Annual Conference of the IEEE Industrial Electronics Society (IECON)*, Nov. 2013, pp. 8110 - 8115.
14. Malgorzata Gawronska, Carla Sanna, Tonino Pisanu, Claudia Musio, **Maura Musio** and Alfonso Damiano, "Cost effective HCPV Fresnel lenses module prototype: design, performance, results, in-field testing and economic analysis", *28th European Photovoltaic Solar Energy Conference (EU PVSEC)*, Sept. 2013, pp. 606-611.

List of Figures

List of Tables